An Experimental Investigation of Structure, Mixing and Combustion in Compressible Turbulent Shear Layers

Thesis by

Jeffery Lawrence Hall

In Partial Fulfillment of the Requirements

for the Degree of

Doctor of Philosophy

California Institute of Technology

Pasadena, California

1991

(submitted November 2, 1990)

Acknowledgements

A great many people have contributed to this project over the years, and I would like to take this opportunity to acknowledge their efforts and thank them for making this thesis a reality. Below, I have listed everybody (I hope!) along with a brief description of their contribution:

- Paul Dimotakis, Professor of Aeronautics and Applied Physics. In addition to all the things an advisor usually does, I particularly appreciate the fact that Paul gave me remarkably free rein to work things out for myself, even when the road got very, very bumpy.
- Earl Dahl, GALCIT technical staff. We served "in the trenches" together and literally built the lab from the ground up. More than anyone else, Earl deserves credit for making the new facility work.
- Cliff Frieler, Graduate Research Assistant. Much of the early conceptual design came from Cliff. He was (and is) the best "sounding board" I know and answered more of my questions than any other two people combined during the course of this project.
- Henning Rosemann, Research Fellow in Aeronautics. Henning played a key role in helping me to debug the new facility and make it operational. He is the second best "sounding board" I know and contributed significantly to the interpretation of the experimental results as they came in.
- Dimitri Papamoschou, Research Fellow in Aeronautics. Dimitri's experience with his own supersonic facility was a valuable resource for me in designing the new lab. Less tangibly, he instilled some much-needed confidence in me during the early days of this project.
- Dan Lang, Staff Engineer. Our resident electronics and computer wizard worked his usual magic on my lab and made sure that everything functioned properly.
- Norm Keidel, Manager of Caltech's Central Engineering Services. Most of the big, critical components were fabricated in Norm's shop, including the test section and the main pressure regulator. Also, the value of the

design help and good humour that Norm and his co-workers contributed to this project cannot be underestimated. These co-workers include: Lou Johnson, George Yamamoto, Ralph Ortega, Rick Paniagua, Mike Gerfen, Steve Siguenza, Betty Swartout and Bovan Bang.

- Alan Goudey, GALCIT technical staff. Some of the design and most of the construction and installation of the lab's electrical/electronics systems were performed by Alan.
- George Lundgren, manager of the GALCIT Machine Shop. Though on a lesser scale than Central Engineering Services, George and his co-workers also provided valuable hardware, design ideas and good humour. George's co-workers were Phil Wood, George Wilson and Larry Frazier.
- Harry Hamaguchi, GALCIT technical staff. Harry was my photography expert, teaching me a lot about the subject while he processed more film than either of us probably cares to remember.
- Rick Gilbrech, Graduate Research Assistant. Although our facilities were different, we shared the same advisor, the same building, some of the same equipment and many of the same problems. His efforts on our mutual behalf are very much appreciated.
- Chris Bond, Graduate Research Assistant. Chris joined the team quite late because he represents the next generation of students in the new facility. Even so, he managed to help out quite a bit in the final experimental stage of my thesis.
- Tom Sobota, Research Fellow in Aeronautics. Tom contributed to the design of the main pressure regulator and provided the lead for finding the four-inch high pressure shutoff valve.
- Jose Lopez-Tiana, Tim Harris and Ralph Kemmerer, Caltech Purchasing Department. These three individuals were instrumental in keeping the flow of equipment and material coming to the lab during the long construction period.
- Ron Wayland and Alan Taylor, Caltech Physical Plant. This duo was primarily responsible for ensuring that I always had enough gas to conduct experiments, despite often short notice and severe problems with the off-campus supplier.
- Herb Gaebler, Clarence Hemphill and Pavel Svitek, GALCIT technical staff. I did not call upon them very much, but when I did, they were always ready to help, be it with ideas or just another pair of hands.

This work would not have been possible without the generous long-term sponsorship of the Air Force Office of Scientific Research. Particular thanks go to our contract monitor, Dr. Julian Tishkoff, for his patience and help during this project.

Finally, I would like to thank my family for their love and support over the years while I laboured far from home.

Abstract

Two-dimensional, compressible, turbulent shear layers are studied in a new wind tunnel facility. Both reacting and non-reacting flows are investigated, with one free stream velocity supersonic and the other subsonic. The combustion experiments are based on the use of low concentrations of hydrogen, nitric oxide and fluorine gases. Side-view Schlieren photographs of these reacting and non-reacting flows appear devoid of the two-dimensional, large-scale structures seen in incompressible flows. Comparison with all-subsonic flows produced in the same facility suggests that this lack of two-dimensional structure is due to the presence of the supersonic high-speed free stream velocity. Travelling shock and expansion waves are observed in the high compressibility flows, evidently created by turbulent structures convecting at supersonic velocities. Such waves are seen only in the low-speed fluid, with apparent convection velocities much higher than those predicted on the basis of isentropic pressure-matching arguments. The measured shear layer growth rates agree with previous results by other experimenters, except for a few cases at low compressibility and low density ratio. The fast chemistry regime is attained in some of the high compressibility flows tested. "Flip" experiments conducted in this regime indicate that the volume fraction of mixed fluid in the layer is substantially reduced as compared to previous incompressible results. These same flip experiments also reveal that compressibility significantly alters the entrainment ratio. Finally, it is observed that the shear layer growth rate is relatively insensitive to incident shock/expansion waves and significant heat release inside the shear layer.

Table of Contents

CHAPTER 1

Introduction

For a number of years now, there has existed at GALCIT* a continuing research effort into turbulence, with particular emphasis on the entrainment and mixing processes of turbulent shear flows. The current work can be viewed as a logical extension of such investigations into the realm of compressible flow. The recent surge of interest in hypersonic flow and SCRAMJET ** engine technology has provided further motivation for this research effort. The two-dimensional mixing layer geometry was chosen for this study for the same reasons it had been chosen in so many previous investigations: It is a simple turbulent shear flow and hence is potentially amenable to analysis; and there already exists a very large body of data on such flows (though mostly at incompressible flow conditions) with which to make comparisons.

One of the key issues in compressible shear layer research is the possible existence of large-scale coherent structures. The significance of such structures in incompressible mixing layers was made clear by the work of Brown & Roshko (1971, 1974). Subsequent studies have demonstrated that these structures play a central role in the entrainment and mixing processes of such flows (Konrad 1976, Dimotakis & Brown 1976, Wallace 1981, Breidenthal 1981, Broadwell & Breidenthal 1982, Mungal & Dimotakis 1984, Bernal & Roshko 1986, Koochesfahani & Dimotakis 1986, Frieler & Dimotakis 1988, Hermanson & Dimotakis 1989). This mixing layer research was extended into the compressible domain by Papamoschou & Roshko (1988). However, their Schlieren photographic data did *not* clearly show the two-dimensional vortices seen in incompressible flows. A similar lack of structure was found by Chinzei *et al.* (1986), Clemens *et al.* (1990) and Goebel & Dutton (1990). However, recent pictures by Clemens & Mungal (1990) do show such vortices, but only at low compressibility levels. Papamoschou (1989) demonstrated that there are "frozen" features in the shear layer that convect at a distinct velocity. Large-scale structure was also detected in the supersonic slot-injection experiments of Clark

---

* Graduate Aeronautical Laboratories, California Institute of Technology

** Supersonic Combustion Ramjet

et al. (1990). Further evidence for large-scale structures can be found in the axisymmetric jet experiments of Fourguette & Dibble (1990). Their two-dimensional Rayleigh scattering images clearly show distinct regions of fluid (as denoted by the intensity of scattered light) separated by regular intervals. Interestingly enough, this structure was detected at a compressibility level beyond that at which Clemens & Mungal (1990) were able to find such structures. The difference between a "slice" view (planar Rayleigh scattering) and a spanwise integrated view (Schlieren) is a possible explanation for this difference, one that points to a significant role played by three-dimensional effects in compressible turbulent shear layers.

A second fundamental question regarding compressible shear layers is whether or not travelling shock and expansion waves are created by turbulent structures convecting at supersonic velocities with respect to one or both free streams. Such travelling waves have been detected in supersonic jet experiments (Lowson & Ollerhead 1968, Tam 1971, Ortwerth & Shine 1977 and Oertel 1979) with the waves originating from the shear layer forming near the jet exit. However, none of the existing photographic data for two-dimensional compressible shear layers shows these waves. It is not clear if these waves did not exist in the flows tested, or if their signal was too weak to be detected. Both Papamoschou (1989) and Dimotakis (1989) have argued for the existence of strong travelling shock waves as a way of resolving the otherwise baffling results for the measured convection velocities of shear layer structures. Some support for this can be found in the numerical simulations of Lele (1989) which do show travelling shock waves in a mixing layer flow. Clearly, there exists a need to reconcile such results and speculations with the lack of experimental evidence for travelling waves.

The effect of compressibility on the growth rate, molecular mixing and chemical reactions forms a third line of inquiry for the present research program. The large decrease in growth rate at high levels of compressibility has been well documented (Papamoschou & Roshko 1988). This experimental observation is also supported by the linear stability analyses of unbounded shear layers by Lessen *et al.* (1965), Ragab & Wu (1987) and Zhuang *et al.* (1988), which indicate that compressible shear layers are less unstable than their incompressible counterparts. In fact, these analyses suggest that the instability modes become almost neutrally stable as compressibility increases. Recent work by Tam & Hu (1989) and Zhuang *et al.* (1990) for bounded shear layers demonstrates that the boundaries can, however, reflect radiated energy back into the shear layer, creating new unstable modes. As regards molecular mixing, much less is known. Recent experimental measurements by Dutton *et al.* (1990) using Mie scattering have provided an estimate of the probability

of mixed fluid across the layer. Such measurements, however, suffer from the same resolution problems that were encountered by Konrad (1976) in his incompressible experiments. A way to avoid these resolution problems is to use chemical reactions in the limit of fast kinetics as a diagnostic for molecular mixing, as was done in the experiments of Breidenthal (1981), Wallace (1981), Mungal & Dimotakis (1984), Koochesfahani & Dimotakis (1986) and many others. Specifically, each free stream carries a different chemical reactant, so that the detection of a chemical *product* is an indicator of molecular mixing and subsequent chemical reaction. Such combustion experiments also have value from the viewpoint of practical devices; indeed, the feasibility of SCRAMJET engine technology is directly related to the issues of molecular mixing and chemical kinetics in compressible shear flows.

It was decided to address these issues in the present research effort by constructing a new experimental facility specifically designed for two-dimensional, supersonic, chemically reacting shear layers. What emerged from the design process was a two-stream blowdown wind tunnel with the capability to study hydrogen-fluorine-nitric oxide combustion at compressible flow conditions. Enough flexibility was incorporated to allow for investigations across part of the large parameter space of compressible reacting and non-reacting shear layer phenomena. The present study represents only a preliminary excursion into this parameter space, focusing primarily on the three aforementioned issues at the low end of the compressibility scale. Nevertheless, it was hoped that some progress could be made on the outstanding issues, and in any case, this research would provide direction for future experiments in the facility.

The theoretical framework that formed the basis for the facility design and experiment interpretation will be discussed in Chapter 2. A reasonably detailed description of the new facility constitutes Chapter 3. Chapter 4 presents and discusses the results for the non-reacting experiments, while Chapter 5 does the same for the combustion experiments.

CHAPTER 2
Theoretical Considerations

2.1 Overview

This chapter will provide a brief review of some of the key results and theoretical ideas that provide the foundation for turbulent shear layer research. It will focus on the specific issues to be addressed in the current study: structure, growth rate, mixing and chemical reactions. In addition, some attempt will be made to show how these issues served as design drivers for the new facility. For a more comprehensive review of turbulent shear layers, the reader is referred to a recent discussion by Dimotakis (1989).

The basic geometry of this flow is depicted in Fig. 2.1. The turbulent shear layer forms between two (almost) parallel free streams that have different velocities. Experimentally, it is found that the thickness of the layer, δ, grows linearly with downstream distance x. Note that if large vortical structures are present, the shear layer growth rate is linear only on a time-averaged basis. Also note that there are various definitions of δ based on the velocity, vorticity and concentration profiles. This study will primarily use a concentration profile measure, specifically the visual thickness obtained from Schlieren photographs. Stream 1 is defined to be the high-speed stream with velocity u_1, density ρ_1, pressure p_1, temperature T_1 and specific heat ratio γ_1. The same variables are used on the low-speed side with a subscript 2. The upper (high-speed) guidewall that bounds the flow is specified to be parallel to the x-axis. The lower guidewall is allowed to deflect to an angle β with respect to the upper guidewall in order to control the streamwise pressure gradient dp/dx. The angles α_1 and α_2 describe the orientation of the shear layer edges within the channel.

2.2 Growth Rate

Models for the growth rate of incompressible non-reacting shear layers have typically assumed that the growth rate depends on two dimensionless parameters, *i.e.*,

$$\frac{\delta}{x} = \frac{\delta}{x}(r, s) \tag{2.2.1}$$

where r and s are the free stream velocity and density ratios; *i.e.*,

$$r \equiv \frac{u_2}{u_1} \qquad \text{and} \qquad s \equiv \frac{\rho_2}{\rho_1} \, . \tag{2.2.2}$$

For example, based on an analysis of a temporally growing shear layer, Brown (1974) proposed

$$\frac{\delta}{x} = C_\delta \frac{(1-r)(1+s^{1/2})}{(1+rs^{1/2})} \, , \tag{2.2.3}$$

while Dimotakis (1984) suggested a slightly modified version that incorporated the effects of spatial growth; *i.e.*,

$$\frac{\delta}{x} = C_\delta \frac{(1-r)(1+s^{1/2})}{(1+rs^{1/2})} \left\{ 1 - \frac{(1-s^{1/2})/(1+s^{1/2})}{1+2.9(1+r)/(1-r)} \right\} . \tag{2.2.4}$$

Unfortunately, the proportionality constant C_δ is found to vary almost by a factor of two over the many experiments that have been conducted. (See Fig. 10 of Brown & Roshko 1974.) This strongly suggests that r and s form an incomplete set of independent variables for modelling the growth rate.

Striking evidence for this "incompleteness" is presented in Fig. 2 of Dimotakis (1989). Although r and s were held fixed for the four experiments, the growth rate was approximately halved by simply increasing the velocity of both free streams by a factor of roughly six. Since this appears to indicate a dependence on velocity difference Δu, one might infer a Reynolds number effect where

$$Re_\delta \equiv \frac{\Delta u \delta}{\nu} \tag{2.2.5}$$

is the local Reynolds number and

$$\Delta u \equiv u_1 - u_2 \tag{2.2.6}$$

is the velocity difference across the layer, and

$$\nu \equiv \frac{\mu}{\rho} \tag{2.2.7}$$

is the kinematic viscosity. However, this would be incorrect because the growth rate is clearly *insensitive* to Re_δ as can be seen from the photographs. As Re_δ increases considerably from the splitter tip to downstream location (*i.e.*, as δ increases), the shear layer growth rate *does not change* (Dimotakis 1989).

At the time of this writing, the correct non-dimensional variable that scales this effect is not known. Indeed, the physical mechanism involved is not known either. Speculation is focused on the initial conditions of the flow, particularly the state of the boundary layers coming off the splitter tip. Browand & Latigo (1979) demonstrated that turbulent boundary layers result in lower growth rates than laminar boundary layers. However, other factors could contribute; for example, the momentum thicknesses of the two streams, the thickness of the trailing edge of the splitter plate, the free stream turbulence levels, *etc.* Given the poor state of knowledge of this phenomenon, one must conclude that Eqs. 2.2.3 and 2.2.4 may not be reliable estimators of turbulent shear layer growth rates, especially if one hopes to collapse data from different experiments in different facilities.

This problem is also vexing with regard to assessing the effects of compressibility on the growth rate. Specifically, how does one decide whether the growth rate reduction is due to compressibility effects or to something else like a change in initial conditions or an increase in free stream velocity, as in Dimotakis (1989)? Since increasing Mach numbers are usually accompanied by increasing velocities and changes in the splitter-plate boundary layers, this question assumes critical importance. Unfortunately, this question cannot be answered at the present time, and in fact, most researchers have tended to assume that *all* of the experimentally measured growth rate reduction was due to compressibility effects at high Mach numbers. It should be emphasized, however, that this approach is not completely without merit; witness the reasonably good collapse of the available data in Fig. 2.2.[†] In that plot, the measured growth rates from the total pressure profiles have been normalized by the incompressible model equation (Eq. 2.2.3) and plotted as a function of the convective Mach number M_{c1}, where M_{c1} is defined by

$$M_{c1} \equiv \frac{u_1 - u_c}{a_1} \,, \tag{2.2.8}$$

with u_c the convection velocity of the large scale structures of the shear layer and a_1 the speed of sound of stream 1. As an aside, it should be noted that one can also define a second convective Mach number; *i.e.*,

$$M_{c2} \equiv \frac{u_c - u_2}{a_2} \,. \tag{2.2.9}$$

[†] The Chinzei *et al.* (1986) data were converted to this normalized form by Dimotakis (1989).

There is *some* indication from Figure 2.2 that the normalization of the compressible growth rate by Eq. 2.2.3 may be faulty. Specifically, the Chinzei *et al.* (1986) and Clemens & Mungal (1990) data do *not* recover the incompressible growth rate at $M_{c1} \simeq 0.25$ as the Papamoschou & Roshko (1988) data do. Nevertheless, the rest of the data agree well and the trend towards lower growth rate at high compressibility is unmistakable in all three studies.

Bogdanoff (1983) was the first to argue that the compressibility effect on the growth rate could be reasonably well scaled by the convective Mach number. The collapse of the data in Fig. 2.2 supports this view; however, it is interesting to note that neither of the free stream Mach numbers, *i.e.*,

$$M_1 \equiv \frac{u_1}{a_1} \qquad \text{and} \qquad M_2 \equiv \frac{u_2}{a_2} \,, \tag{2.2.10}$$

enters directly into this scaling argument. The deduction to be made from this is that compressibility effects can be present, even if one of the free stream Mach numbers is incompressible ($M_{1,2} \ll 1$), by simply ensuring that the velocity *difference* is sufficiently high. This conclusion is exploited in the design of the new facility. Here, the low-speed stream is limited to low subsonic flow ($M_2 < 0.5$), allowing for the generation of high velocity differences and therefore high convective Mach numbers. Despite the evident success of M_{c1} scaling, however, it is still possible that there are additional effects depending on whether or not the low speed flow is subsonic or supersonic. Nevertheless, it is plausible that these are smaller effects and that M_{c1} scaling still describes the basic phenomenon.

A more serious problem with this argument concerns the meaning and determination of the convection velocity u_c. As was discussed in the introduction, it is difficult to identify large-scale structures in compressible shear layers given the available data. This lack of well-defined structures makes it difficult to justify a unique convection velocity for the turbulence in the shear layer. Even if the existence of such structures is accepted, however, there remain difficulties with interpreting the available data. The standard model (Dimotakis 1984, Coles 1985 and Papamoschou & Roshko 1988) is based on the idea of pressure matching at the stagnation points between structures in a reference frame moving with those structures (Fig. 2.3). Given this picture, the total pressures of the two free streams must balance at the stagnation point; *i.e.*,

$$p_{t1} \simeq p_{t2} \,, \tag{2.2.11}$$

where

$$p_{ti} = p_i \left[1 + \frac{(\gamma_i - 1)}{2} \left(\frac{u_i - u_c}{a_i} \right)^2 \right]^{\gamma_i/\gamma_i - 1} \qquad i = 1, 2 \,, \tag{2.2.12}$$

assuming that an isentropic streamline can be traced from the free stream to the stagnation point. Alternatively, Eq. 2.2.12 can also be used for non-isentropic streamlines, which is almost certainly the case for a real shear layer, provided that the total pressure losses on each side are approximately equal (Dimotakis 1989).

However, this symmetrical pressure-loss idea is not confirmed by experiment. In fact, the results of Papamoschou (1989) suggest that quite the opposite is true for compressible shear layers. Using double-spark Schlieren photography, he was able to track turbulent features in the flow and to compute convection velocities. The results (Fig. 2.4) clearly show that the turbulent features convect at speeds very close to one free stream velocity or the other in the compressible regime. Note that isentropic pressure matching (*i.e.* Eqs. 2.2.11 and 2.2.12) for equal static pressures yields $M_{c1} = M_{c2}$ for $\gamma_1 = \gamma_2$, and that even when $\gamma_1 \neq \gamma_2$, the two isentropically computed convective Mach numbers are almost equal. If the pressure-matching argument is valid, then the experimental results imply that the non-isentropic pressure losses in the two stream are not equal. This has led both Papamoschou (1989) and Dimotakis (1989) to speculate that shock waves exist on *one* side of the shear layer, thereby providing a mechanism for unequal pressure losses. These waves would presumably be the same as those seen in supersonic jet flows (Lowson & Ollerhead 1968, Tam 1971 and Oertel 1979), although curiously enough, they were not detected in any shear layer experiment prior to the current research.

The final point to be discussed in this section concerns the effects of heat release on the growth rate of the turbulent shear layer. For incompressible shear layers, the data of Hermanson & Dimotakis (1989) demonstrated that although the displacement thickness of the shear layer, δ_*, increases with increasing heat release q, the overall growth rate *decreases*. Dimotakis (1989) has suggested an equation for this behaviour; *i.e.*,

$$\frac{\frac{\delta}{x}(q)}{\frac{\delta}{x}(0)} \simeq 1 - 0.05q \ , \tag{2.2.13}$$

where

$$q \equiv \frac{\Delta\rho}{\rho} \tag{2.2.14}$$

and $\Delta\rho$ is the density change that is due to heat release. This result, though perhaps counter-intuitive, is not large and suggests that the growth rate is not very sensitive to heat-release effects. One of the purposes of the current research effort is to test this hypothesis in compressible flow.

2.3 Entrainment and Molecular Mixing

Large-scale structures have been recognized to play an important role in the entrainment processes of incompressible turbulent shear layers; in particular, models for entrainment based on the kinematic effects of such structures are in reasonable agreement with the available data (Dimotakis 1984, Coles 1985). In this section will be presented a brief description of the basic mechanisms and equations for both entrainment and molecular mixing. More detailed descriptions can be found in the models of Broadwell & Breidenthal (1982), Dimotakis (1987) and Broadwell & Mungal (1988, 1990).

A key observation, made by Brown & Roshko (1974), is that large parcels of free stream fluid from both sides exist inside the shear layer, and at times almost penetrate to the opposite side. This suggested the need to distinguish between entrainment, in which this unmixed, irrotational fluid is "gulped" up into the layer, and mixing, in which this fluid is "digested" by the action of small scale-turbulence and molecular diffusion inside the shear layer. The importance of molecular diffusion in the mixing process needs to be emphasized because it is the *only* mechanism that can mix the two fluid streams at a *molecular level.* Moreover, it is this molecular mixing that is a prerequisite for chemical reactions to occur inside the shear layer.

The rate of molecular mixing depends on two factors in a given flow: the magnitude of the concentration gradient and the amount of interfacial area between the two fluids. Both factors, in fact, are related to the action of small-scale turbulence inside the shear layer. Such turbulent motions stretch and fold the interface between the two fluids, thereby increasing the interfacial area and thinning the diffusion length scales at this interface. That such small-scale turbulence does indeed govern the rate of molecular mixing can be seen from the work of Konrad (1976), Breidenthal (1981), Bernal & Roshko (1986) and Koochesfahani & Dimotakis (1986). They found a transition process in the turbulent shear layer over the range $5 \times 10^3 < Re_\delta < 2 \times 10^4$, in which the amount of molecular mixing increased from negligible amounts to a substantial fraction of the fluid inside the layer. This transition is caused by the onset of three-dimensional instabilities in the flow which produce counter-rotating streamwise vortices superimposed on the underlying two-dimensional structure. The net result is a very rapid increase in the interfacial surface area between the two fluids with an associated increase in the rate of molecular mixing.

Inside the shear layer, this molecular mixing is found to occur at all compositions ranging from pure high speed to pure low speed fluid (Konrad 1976, Kooches-

fahani & Dimotakis 1986). At a streamwise location x, this distribution can be quantified in terms of the probability density function, $p(\xi, y)$, where ξ is the mole fraction of high-speed fluid in an infinitesimal[‡] volume at location y. A sketch of $p(\xi)$ for equal density ($s = 1$) flow (from Dimotakis 1989) is shown in Fig. 2.5. Note that this PDF is assumed to be spatially averaged across the shear layer, and that $\xi = 0$ corresponds to pure (unmixed) low-speed fluid, while $\xi = 1$ corresponds to pure high-speed fluid. This PDF illustrates four key properties of the molecular mixing inside a turbulent shear layer:

1. All mixture fractions ξ are present.
2. *Unmixed* fluid ($\xi = 0$, $\xi = 1$) can be found.
3. The PDF has a pronounced central peak.
4. The PDF is not symmetrical about $\xi = 0.5$.

This latter point indicates that high-speed fluid (in this example) is preferentially entrained into the layer for $s = 1$ flow. Quantitatively,

$$\bar{\xi} = \int_0^1 \xi \, p(\xi) \, d\xi \, , \tag{2.3.1}$$

where $\bar{\xi}$ is the average high-speed fluid mole fraction across the layer. $\bar{\xi}$ is related to the overall molar entrainment ratio, E, into the shear layer; *i.e.*,

$$\bar{\xi} = \frac{E}{E+1} \, , \tag{2.3.2}$$

where

$$E = \frac{\dot{n}_1}{\dot{n}_2} \tag{2.3.3}$$

and $\dot{n}_i$ is the molar flux of fluid from stream i into the shear layer. In this example (Fig. 2.5), $\bar{\xi} \simeq 0.57$ and $E \simeq 1.3$. Now, it must be emphasized that the average mole fraction in the *molecularly mixed* fluid, $\bar{\xi}_m$, is not necessarily equal to the overall average mole fraction, $\bar{\xi}$ (Hermanson & Dimotakis 1989, Dimotakis 1989). Here we define $\bar{\xi}_m$ to exclude the unmixed fluid; *i.e.*,

$$\bar{\xi}_m \equiv \int_\epsilon^{1-\epsilon} \xi \, p(\xi) \, d\xi \, , \tag{2.3.4}$$

---

‡ Subject to the limitations of the continuum approximation, of course.

where ϵ is small in some sense. A mixed fluid entrainment ratio, E_n, can be computed from $\bar{\xi}_m$; *i.e.*,

$$E_n = \frac{\bar{\xi}_m}{1 - \bar{\xi}_m} \quad . \tag{2.3.5}$$

Experimentally, it is found that E_n is a function of r and s in incompressible shear layers. Dimotakis (1984) has suggested a model for this phenomenon, which yields

$$E_n \simeq \frac{1}{s} \frac{w_2}{w_1} \frac{u_1 - u_c}{u_c - u_2} \left(1 + \frac{l}{x}\right) , \tag{2.3.6}$$

where l/x is the mean large-scale structure spacing-to-position ratio and w_i is the molecular weight. Note the implicit assumption that $p_1 = p_2$. A fit of the available incompressible data for l/x yields (Dimotakis 1984)

$$\frac{l}{x} \simeq 0.68 \frac{1 - r}{1 + r} , \tag{2.3.7}$$

allowing for the estimation of E_n based on the specified free stream parameters and u_c. For *compressible* flows, it is plausible that this equation is also applicable, provided that l/x is suitably scaled. Lacking conclusive measurements, it will be assumed here that compressibility scales l/x in exactly the same way that it scales δ/x (Dimotakis & Hall 1987, Dimotakis 1989).

A simplified version of the PDF in Fig 2.5 is used in the models of Broadwell & Breidenthal (1982) and Broadwell & Mungal (1988), the major difference being that the central peak in the PDF is represented by a delta function. This model lends itself to a simplified physical interpretation of the fluid distribution inside the layer. The basic idea is that molecularly mixed fluid resides in two distinct locations inside the shear layer (Fig. 2.6). One location is the thin, planar diffusion zone between vortices, alternatively known as a flame sheet or a Taylor layer. The second location is in the core of a shear layer vortex. The vortex cores are thought to be homogeneously mixed at an overall entrainment ratio E, because of the combined action of high strain rate (rapid production of interfacial surface area) and molecular diffusion. The time series data of Mungal & Dimotakis (1984) support this view, showing regularly spaced, almost uniform temperature regions (*i.e.*, homogeneously mixed vortex cores) in the shear layer. Therefore, in this description, the homogeneous vortex cores account for the peak in $p(\xi)$ roughly centered on $\bar{\xi}$, and the flame sheets account for the rest of the distribution.

In the absence of precise knowledge of $p(\xi)$, chemical reaction data can be used to estimate some of the macroscopic parameters of the flow. Of particular importance are E_n and δ_m/δ, which are, respectively, the mixed-fluid entrainment ratio and the overall fraction of molecularly mixed fluid in the shear layer. The methodology is based on the so-called "flip" experiment in which grossly unequal reactant concentrations are used in the two free streams (Mungal & Dimotakis 1984, Koochesfahani & Dimotakis 1986). Note that the reactants must be diluted by some inert carrier fluid for this to be possible. This inequality is quantified in terms of the stoichiometric mixture ratio ϕ defined by

$$\phi \equiv \frac{X_2/X_1}{(X_2/X_1)_{\rm st}} \ , \tag{2.3.8}$$

where X_i is the free stream mole fraction of reactant i, and the subscript 'st' denotes a stoichiometric mixture. For example, a flow with $\phi = 1/4$ denotes that 4 parts of low-speed fluid must be mixed with 1 part of high-speed fluid in order to consume *all* of the reactants. This particular circumstance results in the *maximum* heat release possible, corresponding to a temperature rise known as the adiabatic flame temperature, $\Delta T_{\rm flm}(\phi)$.[♯] This occurs at a mixture fraction $\xi = \xi_\phi$, where

$$\xi_\phi = \frac{\phi}{\phi + 1} \ . \tag{2.3.9}$$

Any given experiment will yield a result for the average chemical product mole fraction, δ_P/δ, obtained from the cross-stream temperature profile; *i.e.*,

$$\frac{\delta_P}{\delta}(\xi_\phi) = \frac{1}{\delta}\int_{-\infty}^{\infty} \frac{\Delta T(y,\xi_\phi)}{\Delta T_{\rm flm}(\xi_\phi)}\, dy \ , \tag{2.3.10}$$

where the functional dependence of $\xi_\phi(\phi)$ is noted. A typical "flip" experiment will consist of a $\xi_\phi = \xi_0 \to 0$ run and a $\xi_\phi = \xi_1 \to 1$ run. The results for $\delta_p(\xi_0)/\delta$ and $\delta_p(\xi_1)/\delta$ can be used to estimate E_n and δ_m/δ as follows:

$$\frac{\delta_m}{\delta} \simeq \frac{(1-\xi_0)}{\delta}\left[\delta_P(\xi_0) + \delta_P(\xi_1)\right] \ , \tag{2.3.11}$$

$$\bar{\xi}_m \simeq \frac{\delta_P(\xi_1)}{\delta_P(\xi_0) + \delta_P(\xi_1)} \tag{2.3.12}$$

♯ This is strictly true only for equal heat and species diffusivities; *i.e.*, $Le \equiv \kappa/\mathcal{D} = 1$.

and E_n follows from Eq. 2.3.5. For the derivation of Eqs. 2.3.11 and 2.3.12, the reader is referred to Dimotakis (1987) or Dimotakis (1989). Note that these equations are strictly valid only for negligible heat release and constant molar heat capacities across the layer. A more general discussion appears in Frieler & Dimotakis (1988).

On the basis of the measurements of Frieler & Dimotakis (1988), it was found that

$$\frac{\delta_m}{\delta} \simeq 0.49 \tag{2.3.13}$$

for gas phase shear layers at $r = 0.4$. This value was found to be independent of the density ratio, but it decreased slightly with increasing Re_δ. This value can be contrasted with that found by Koochesfahani & Dimotakis (1986) for water shear layers; *i.e.*,

$$\frac{\delta_m}{\delta} \simeq 0.26\,. \tag{2.3.14}$$

This difference is attributable to the difference in molecular diffusivity between the two media. In terms of the dimensionless Schmidt number, S_c, defined here as

$$S_c \equiv \frac{\nu}{\mathcal{D}}\,, \tag{2.3.15}$$

$S_c \simeq 600$ in water versus $S_c \simeq 0.7$ in gas phase flows (Dimotakis 1989).

The preceding discussion was based on incompressible flow experiments. The effect of compressibility on the mixing transition, the entrainment ratio and the molecular mixing was basically unknown at the inception of the present study and therefore served as a major motivating influence.

2.4 Chemical Kinetics

The issue of chemical kinetics was without question the most important design driver for the new facility. The problem it posed was that for a variety of purposes, it is desirable to ensure that most (or all) of the molecularly mixed fluid in the shear layer completes its chemical reactions within the confines of the combustion chamber or test section. There are two pertinent time scales to be considered: τ_x, which is the time of flight of the mixed fluid through the test section; and τ_c, which is the time required for chemical reactions. The ratio of these two time scales is the Damköhler number (Da):

$$Da \equiv \frac{\tau_x}{\tau_c}\,. \tag{2.4.1}$$

For $Da \ll 1$, relatively little chemical product would be formed; for $Da \gg 1$, essentially all of the molecularly mixed fluid would have sufficient time to complete chemical reactions.

This second limit is known as the "fast-chemistry limit". In this regime, the chemical reactions are so fast that the time lag between molecular mixing and chemical product formation is negligible. Therefore, reacted fluid becomes a marker for mixed fluid. This equivalence can be carried one step further. For exothermic reactions, chemical product formation is accompanied by heat release. The resultant temperature rise of the fluid therefore marks the presence of chemical products, which in turn, indicate molecularly mixed fluid. Hence, in this limit, one can use a thermometer to measure molecular mixing. This use of chemistry as a diagnostic for molecular mixing is arguably the best such way to measure molecular mixing. It has been successfully applied to water flows (acid-base reactions) by Breidenthal (1981) and Koochesfahani & Dimotakis (1986), and to gas phase flows by Wallace (1981), Mungal & Dimotakis (1984), Frieler & Dimotakis (1988) and Hermanson & Dimotakis (1989). The use of δ_P/δ measurements from flip experiments to estimate E_n and δ_m/δ (described in the last section) is predicated on the existence of fast chemistry in the experiments.

The other important feature of the fast-chemistry limit is that it represents maximum chemical product formation. At all locations within the shear layer, the lean reactant is completely consumed in the molecularly mixed fluid. The energy release per unit mass can be increased only by increasing the amount of molecular mixing. For this reason, this limit is also known as the "mixing-limited regime". Clearly, one wishes to operate any kind of engine (*e.g.*, SCRAMJET) in this regime.

There are many obstacles to fast chemistry in compressible turbulent shear layers. Chief among them is the very high convection velocity (u_c), which generally accompanies compressible flow. Note that u_c and τ_x are inversely related; *i.e.*,

$$\tau_x \sim \frac{L}{u_c} , \tag{2.4.2}$$

where L is the length of the combustion chamber or test section. Using the new wind tunnel facility as an example, $u_c \sim 1000\ m/s$ and $L \sim 1\ m$, yielding flight times on the order of $\tau_x \sim 1\ ms$. Since high velocities are inherent in this kind of flow, the only way to increase τ_x is to increase the length L. Of course, geometrical scaling has its own problems, primarily cost, mass and skin friction (for flight vehicles).

An alternative way to achieve fast chemistry is to ensure that the characteristic chemical time (τ_c) is sufficiently small. Lacking any published data on chemical times in compressible shear flows, it became necessary to extrapolate the data available from incompressible flows, primarily the study done by Mungal & Frieler (1988). The methodology employed by Mungal & Frieler consisted of two parts: First, a theoretical computation was performed using a constant mass flow/kinetics model to estimate τ_c; second, experimental values of τ_x and chemical product formation were obtained to yield a functional dependence between chemical product formation and the Damköhler number. As a result of their analysis, they concluded that the fast chemistry limit was attained when $Da > 40$.

This methodology was repeated in the current research effort. A revised model was employed (Dimotakis & Hall 1987), which attempted to incorporate the first-order effects of entrainment. This model will be briefly described below.

Both flow/kinetics models are based on the idea that much of the molecularly mixed fluid in the shear layer resides in homogeneously mixed vortex cores, as was described in the previous section. On this basis, one can postulate a combustion model that considers *only* these homogeneous regions, ignoring all other contributions (*i.e.*, flame sheets) to chemical product formation. Such a model is therefore concerned with the temporal evolution of a homogeneously mixed mass of fluid, also known as the "well-stirred reactor problem". The resultant mathematical description consists of a system of first-order, ordinary differential equations that can be solved by numerical integration.

The continuity and energy equations form the basis of this model. There is one continuity equation for each chemical species i of the form

$$\dot{n}_i = \dot{n}_{ci} + \dot{n}_{ai} \,, \tag{2.4.3}$$

where the dot denotes time differentiation, n_i is the number of moles of species i in the "reactor", $\dot{n}_{ci}$ is the rate of production of n_i that is due to chemical reactions, and $\dot{n}_{ai}$ is the addition rate of n_i that is due to new mass being added to the reactor (entrainment). Estimates for the $\dot{n}_{ai}$ can be provided by Eq. 2.2.3, suitably scaled for the effects of compressibility (Fig. 2.2), and Eq. 2.3.6. Note that it is highly speculative to extrapolate Eq. 2.3.6 to compressible flow; hence, many of the preliminary design calculations simply assumed that $E_n = 1$.

The overall chemical production of species i is generally a sum of many simple reactions. Table 2.1 is an example of this, showing the detailed reaction mechanism

that is believed to describe hydrogen-fluorine-nitric oxide ($H_2/F_2/NO$) chemistry. Each chemical production rate can be written in the form

$$\dot{n}_{ci} = V \sum_j k_{fj} \prod_\alpha [c_\alpha]^{b_\alpha} \ , \tag{2.4.4}$$

where k_{fj} is the forward rate coefficient of the j^{th} reaction, $[c_\alpha]$ is the molar concentration of species α that participates in the j^{th} reaction; *i.e.*,

$$[c_\alpha] \equiv \frac{n_\alpha}{V} \ , \tag{2.4.5}$$

where V is the total volume of the reactor; and b_α is the stoichiometric coefficient of species α in reaction j. A sample equation is explicitly written out in Table 2.1 for the production of HF in this chemical system.

The forward rate coefficient k_{fj} is typically derived from laboratory measurements that have been fitted to an equation of the form

$$k_{fj} = A_j T^{\beta_j} \ \exp\left[-E_j/R_o T\right] , \tag{2.4.6}$$

where R_o is the universal gas constant, T is the temperature of the reactor fluid, and A_j, β_j and E_j are the fitted constants. This equation is known as the Arrhenius relation for reaction rates. Unfortunately, variances in the k_{fj} are often in the range of $\pm 100\%$ because of the difficulty in performing these kinetics experiments. The constants for the $H_2/F_2/NO$ reactions are listed in Table 2.1. Note that each of the reactions listed also proceeds in *reverse*, with a rate coefficient given by

$$k_{rj} = \frac{k_{fj}}{k_{ej}} \ , \tag{2.4.7}$$

where k_{ej} is the equilibrium constant for the j^{th} reaction.

The energy equation for this reactor model can be written in the form

$$\frac{d}{dt} \int_V h \, dn = \sum_i h_{ai} \dot{n}_{ai} \ , \tag{2.4.8}$$

where h is the enthalpy (per mole), n is the number of moles of the reactor fluid, and h_{ai} and $\dot{n}_{ai}$ are the total enthalpy and rate of molar addition of species i to the reactor. Note that h_{ai} for free stream k is given by

$$h_{ai,k} = h_{si} + \frac{1}{2} w_i |u_k - u_c|^2 \ , \tag{2.4.9}$$

where h_{si} is the static enthalpy and w_i is the mean molecular weight of species i in free stream k. Eq. 2.4.8 is derivable from a control volume analysis at constant pressure and simply states that the total energy of the reactor can change only by energy addition from outside. It can be re-written in terms of temperature, which is a more convenient independent variable. Specifically,

$$\dot{T} = \frac{1}{\sum_i n_i C_{p_i}} \left\{ \sum_i h_{ai} \dot{n}_{ai} - \sum_i h_i \dot{n}_i \right\}, \tag{2.4.10}$$

where C_{p_i} is the molar heat capacity of species i.

Equations 2.4.4 and 2.4.10 form a system of $(i+1)$ ordinary differential equations. A solution requires the initial conditions for T and the n_i, the chemical reaction mechanism, the rate coefficients and thermodynamic data for all species, specifically $C_p(T)$ and $h(T)$ (for perfect gases). For the current research, the actual computations were facilitated by the use of the CHEMKIN software package (Kee *et al.* 1980).

As has been foreshadowed by Table 2.1, $H_2/F_2/NO$ chemistry was chosen for this research. There were two reasons for this selection. First, $H_2/F_2/NO$ chemistry ranks among the fastest known, and even so, it will be shown that the attainment of the fast-chemistry regime in compressible flow is by no means certain. Second, $H_2/F_2/NO$ chemistry does not require ignition sources and will react at ambient temperatures and below. It should be added that both reasons also motivated the use of $H_2/F_2/NO$ chemistry in the earlier research efforts of Mungal & Dimotakis (1984), Frieler & Dimotakis (1988) and Hermanson & Dimotakis (1989). As with those efforts, NO is treated more as a catalyst than as a true reactant in the current experiments. Specifically, small concentrations of NO are needed to initiate the overall reaction by liberating fluorine atoms that can react with hydrogen molecules (Reaction 1 in Table 2.1). However, the concentrations of H_2 and F_2 are always much higher and serve as the basis for the definition of the stoichiometric mixture ratio (ϕ) in the reacting flow experiments.

Figure 2.7 presents a typical result of a kinetics computation describe above. The plot shows the temporal evolution of the reactor temperature for the fast kinetics condition of the Mungal & Frieler (1988) experiment.* It should be noted that not only has their flow model been revised to include entrainment in this calculation, but their reaction mechanism (Table 2.1) has been expanded to include

* An ambient temperature of 300 K was assumed for this calculation. The resultant ΔT was 93 K.

the *HNO* reactions. The temperature versus time curve has a characteristic "S" shape. The overall reaction requires some time to "get going", then it proceeds exponentially, reaching a nearly asymptotic state at some characteristic time τ_c. Here, τ_c is identified with the time required for completion of the chemical reaction (Eq. 2.4.1). It is estimated by drawing a tangent to the curve at its maximum slope (the dotted line, as shown) and extrapolating it to $\Delta T/\Delta T_\infty = 1$. It can be seen that this yields $\tau_c \simeq 3.9\ ms$ for this test condition, which combined with the Mungal & Frieler (1988) stated value of $\tau_x \simeq 20.8\ ms$ yields $Da \simeq 5.3$. This can be contrasted with the value of $Da \simeq 40$ quoted in their paper. Most of this change is due to the addition of the two *HNO* reactions to the model.

Figure 2.8 presents the computed results for a concentration study using the baseline $M_1 = 1.5$, $M_2 = 0.3$ flow with N_2 diluent. The static pressure was set to 1 atm, the stagnation temperatures were set to 295 K and the entrainment ratio was set to unity. The molar concentration of NO was held constant at 0.25%, while those of H_2 and F_2 were varied from 1% to 8%, the latter being close to the effective limit of the new experimental facility for F_2. The range of characteristic chemical times is seen to be $0.1\ ms < \tau_c < 5.6\ ms$. An estimate of u_c from Eq. 2.2.12 for this flow yields $u_c \simeq 277\ m/s$. Given $L = 0.38\ m$ for this facility (Section 3.4), this results in a predicted Damköhler number range of $0.2 < Da < 14$, which brackets the Mungal & Frieler (1988) fast-chemistry threshold value of $Da \sim 5.3$ for incompressible flow. These kinetics calculations will be compared to the experimental results in Chapter 5.

If the high-speed nitrogen is replaced with high-speed helium in the baseline case, the attainment of fast chemistry becomes less certain. For this flow, Eq. 2.2.12 yields $u_c \simeq 450\ m/s$. Assuming that the estimates for τ_c remain basically unchanged, this results in a Damköhler number range of $0.15 < Da < 8$. This only marginally brackets the fast-chemistry threshold value. However, Eq. 2.2.12 will probably not apply to this flow because of the expected *unequal* convective Mach numbers (*cf.*, Fig. 2.4). Resolution of this uncertainty requires experimental data; therefore, further discussion of this particular flow/kinetics condition will be postponed to Chapter 5.

2.5 Synopsis of Design Drivers

The major problem of attaining the fast-chemistry limit in a compressible turbulent shear layer made it the primary design driver for the new facility. Three key design decisions resulted from the analysis of this problem, all of them directed at making the chemical kinetics as fast as possible:

1. The $H_2/F_2/NO$ chemical system was chosen because of its inherently fast kinetics and because it is hypergolic.
2. The static pressure of the test section was set to 1 atm, the highest value possible given the other constraints on the facility. Note that the chemical production rate for HF scales like the *square* of the molecular number density (Eqs. 2.4.4, 2.4.5 and Table 2.1).
3. The exponential dependence of the reaction rate on temperature (Eq. 2.4.6) suggested the desirability of preheating the reactant gases in order to speed up the chemical kinetics. Although such preheating was not done in the current research, the capability for it was included in the facility as built. See Appendix A for details.

The other major design driver was the requirement of attaining high convective Mach numbers. In particular, the search for travelling shock waves in the flow required $M_c > 1$. The limiting factor in this regard was the high stagnation pressure required to drive the high-speed flow, given that the static pressure was already set to 1 atm. The pressure limit finally chosen allows for a maximum free stream Mach number of roughly 3, which in turn allows for a maximum isentropically estimated convective Mach number in the range of 1.5 to 2 depending on the gases flowed.

These primary design drivers were sufficient to determine the basic configuration of the new facility. As was mentioned in the Introduction, what resulted is a two-stream, blowdown wind tunnel capable of producing supersonic, reacting shear layers with $H_2/F_2/NO$ chemistry. It is a high-pressure, high mass flux facility with the capability for preheating the gas of the high-speed stream. The details of this facility will be described in the next chapter.

CHAPTER 3
Facility Description

3.1 Overview

The new experimental facility incorporated some of the elements of an earlier laboratory, which was used to study incompressible, reacting, planar shear layers (Mungal & Dimotakis 1984, Hermanson & Dimotakis 1989, Frieler & Dimotakis 1988). Both the old and the new components will be described in the following sections.

The new facility is a two-stream, blowdown wind tunnel with a nominal run time in the range of two to five seconds. Figures 3.1 and 3.2 are, respectively, north- and west-looking photographs of the facility, with the author included for scale. Figure 3.3 shows most of the major components in a floor-plan layout, and Fig. 3.4 presents a simplified flow schematic.

The basic operation of the facility is as follows: Various compressed gases are loaded into the H_2/NO and F_2 Reactant Tanks at the desired pressures and compositions. Fast-acting valves are then opened at the start of the experiment, allowing this gas to flow through parallel piping networks and into the test section. Specially designed nozzles bring these two gas streams together in a two-dimensional mixing layer geometry. A variety of instruments measure the many flow parameters at this point, after which the gas exhausts into the waste-gas disposal system.

The facility is comprised of five major subsystems:

1. Low-speed fluorine gas delivery network.
2. High-speed hydrogen/nitric oxide gas delivery network.
3. Test section and diagnostics
4. Waste-gas disposal system.

5. Run-time control, data acquisition and data processing.

A brief discussion of each will be given in the remainder of the chapter. Further details may be found in Appendix A, and in Hall & Dimotakis (1989).

3.2 Low Speed Fluorine Gas Delivery Network

Most of the hardware for this subsystem was taken from the old laboratory (Mungal & Dimotakis 1984). In addition, the laboratory procedures for the safe handling of fluorine gas developed during the previous research program were incorporated here.**

Loading of the gas on this side is accomplished in a two-step process. The F_2 and inert diluent gases (N_2, Ar, He) are first loaded into the F_2 Mixing Vessel (Fig. 3.4). This vessel is a 0.1 m (4 in) diameter by 4.88 m (16 ft) long pipe with a small, 1.25 cm (0.5 in) diameter perforated tube on its axis. The total volume of the Mixing Vessel is 0.04 m^3 (1.4 ft^3). Gas entering this vessel flows down the small axial tube and is then injected radially through the perforated holes. This helps to mix the different gases inside the tank. Partial pressure measurements are used to set the concentrations of the constituent gases to a relative accuracy of $\simeq 1\%$.

In the second step of the loading process, the gas mixture is transferred from the mixing vessel to a Teflon bag located inside the F_2 Reactant Tank. The outside of this bag is connected via a 0.15 m (6 in) diameter pipe to a very large, 12.7 m^3 (450 ft^3) pressure vessel called the Surge Tank. The Surge Tank, when filled with N_2, acts like an almost constant pressure source during an experiment ($\sim 5\%$), squeezing the gas out of the Teflon bag and into the test section. This arrangement not only removes the need for a pressure regulator, it also isolates the F_2 gas from the Teflon-coated wall of the F_2 Reactant Tank, adding yet another level of safety. The F_2 Reactant Tank itself has an internal volume of approximately 0.57 m^3 (20 ft^3) and is rated for 800 kPa (115 $psig$) working pressure. Note that the difference in volume between the two tanks requires that the Mixing vessel be filled and discharged several times in order to fill the F_2 Reactant Tank. This design feature helps to flush the F_2 out of the Mixing Vessel and into the F_2 Reactant Tank. Once the gases have been completely loaded into the F_2 Reactant Tank, they are allowed

** See the discussion in Appendix A of Mungal (1983).

to settle and mix for at least half an hour in order to produce a homogeneous mixture.

During an experimental run, the low-speed gas mixture flows through a 7.5 cm (3 in) diameter stainless steel pipe and a pair of valves before it reaches the test section. The first valve is a pneumatically actuated globe valve with an opening time of $\simeq 0.5$ sec. It serves as the shutoff valve. The second valve is an adjustable sonic metering orifice that controls the mass flux. This metering valve consists of two concentric cylinders, the inner one of which has a large number of 1/8 inch (3 mm) diameter holes drilled in it. By moving the two cylinders axially with respect to each other, the number of holes exposed to the flow is changed, thereby changing the effective orifice area of the valve. Immediately downstream of this valve is a 7.5 cm (3 in) thick stack of high-porosity aluminum mesh screen, which acoustically damps the flow just before it enters the test section.

3.3 High Speed Hydrogen/Nitric Oxide Gas Delivery Network

This delivery network also operates on the blowdown principle. Because of the high volumetric fluxes, however, it is not practical to provide a large enough tank to serve as a constant pressure source, as is done with the Surge Tank in the F_2 gas delivery system. This requires a pressure regulator in the flow, which will compensate for the falling pressure in the reactant tank during an experiment.

Loading of the high-speed gas mixture is done directly into the H_2/NO Reactant Tank (Fig. 3.5). This tank has approximately 1.2 m^3 (42 ft^3) of internal volume and is designed for a working pressure of 100 atm (1500 psi) at a maximum temperature of 600 K (620 ^oF). Most of the tank interior is filled with aluminum mesh screen in the form of two cylindrical rolls.[†] This packing is used to minimize the gas temperature drop during blowdown. As with the low-speed side, partial pressure measurements are used to set the concentrations of the constituent gases. Mixing of the different gases is enhanced by injecting along the axis of the tank, which is free of screen packing. This injected gas entrains the gas already in the tank and pumps it to the top of the tank. This creates a circulating flow with gas rising along the axis and falling through the screen along the tank circumference, thereby promoting mixing. Once completely loaded, the gas is allowed to settle and mix for at least half an hour.

[†] The volume fraction occupied by the metal is roughly 10%.

As is the case for the low speed side, the gas mixture from the H_2/NO Reactant Tank flows through a shutoff valve, a regulating valve and an acoustic dampener before it reaches the test section. A 10 cm (4 in) diameter stainless steel pipe connects all of these elements. The shutoff valve is a stainless steel, full port, 10 cm (4 in) ball valve manufactured by the VALVTRON company. It is a metal-seated valve, and therefore is compatible with high temperature fluids. A ROTORK pneumatic actuator is used to open this valve, with an opening time of $\simeq 1$ sec.

The pressure regulator is an in-house designed, constructed and tested device (Fig. 3.6).‡ It is a dynamic equivalent to the passive metering valve employed on the low speed side. This valve also uses two concentric cylinders, but in this case, the inner one *rotates* inside the outer one. There are ten slots cut into each of these two cylinders in matching patterns. These slots are grouped into pairs at five equally spaced azimuthal positions. The degree of alignment of the rotor/stator slot openings determines the effective flow orifice area and the resultant pressure drop. Since this is an active device, it requires a precisely controllable motor that will rotate the inner cylinder in a prescribed manner. A Compumotor KH-740 servo-motor is used for this task (Appendix A). Closed-loop feedback control is employed to determine the required rotor position as a function of time during an experiment. Details on this control system can be found in Section 3.6.

Acoustic damping is provided by a 2 m (6.3 ft) long pipe lining downstream of the pressure regulator. This configuration is essentially a silencer, consisting of an annulus of aluminum mesh screen sandwiched between the pipe wall and a cylindrical perforated plate.

3.4 Test Section and Diagnostics

A cutaway drawing of the test section is presented as Fig. 3.7. It is constructed almost entirely from 8.75 cm (3.5 in) thick 6061-T6 aluminum plate, with the exceptions to be noted as follows. The flow is from left to right in the drawing with the high-speed stream on top. The span is 15 cm (6 in). The two settling chambers and flow management sections are identical. A perforated cone is used to diffuse the incoming flow, followed in sequence by a pair of coarse mesh screens, honeycomb and lastly, a pair of fine mesh screens. The specifications for all of these elements can be found in Appendix A.

‡ The mechanical design was largely the work of Cliff Frieler and Tom Sobota.

Aluminum 2219-T8 plate is used for the two nozzle blocks. They were cut on a computer-controlled milling machine. The splitter plate is constructed from 17-4 PH stainless steel and hardened to condition H900. All of the subsonic contours were computed using a GALCIT Laplace solving code for inviscid flow (Pepin & Dimotakis 1989). The supersonic contour was calculated using an AEDC design code (Sivells 1978). The high-speed contraction ratio is 7.5 (for the $M_1 = 1.5$ nozzle), and the low-speed contraction ratio is 4.0 . The nozzle exit heights are 31.8 mm and 50.8 mm (1.25 and 2.0 in) respectively.

The shear layer itself forms at the end of the splitter plate and is bounded by 17-4 PH stainless steel guidewalls on the top and bottom, and by optical windows on the sides. The guidewalls are adjustable, with an elastic flexure joint and screw jack mechanism as shown in Fig. 3.7. This adjustment provides the means to affect the streamwise pressure gradient. The optical windows are composed of two pieces. The outer piece is a 50.8 mm (2 in) thick BK7 optical window designed to take a worst-case pressure loading of 5 atm.[♯] The inner piece is a 3.2 mm ($\frac{1}{8}$ in) thick polished pyrex window designed to protect the BK7 glass from the corrosive effects of F_2 and HF gases. The pyrex is also susceptible to F_2 and HF etching, but it is inexpensive enough to be considered disposable when the optical quality has deteriorated beyond usability.

In the present configuration (Fig. 3.7), the shear layer effectively ends 0.38 m (15 in) downstream of the splitter tip.* An instrument rake is located at that position, comprised of two parallel rows of 16 - 1.6 mm ($\frac{1}{16}$ in) diameter tubes aligned across the flow in the y-direction. One row of tubes is connected to 16 pressure transducers (Druck model PDCR 200) to provide a mean total pressure profile of the flow. The second row of tubes supports 25 μm (0.001 in) diameter, chromel/alumel exposed-junction thermocouples, which provide a mean total temperature profile of the flow (Appendix A). After the shear layer gases flow past this instrument rake, they exhaust into the shower tunnel (Section 3.5).

Another diagnostic used in this experiment is side-view Schlieren photography. A folded optics system is employed (Fig. 3.8), which can image a 25 cm (10 in) diameter region of the test section.** Hence, two photographs are required to image the complete shear layer. A 20 $nsec$ duration spark source (Xenon N-789B

[♯] With a safety factor of ten.

* The maximum possible shear layer length in the test section is approximately 0.65 m.

** This system was originally constructed by Jim Hermanson for use in the old HF laboratory.

nanolamp) provides the illumination, and a motor-driven Nikon FE 35 mm camera receives the image. All pictures are recorded on Ilford XP1-400 black and white film.

The remaining diagnostics consist of two types of pressure transducers mounted on the centerlines of the two adjustable guidewalls (See Appendix A, Fig. A4) The first type of transducer is a fairly low-frequency response model (Druck PDCR 200 and PDCR 900) designed to measure the mean streamwise pressure gradient. Seven such transducers are mounted in each guidewall spanning from the hinge to the instrument rake. The second type of transducer is a 1 MHz response piezoelectric device (PCB model 113A21), mounted four per guidewall. These transducers provide time-resolved data for the pressure fluctuations in the test section.

Details on the data acquisition and processing can be found in Section 3.6.

3.5 Waste Gas Disposal System

The presence of toxic and corrosive gases in the exhaust flow (HF, F_2, NO, NOF, $etc.$) requires a waste-gas treatment capability for the laboratory. This capability is provided by a concentrated solution of sodium hydroxide in water,[†] which is sprayed into the exhaust gases via high-pressure shower nozzles. Since all the toxic gas components form acids in water, the alkaline $NaOH$ serves to neutralize them.

In practice, this treatment follows a three step-procedure:

1. The exhaust gas from the test section flows through the shower tunnel and into the catch bag. This gas is sprayed "on the fly" here, starting the neutralization process as well as evaporatively cooling the hot combustion products.
2. All of the gas is then collected in the inflatable catch bag. More showers are located here, spraying the gas until neutralization is completed.
3. The scrubbed exhaust gases, consisting of diluent gases and unreacted H_2, are vented to the atmosphere. Note that the concentration of H_2 is always diluted below the flammability limit[‡] before venting.

[†] The pH was kept above 12.

[‡] Which is 4% H_2 in air.

The basic hardware configuration for this system is shown in Fig. 3.4. More details can be found in Appendix A.

3.6 Run-time Control, Data Acquisition and Data Processing

Two DEC LSI-11/73 CPU based, RT-11 computers are used for the run-time experiment control and data acquisition. The first computer is used to sequence the experiment by opening and closing the shutoff valves, starting the camera and the analog-to-digital conversion (A/D) boards, and performing the closed-loop feedback control for the high-speed stream pressure regulator (Section 3.3). The second computer is dedicated to test section data acquisition, 32 channels in all. Both are networked, via Ethernet, to a VAX/VMS cluster used to process the data.

The closed-loop feedback control of the main pressure regulator is based on a proportional-integral-derivative (PID) algorithm.[♯] In essence, one measures the actual pressure as a function of time, compares it to the desired pressure and computes corrective action based on the difference, the integral and the derivative of the two values. Specifically,

$$\Delta\theta = G_P(p_p - p_r) + G_I \int_0^t (p_p - p_r)dt + G_D \frac{d}{dt}(p_p - p_r) \,, \tag{3.6.1}$$

where $\Delta\theta$ is the corrective action to be implemented (change in rotor angle), p_p is the measured pressure, p_r is the required pressure (user-specified) and G_P, G_I and G_D are the proportionality constants (the gains).

In practice, the gains were determined by trial and error over a large number of tests. Attempts to model the non-linear dynamics of this flow system and to employ modern control theory have been, as yet, unsuccessful. Nevertheless, a simple continuity analysis is critical in predicting the approximate open-loop control for this problem. In this analysis, the mass flux through the test section nozzle is specified (via the Mach number); in a steady-state condition, this mass flux must also flow through the regulator valve. To the extent that the regulator acts like a

---

[♯] The electronics needed to drive the customized pressure regulator were designed by Dan Lang and built by Alan Goudey and Dan Lang. Paul Dimotakis was responsible for the basic control algorithm and, with Dan Lang, wrote the required assembly language macros. Credit is also due to Henning Rosemann for coding the algorithm and debugging the final software.

sonic metering orifice, one has only to set the effective flow area (A_{eff}); *i.e.*,

$$\dot{m} = A_{\text{eff}}\, p_t \sqrt{\frac{\gamma}{RT_t}} \left[\frac{\gamma+1}{2}\right]^{\frac{-1}{2}\frac{(\gamma+1)}{(\gamma-1)}}, \tag{3.6.2}$$

where $\dot{m}$ is the mass flux, p_t is the upstream total pressure, T_t is the total temperature, R is the gas constant and γ is the ratio of specific heats. The final algorithm uses this equation to estimate the regulator behaviour and then applies the PID controller to *correct* for the inherent inaccuracies. This can be viewed as a linearization of the true non-linear system about the quasi-steady-state operating point.

Three pressure transducers (Druck model PDCR 130) are used to provide the inputs for the control program. They are located at the H_2/NO Reactant Tank, the regulator exit (*i.e.*, immediately downstream of it) and the plenum chamber of the test section. The analog data are converted to digital form by a Data Translation DT 2757 16-bit A/D board. The converted data are used by the control program and then stored for post-run analysis. The output of the control program consists of a value for the clock frequency that drives the servo-motor. An in-house designed electronic circuit generates the clock signal and serves as the hardware interface between the computer and the servo-motor.

For data acquisition, all test section pressure and temperature signals, except for the PCB transducers, are fed into a multistage, low-noise amplifier circuit and low pass filter. The 3-pole Butterworth filter knee is set to be one-half the sampling rate of 200 *Hz* per channel. There are 32 channels of data taken during each experiment, comprised half of temperature data, half of pressure data. The pressure data consist of a mixture of guidewall static pressures and rake total pressures. The output from the amplifier circuits is sent to a Data Translation DT 3362, 12-bit A/D board. One of the two computers is dedicated to operating this board and storing the data.

The data from the PCB transducers are recorded on a Nicolet oscilloscope. Only two channels, at 7680 data points per channel can be recorded per run in this fashion. The nominal sampling rate is 2 *MHz* per channel.

After an experiment, all data are transferred from the RT-11 machines to a μVAX computer for data processing. This processing is performed by in-house written software that incorporates many FORTRAN routines from *Numerical Recipes* (Press *et al.* 1989) and the IMSL Math Library (1989). Typically, the processing involves three steps:

1. Convert from A/D counts to engineering units, folding in the calibration data at the same time.
2. Compute average and rms values for each channel.
3. Fit the data and obtain spatial profiles.

Examples will be discussed in Chapters 4 and 5.

CHAPTER 4
Results For Non-Reacting Flows

4.1 Overview

This chapter will present and discuss results for the non-reacting experiments that were performed in this study. A list of the experiments discussed here can be found in Table 4.1. The test cases are listed in order from highest to lowest compressibility, as determined by the isentropic model for M_{c1} (Eqs. 2.2.11 and 2.2.12). All of the supersonic flows were generated with the same nozzle that produced a design free stream Mach number of 1.5. The variations between the supersonic test cases were produced by using different gases and different low-speed velocities (u_2). The subsonic runs were generated by using a subsonic nozzle in place of the supersonic nozzle.

Before proceeding with the discussion of the individual cases, it may be useful first to describe some aspects of the experimental procedure that were common to all of the experiments. The basic goal was to produce straight, nominally self-similar shear layers with zero streamwise pressure gradient. The values listed in Table 4.1 correspond to this condition in all test cases. The difficulty in achieving this condition stemmed from the fact that no theory exists for accurately predicting the required lower guidewall deflection angle (β) and high speed stream total pressure (p_r). The guidewall deflection was needed to compensate for the net displacement thickness of the shear layer and the guidewall boundary layers, and to maintain a zero streamwise pressure gradient thereby. The high speed total pressure, in turn, determined the high-speed stream static pressure at the splitter tip, given a specific area ratio of the nozzle. Although this static pressure was nominally one atmosphere, small differences were generally found from case to case. More importantly, it was found that a flow-dependent pressure difference across the splitter tip was required to produce a straight shear layer. This pressure difference resulted from the need to change the low-speed stream velocity vector at the splitter tip. Specifically, the splitter tip was designed with a 5° convergence angle of the two free

streams; therefore, when this angle did not equal the low-speed flow angle required for a negligible streamwise pressure gradient (*i.e.* the guidewall deflection angle), a static pressure difference was required to deflect the low-speed stream velocity vector. The magnitude of this pressure difference was found to vary from case to case; examples will be given in the following sections.

The lack of accurate predictions necessitated a trial-and-error procedure to find the desired values for β and p_r in each case. This iterative search was performed in the following manner. For each experiment, a "best guess" guidewall angle was chosen and held constant for the duration of the run. The high-speed stagnation pressure, however, was continuously varied as a function of time with the intention of sweeping across that value of pressure which resulted in a straight shear layer. This pressure sweeping is illustrated in Fig. 4.1, taken from Case 3. The left time trace shows the history of the high-speed stream total pressure. At the end of the start up ($t \sim 1.0\ s$), the total pressure was linearly increased for the remainder of the experiment. This pressure sweep was rather easily implemented by specifying a linearly increasing pressure in the feedback-control algorithm for the main pressure regulator (p_r in Eq. 3.6.1). The right time trace in Fig. 4.1 demonstrates the accuracy of the plenum pressure control for this flow. After startup, the difference between the measured total pressure (p_p) and the requested total pressure (p_r) fluctuated by only $\pm 0.5\%$ of p_r. This accuracy is typical for all of the supersonic nitrogen flows. The supersonic helium flows are generally less steady, with fluctuation levels of the order of $\pm 1.5\%$ (Fig. 4.2).

Although straight shear layers were the main focus of this study, the experimental procedure also generated data at off-design conditions. These off-design flows typically featured a strong wave coming off the splitter tip, created by the pressure imbalance between the two free streams at this point. This strong wave subsequently reflected many times off the upper guidewall and the shear layer, creating deflections at each shear layer reflection point. These often highly distorted flows were of interest from the point of view of how the shear layer structure and growth rate were affected by such large disturbances. Examples of these flows will be presented in the following sections describing individual test cases.

The next section will describe the results for Case 3, the all-nitrogen flow. In many respects, this medium compressibility flow served as a reference condition against which all other cases were compared. Following that, the high compressibility runs (Cases 1 and 2) will be discussed. These experiments were intended to reveal the presence of travelling shock waves in the flow. Finally, the low compress-

ibility results (Cases 4-11) will be presented. These include the subsonic/subsonic experiments intended to provide reference conditions for the incompressible growth rate.

4.2 The Medium Compressibility Nitrogen/Nitrogen Reference Flow

Fig. 4.3 is a side-view Schlieren photograph with horizontal knife edge of the basic $M_1 = 1.46\ N_2$, $M_2 = 0.28\ N_2$ reference flow. The figure is actually a composite photograph of two separate, but otherwise identical experiments, necessitated by the limited field of view of the optics system. The flow is from left to right, with the high-speed stream on top. The splitter plate would be just barely visible at the extreme left edge were it not obscured by the flow. The upper and lower guidewalls are clearly visible, with the lower guidewall deflected upwards ($\beta \simeq 2°$). The cross-stream instrument rake can be seen at the far right side, with the sixteen thermocouple support tubes in the foreground and the sixteen total pressure tubes hidden in the background. The three digit numbers in the pictures are identifying labels for the experiment in which the data were recorded. This basic arrangement will also be true for all of the flow photographs that will be presented later.

The most striking feature of Fig. 4.3 is the apparent absence of large-scale vortical structures. And yet, upon close inspection of the downstream region, one can identify some large, dark, arc-like features within the shear layer. It is possible that these features are coherent vortical structures, but they appear not as well defined as those found in incompressible flows. The wedge-like shape of the shear layer itself is, however, unmistakable. The edges are straight and the growth rate is linear. Clemens & Mungal (1990) report similar results at this convective Mach number, while Papamoschou & Roshko (1988) also found linear growth on the basis of velocity profile measurements, although their optical signal was too weak to show a well-defined wedge in the Schlieren photographs.

Also visible in the photograph are two standing wave systems in the supersonic high-speed free stream. One system originates from the nozzle block/guidewall junction, where spanwise curvature produces a non-uniform step on the order of $\pm 0.05\ mm$. The second system originates from the splitter tip. Both waves travel downstream and alternatively reflect off the upper guidewall and the shear layer. These negligibly weak waves have no apparent effect on the macroscopic properties of the shear layer; the layer remains straight and the growth rate is unaffected.

The measured visual growth rate listed in Table 4.1 was taken from this photograph. The value for M_1 was obtained from the wave angle of the weak wave coming from the nozzle/guidewall junction; *i.e.*,

$$M_1 = \frac{1}{\sin \mu_s} , \tag{4.2.1}$$

where μ_s is the wave angle measured with respect to the upper guidewall.* The value for M_2 was computed from the measured stagnation and static pressures made on the low-speed side; *i.e.*,

$$\frac{p_{t2}}{p_{s2}} = \left(1 + \frac{\gamma_2 - 1}{2} M_2^2\right)^{\gamma_2/(\gamma_2 - 1)} . \tag{4.2.2}$$

Once M_1, M_2, p_s and δ_{vis} were obtained, all of the other parameters listed in Table 4.1 could be computed and tabulated. A value of $C_\delta = 0.17$ was adopted for Eq. 2.2.3, as was done in Papamoschou & Roshko (1988). Note that the normalized growth rate of 0.570 for this flow agrees well with the available data (Fig. 4.4) and confirms that this flow was moderately compressible.

One possibility for the apparent lack of structure in Fig. 4.3 is that the sensitive Schlieren optical system was saturated by the signal from high-gradient, small-scale turbulence present in the flow. In other words, any underlying two-dimensional structure could be obscured by the small-scale turbulence superimposed on top of it. To investigate this possibility, the optical system was desensitized in order to reduce the signal from the small scale turbulence. Two different techniques were tried for this purpose. First, the knife edge was removed and the camera slightly defocused to produce a shadowgraph image (Fig. 4.5a). Second, the knife edge was rotated to a vertical position in the usual Schlieren arrangement to neglect the strong cross-stream optical signal (Fig. 4.5b). However, neither photograph indicates any underlying, two-dimensional, large-scale structure. These null results would seem to indicate that large scale structure, if it is present at all, must be substantially distorted by three-dimensionality in the flow. Nevertheless, the possibility that strong gradients generated by small-scale turbulence are the culprit cannot be completely ruled out on the basis of only these two photographs. Conclusive resolution of this issue requires some kind of planar diagnostic (*e.g.*, Rayleigh scattering) that would "slice" the flow instead of integrating across the span. Such an experiment is an obvious candidate for future work in the facility.

---

* This ignores the small effect of the boundary layer displacement thickness on the free stream velocity vector.

The streamwise pressure gradients, as measured along the two guidewalls, are plotted in Fig. 4.6. The variation along the high-speed guidewall was due to the standing wave systems discussed previously. These variations are obviously much larger than those on the low-speed guidewall; however, they constitute only $\pm 2\%$ of the high-speed stream total pressure. Note that these pressure variations were measured at the guidewall and not at the shear layer itself; in fact, the lack of curvature in the Schlieren photograph (Fig. 4.3) suggests that the pressure difference across the shear layer was not as large as the guidewall profiles might indicate. The low-speed stream pressure gradient was found to increase slightly just downstream of the splitter tip ($+17\%$ of the low speed stream total pressure, p_{t2}) and then to decrease slightly near the end of the test section (-19% of p_{t2}). This variation is only a $\pm 1\%$ of the *static* pressure, p_2.

As was discussed in the overview section of this chapter, this straight shear layer flow required a pressure difference across the splitter tip. From Fig. 4.6, this pressure difference ($\Delta p = p_1 - p_2$) was found to be $\sim 3\ kPa$. Note also that the mean static pressure p_2 was slightly *below* one atmosphere, despite a downstream boundary condition of exactly one atmosphere (*i.e.*, the catch bag). It proved to be impossible to specify the value of p_2, given the other constraints of zero (or minimal) streamwise pressure gradient and a straight shear layer. Nevertheless, it was found that p_2 was always very close to atmospheric pressure; hence, its small deviations were only a factor in the iterative search procedure for finding the required splitter tip pressure difference.

The total pressure profile for this flow is presented in Fig. 4.7. The coordinate system is defined such that the splitter tip corresponds to $(x, y) = (0, 0)$. The raw pressure measurements were converted to true total pressures using the Rayleigh pitot tube formula; *i.e.*,

$$\frac{p_s}{p_m} = \left[\frac{2\gamma M^2}{\gamma+1} - \frac{\gamma-1}{\gamma+1}\right]^{1/(\gamma-1)} \left[\frac{\gamma+1}{2} M^2\right]^{-\gamma/(\gamma-1)}, \tag{4.2.3}$$

where p_m and p_s are the measured total and static pressures, and M is the free stream Mach number. This equation must be iteratively solved for M, after which the true total pressure p_t can be computed from Eq. 4.2.2 with the subscript 2 replaced by a subscript 1. The least-squares fitted line in Fig. 4.7 is of the form

$$p_t(y) = a_1 + a_2 \tanh\left(a_3 + a_4 y + a_5 y^3\right), \tag{4.2.4}$$

where the a_i are the fit coefficients. The shear layer pitot-pressure thickness δ_{pit} is defined to be the distance between the locations on the best-fit line where the

velocity attains 99% of its free stream value. For this flow, it was found that $\delta_{\text{pit}} = 35\ mm$ as opposed to a visual thickness of $\delta_{\text{vis}} = 44\ mm$ as measured from Fig. 4.3 near the instrument rake. This suggests that the velocity profile is thinner than the density profile across the shear layer, a result also found by Brown & Roshko (1974) for incompressible flows.

To conclude this section, two off-design flows will be discussed for this test case. The first is shown in Fig. 4.8, which is a slightly overexpanded supersonic flow condition. Immediately obvious are the large vortical structures visible in the downstream section. The *only* difference between this flow and the regular flow shown in Fig. 4.3 is the strength of the shock wave coming off the splitter tip. Therefore, one is tempted to conclude that this strong planar wave system resonated with and thereby enhanced the weak, two-dimensional structure arguably present in the regular flow. Although it is difficult to see in the picture of Fig. 4.8, there is some evidence that the reflected wave spacing is equal to the vortex spacing, a feature that lends credence to the idea of resonant forcing of the shear layer (Zhuang *et al.* 1990). Finally, it must be noted that relatively few of the off-design flows for which data exist demonstrated such enhanced structure, attesting perhaps to the difficulty in *unintentionally* achieving the required resonance conditions.

The second off-design flow is shown in Fig. 4.9. This badly pressure mismatched flow illustrates the relative insensitivity of the overall growth rate to the impact of strong waves of this orientation. The shear layer is highly curved by these waves, and yet the shear layer thickness in the vicinity of the instrument rake is $\delta_{\text{vis}} = 40\ mm$, which is very close to the nominal shear layer thickness of $\delta_{\text{vis}} = 44\ mm$. This result implies a considerable resiliency of the mixing layer to such external disturbances. This resiliency is somewhat surprising, given the experimental evidence quoted earlier (Section 2.2), which suggested that the shear layer growth rate is *quite* sensitive to changes in the *initial conditions*. Taken together, these observations indicate that the shear layer growth rate is almost completely determined by the conditions at the splitter tip, and that it retains the memory of these formative conditions for very great distances. Note that for this Case 3 flow, the shear layer to splitter tip momentum boundary layer thickness ratio is roughly $\delta/\Theta \simeq 2000$, which is certainly a long distance over which to remember the initial conditions of the flow (Bradshaw 1966, Dimotakis & Brown 1976, Dimotakis 1989).

4.3 The High Compressibility Flows

Two high compressibility flows were studied in this research effort, both of which used helium as the high-speed fluid. The difference between the two flows was that Case 1 used argon as the low-speed fluid, whereas Case 2 used nitrogen. The high sound speed of helium produced a very large velocity difference across the shear layer in these cases, resulting in a predicted isentropic convective Mach number, $M_{c1}^{(i)}$, close to unity (see Table 4.1). However, given the highly asymmetric results of Papamoschou (1989), this isentropic model prediction was not expected to be accurate. Instead, flows with one of M_{c1} and M_{c2} high supersonic and the other low subsonic were thought to be more likely. Furthermore, it seemed probable that such flows with supersonic convection velocities would produce travelling shock and expansion waves that ought to be detectable with the available optics (Papamoschou 1989, Dimotakis 1989). As it turned out, these expectations were realized.

Figures 4.10 and 4.11 are side view Schlieren photographs of these two test cases using a horizontal knife edge. Immediately obvious in both figures is a complex, yet regular wave system in the low-speed flow. Note that these waves could not have been *standing* waves produced by guidewall surface roughness or some other such mechanism, because the free stream Mach number (M_2) was much less than unity. The only possible source for these waves was shear layer structures travelling at a *supersonic* velocity with respect to the low-speed flow. Note that the absence of a wave system on the high-speed side means that these shear layer structures are travelling *subsonically* with respect to the high-speed flow.

Closer inspection of the wave system reveals several key features. The system is comprised of a set of incident waves originating at the shear layer and a set of reflected waves off the lower guidewall. Each set is composed of alternating compression and expansion waves, which must nearly balance each other to maintain a negligible mean streamwise pressure gradient. Not surprisingly, the compression (shock) waves are sharper and more easily seen in the photographs; witness the white incident waves and the black reflected waves that dominate the images. The wave system does not extend all the way upstream, but instead seems to originate from an imaginary line that runs from the splitter tip to the guidewall at roughly a 45° angle. A similar generating envelope was observed in the various supersonic jet experiments of Lowson & Ollerhead (1968), Tam (1971) and Oertel (1979).

It is not possible to discern from these photographs the precise nature of the shear layer structures that created the waves. In fact, the shear layer seems devoid

of *any* kind of two-dimensional structure at all. There is not even the hint of two-dimensional vortex structure seen in the moderate compressibility flow (Fig. 4.3). Within the wave system itself, one can see a large number of thin, sharp white lines (compression waves) which seem to constitute larger, more diffuse features. These larger features have a spacing which approaches the local shear layer thickness δ_{vis}. The presence of the closely spaced, sharp lines provides further support for the idea that the large-scale structure is either concealed by the abundant small scale turbulence or distorted by three-dimensionality.

The travelling wave system also represents a powerful diagnostic for the convection velocity of the shear layer structures, regardless of their exact nature. Specifically, the angles of these waves can be measured to provide an estimate for the convective Mach number, M_{c2}; *i.e.*,

$$M_{c2} \simeq \frac{1}{\sin \mu_{\text{T}}} , \tag{4.3.1}$$

where μ_T is the wave angle of the travelling wave. This angle must be measured with respect to the velocity vector of the structure creating the wave. For the current analysis, this velocity vector was assumed to bisect the shear layer wedge, giving an approximate angle of $-2°$ with respect to the x-axis. Note that this Mach number estimate will be *exact* in the limit of negligible wave strength, and will underestimate M_{c2} if the travelling waves are strong. Measurement of the wave angles in Figures 4.10 and 4.11 was hindered somewhat by the complex merging and interference patterns of the visible waves. In practice, a range of wave angles was found by measuring many waves in the photographs. After application of Eq. 4.3.1, this yielded:

$$2.1 \leq M_{c2} \leq 2.6 \qquad \text{for Case 1} \tag{4.3.2a}$$

and

$$2.0 \leq M_{c2} \leq 2.4 \qquad \text{for Case 2.} \tag{4.3.2b}$$

A second diagnostic was employed in these experiments in order to measure the convection velocity of the shear layer structures. This diagnostic was the PCB piezoelectric pressure transducers that were discussed in Section 3.4. These flush-mounted guidewall transducers had sufficient temporal resolution ($\sim 1\ \mu s$) to measure the pressure "footprint" of the travelling waves on the guidewall. An example of these pressure time traces for Case 2 is presented as Figure 4.12. The pressure fluctuation is seen to be quite large, on the order of $\pm 20\ kPa$. Recall that the static pressure was only 100 kPa (1 atm). The two transducers whose time traces are

shown in Figure 4.12 were located on the centerline of the guidewall and spaced 5.08 cm (2.0 in) apart. The cross-correlation between these two time traces is shown in Figure 4.13. The dominant peak is centered on a time lag of 59 μs. Given the 5.08 cm spacing and a time lag of 59 μs, one can infer a convection velocity of the pressure footprint of**

$$u_c = \frac{0.0508}{59 \times 10^{-6}} = 860\ m/s. \tag{4.3.3a}$$

Given the free stream conditions of $u_2 = 104\ m/s$ and $a_2 = 347\ m/s$, this yields

$$M_{c2} = \frac{u_c - u_2}{a_2} = 2.18\ . \tag{4.3.3b}$$

This value falls within the range suggested by the wave angle measurements.

It should be noted that the cross-correlation function presented in Fig. 4.13 has the highest peak of any of the measurements taken for these cases. Nevertheless, even though the amplitude of the peak varied from measurement to measurement, its temporal location (*i.e.* the time lag) never changed by more than ±5%. Furthermore, the 5 cm spacing between transducers must be considered as large, particularly in light of the photographic evidence which shows considerable wave interaction on scales much smaller than 5 cm. Closer spacing would presumably increase the cross-correlation peak and reduce its time lag, but it should leave the inferred convection velocity unchanged. Finally, it was generally found that cross-correlations computed from transducer pairs downstream near the instrument rake possessed higher peak amplitudes than those computed from transducer pairs near the splitter tip. This improved cross-correlation is to be expected, perhaps, because of the fact that the local shear layer thickness approaches the transducer separation at the downstream location.

If we adopt a value of $M_{c2} = 2.18$ for Case 2, this requires that $M_{c1} = 0.36$ (from Eq. 2.2.8 and 2.2.9). Here then is corroboration of the Papamoschou (1989) results, which indicated very different convective Mach numbers for high compressibility flows. The current data are plotted with the Papamoschou data in Figure 4.14. Note that the result for Case 1 is also included with $M_{c1} = 0.31$ and $M_{c2} = 2.54$ as deduced from its own cross-correlation measurements. Although the scatter in the data is large, it can at least be said that the new data do not contradict the old.

** This calculation neglects the non-parallelism of the convection velocity vector and the lower guidewall. The error is less than 1% because of the small angles involved.

Although the presence of the travelling wave system is presumably related to the unequal convective Mach numbers, the precise mechanism involved remains uncertain. If the total pressure matching concept described in Section 2.2 applies to this situation, then there *must* be some physical process that dissipates large amounts of total pressure on the low-speed side of the shear layer in these two flow cases. Shock waves can certainly play this total-pressure dissipation role (Papamoschou 1989 and Dimotakis 1989); however, the waves visible in the photographs are not strong enough to produce the observed inequalities. This conclusion is based on three observations: First, the waves in the photographs deflect by only small amounts when intersected by other waves of the system; second, the cross-correlation measurements for M_{c2} agree with the wave angle measurements; and third, even a *normal shock wave* with a shock Mach number of $M_s = M_{c2} = 2.18$ dissipates only 33% of the upstream total pressure. This cannot nearly account for the convective frame total pressure difference that exists in these two flow cases.

A possible resolution of this dilemma can be found in the idea that shear layer vortices may be capable of *locally accelerating* the flow to Mach numbers much higher than M_{c2} (Papamoschou 1989). Fig. 4.15 illustrates the basic idea, in which an expansion fan accelerates the flow around the vortex and a shock wave decelerates the flow near the stagnation point between vortices. It is plausible that this re-compression shock will be essentially *normal* near the vortex but will transition to a much weaker oblique shock in the free stream flow due to interaction with the expansion waves coming off the edge of the vortex in the accelerated flow region. This strong re-compression shock, with $M_s > M_{c2}$, therefore provides a mechanism in which very large amounts of total pressure can be dissipated.

Unfortunately, the current experiments were unable to photographically detect any strong waves embedded in the shear layer. In addition to the photographs of Figs. 4.10 and 4.11, a Schlieren picture was also taken with a vertical knife edge (Fig. 4.16) and shadowgraph picture was taken in a manner described in the previous section for Case 2 flow (Fig. 4.17). Both of the latter pictures reveal more internal structure than the horizontal knife edge Schlieren photograph, but there is no sign of any embedded shock waves. Of course, it is possible that the same elements which may prevent the recognition of large-scale vortex structure (three-dimensionality, abundant small-scale turbulence) also hide embedded shock waves. Nevertheless, given the very large dissipation required to explain the measured convection velocity, it is surprising that these supposedly strong shocks (*i.e.* $M_s = 6.8$ for Case 1) do not show up in the available photographs.

Figure 4.16 reveals another noteworthy feature, namely the existence of vertical travelling waves in the low-speed flow. These white lines are *normal* shock waves travelling *upstream*. They are evidently weak waves since they do not seem to affect the shear layer or the other travelling waves to an appreciable extent. Their origin is unknown. Note that these normal shock waves possess an irregular spacing and are therefore unlikely to be a resonance phenomenon related to structural vibrations.

The streamwise static pressure profiles for the two test cases are presented as Figs. 4.18 and 4.19. Both plots show a much larger pressure difference across the splitter tip than is found for Case 3; specifically, $\Delta p = 12\ kPa$ for Case 1 and $\Delta p = 14\ kPa$ for Case 2, versus $\Delta p = 3\ kPa$ for Case 3. Like that of Case 3, the low-speed static pressure in the two flows is seen first to increase and then to decrease along the lower guidewall. The net overall pressure difference is -5% for Case 1 and -12% for Case 2.

The total pressure profile for Case 1 is presented as Fig. 4.20. The corresponding curve for Case 2 is omitted here because $\gamma_{He} \neq \gamma_{N_2}$, thereby complicating the use of the Rayleigh pitot-tube formula (Eq. 4.2.3).† For Case 1, the shear layer thickness based on the total pressure profile in Fig. 4.20 is found to be $\delta_{\text{pit}} = 37\ mm$. This can be contrasted to a visual thickness of $\delta_{\text{vis}} = 40\ mm$. As for Case 3, the velocity profile is seen to be narrower than the density profile.

The entries in Table 4.1 for these two test cases were determined in the same manner that was already described for Case 3 in the previous section. The resultant normalized growth rates ($\delta_{\text{vis}}/\delta_{\text{inc}}$) are plotted in Fig. 4.21, along with the other available data. The agreement is seen to be fairly good. Actually, it is somewhat surprising that the data collapse as well as they do given the fact that the isentropic model for predicting M_{c1} is demonstrably wrong. Perhaps this can be understood by considering $M_{c1}^{(i)}$ to be an *averaged* measure of compressibility in the flow, a parameter that combines the effects of a supersonic M_{c2} and a subsonic M_{c1}, in this example. The value of $M_{c1}^{(i)}$ also happens to be close to the parameter $\Delta U/(a_1 + a_2)$ suggested by Papamoschou (1989) as a means of determining when travelling waves would be present in a flow. From this point of view, $M_{c1}^{(i)}$ is possibly still a valid measure of the overall compressibility of the shear layer, although the underlying physical ideas are somewhat different than originally thought.

An alternative way to scale the compressibility effect in turbulent shear layers

---

† *i.e.*, a $\gamma(y)$ profile would have to be assumed.

is to take the *maximum* of the two convective Mach numbers for a flow. The result of such scaling is shown in Fig. 4.22, where only the available data with *measured* convective Mach numbers are included. The general behaviour of the data is similar to that of the previous scaling, although clearly more data are required to evaluate the relative merits of the different scaling ideas.

Although a large amount of off-design flow data was accumulated for these two test cases, there was no indication of large-scale structures in any of them. This is in contrast to the results for the medium compressibility off-design flows in which two-dimensional structure sometimes could be seen, presumably enhanced by the impact of strong planar waves off the splitter tip. This suggests that compressibility suppresses the formation of two-dimensional structure, even to the extent that some external forcing is unable to compensate for this suppression. This lack of large-scale two-dimensional structure in high compressibility mixing layer flow is in accord with the observations of Clemens & Mungal (1990) and Goebel & Dutton (1990). The final remark to be made about the off-design conditions for these cases is that the overall growth rates demonstrated little sensitivity to the impact of strong waves. This behaviour was very similar to that of Case 3, with variations in the growth rate on the order of 10% and less.

4.4 The Low Compressibility Flows

The low compressibility experiments were motivated by the need to anchor the normalized growth rate as $M_{c1}^{(i)} \rightarrow 0$. Given the modelling uncertainty discussed in Section 2.2, this was deemed a necessary precaution in order to better deduce the growth rate reduction that was due to compressibility effects alone. As it turned out, however, surprising results were found in which the flow demonstrated complex behaviour as $M_{c1}^{(i)} \rightarrow 0$. This behaviour hinted at the possibility that there could be a compressibility effect due to a *supersonic* M_1 even in the limit of $M_{c1}^{(i)} \rightarrow 0$. This, in turn, led to two experiments with $M_1 < 1$ in order to contrast the differences between supersonic and subsonic high-speed flow at very low $M_{c1}^{(i)}$.

Some of this complex behaviour is illustrated in Fig. 4.23, which is a plot of the normalized growth rate for the supersonic M_1 flows (Cases 1 to 9), along with the other available data. Not only do the new data fail to recover the predicted incompressible growth rate as $M_{c1}^{(i)} \rightarrow 0$, they also show a peak at $M_{c1}^{(i)} \simeq 0.3$, below which the normalized growth rate actually *decreases*. This behaviour was

completely unexpected and is not understood at the present time. Nevertheless, there are a few clues to this behaviour that can be gleaned from the available data.

The first clue is that *all* of the unexpectedly low growth rates (Cases 7, 8 and 9) occurred at very low density ratios, lower in fact than any of the other flows represented in Fig. 4.23. As can be seen from Table 4.1, the current low compressibility experiments were performed using various mixtures of helium and argon as the low-speed fluid. Low values of $M_{c1}^{(i)}$ were achieved by using high concentrations of helium (*i.e.*, large a_2) which, as a byproduct, also resulted in low density ratios. The reason why such low density ratios should be accompanied by low growth rates is not at all clear. Certainly, there were no indications from earlier incompressible experiments of unusually low growth rates at density ratios as small as 1/7 (Brown & Roshko 1974, Frieler & Dimotakis 1988). One major difference between those incompressible experiments and the current research is the existence of supersonic versus subsonic flow on the high-speed side. It became necessary, therefore, to investigate this difference by conducting subsonic M_1 experiments in the same facility that was used for the current supersonic experiments.

Not too surprisingly, these subsonic experiments (Cases 10 and 11) *do* very nearly recover the predicted incompressible growth rate. Fig. 4.24 shows the usual plot with these two subsonic results included. Here then is clear evidence that the growth rate can be strongly influenced by whether or not M_1 is subsonic or supersonic. Note that the other dimensionless parameters of the contrasted flows are approximately equal: $M_{c1}^{(i)}$, Re_x, r and s. Therefore, one is led to the conclusion that $M_{c1}^{(i)}$ scaling does *not* represent all of the compressibility effects in a turbulent shear layer, because reduced growth rates are found that are due to a supersonic M_1 even in the limit of $M_{c1}^{(i)} \to 0$.

However, even if $M_{c1}^{(i)}$ scaling is not universal, it works quite well for *most* of the available data in Fig. 4.24. In fact, it is remarkable to note that for $M_{c1}^{(i)} \leq 1$, the bulk of the data is well represented by a *single straight line* (Fig. 4.25). Interestingly enough, this fitted line very nearly passes through $(M_{c1}^{(i)}, \delta_{\text{meas}}/\delta_{\text{inc}}) = (0, 1)$, a requirement that the data must satisfy by definition. Taken together, these observations indicate that $M_{c1}^{(i)}$ compressibility scaling must have some validity. Its failure to account for the growth rates of Cases 7, 8 and 9 should therefore be viewed as a sign of incompleteness rather than error.

Further clues to the unexpected behaviour of Cases 7, 8 and 9 can be found in the Schlieren photographs of these flows (Figs. 4.27 to 4.29). When viewed

with Case 6 (Fig. 4.26) as a sequence of flows with decreasing density ratio, the photographs of Cases 7 and 8 appear to indicate some kind of transitional behaviour. Specifically, these two shear layers develop a pronounced undulation downstream of a certain point in the flow. This undulation, in turn, evolves into large, seemingly two-dimensional structures near the instrument rake. It should be emphasized that the photographs of Figs. 4.27 to 4.29 are typical; it was not possible to remove the undulation from these shear layers by a suitable choice of high-speed stream total pressure or lower guidewall deflection angle. Interestingly enough, this undulation is absent in the lowest density ratio flow (Case 9), suggesting that this flow lies *beyond* the transitional regime.

Very little is known about this transition phenomenon except that it coincides with the reduction in observed growth rates over a density ratio range of $0.1 < s < 0.2$. One can speculate that this behaviour is the result of competing growth rate mechanisms which become equally significant somewhere in the middle of that density ratio range. Note that this new growth rate mechanism does not appear to be related to the so-called "wake effect" identified by Koochesfahani & Frieler (1987). They found that at *high* density ratios ($s \geq 6$) a second instability mechanism becomes important in addition to the usual Kelvin-Helmholtz instability. This second mechanism was linked to the velocity deficit in the wake of the splitter plate in the initial roll-up region of the shear layer.

Whatever form the new low density ratio growth rate mechanism takes, it seems plausible that it is directly related to the existence of *supersonic* flow on the high-speed side of the shear layer. It must be emphasized that only the combination of $M_1 > 1$ and $0.1 < s < 0.2$ produces the unusual behaviour, at least based on the available data. One might reasonably suspect that the hyperbolic character of the $M_1 > 1$ free stream flow lies at the heart of the matter; certainly, this will inhibit downstream-to-upstream feedback mechanisms in the flow (Dimotakis & Brown 1976). Of course, such inhibition is present whether the flow possesses a low density ratio or not. Therefore, this phenomenon must contain one or more additional elements that, for the present time, remain unknown.

In contrast to the surprises of Cases 7, 8 and 9, the Schlieren photograph of the almost equal density *subsonic* flow (Case 10, Fig. 4.30) is very much as expected. The large, two-dimensional vortex structure is quite well defined and the growth rate, as previously mentioned, is very close to the predicted value.

To close out this section, a few summarizing comments will be made concerning

some of the implications of these low compressibility results. The first comments concern the large-scale structure content of these flows. Although the altered character of Cases 7, 8 and 9 complicates any general conclusions, there is evidently less two-dimensional vortex structure in the supersonic M_1 experiments versus the subsonic M_1 experiments. In particular, the very low compressibility flow of Case 9 (Fig. 4.29) shows no discernible two-dimensional structure, even though its has a *lower* $M_{c1}^{(i)}$ than does the subsonic flow of Case 10. This would seem to contradict the conclusions of Clemens & Mungal (1990) who stated that large-scale two-dimensional structure was present at low $M_{c1}^{(i)}$ but not at high $M_{c1}^{(i)}$.‡ For example, the photograph of Case 6 (Fig. 4.26) reveals little structure, even though it has approximately the same $M_{c1}^{(i)}$ as the Clemens & Mungal (1990) flow, and it is not in the transitional regime. Given the current results, therefore, the determining factor that decides the large-scale structure content of the flow seems to be whether or not one of the free stream Mach numbers is supersonic. All of the supersonic M_1 flows have much reduced, or at least not obvious, structure; both of the subsonic M_1 flows have a clear, well-defined structure.

The second set of implications to be discussed concerns the growth rate data at low $M_{c1}^{(i)}$. The fitted line to the bulk of the data in Fig. 4.25 suggests that the growth rate is affected by compressibility even at very low $M_{c1}^{(i)}$. Unlike the Papamoschou & Roshko (1988) data, there is no indication that the growth rate plateaus at a constant value of $\delta_{\text{meas}}/\delta_{\text{inc}}$ at low $M_{c1}^{(i)}$. The idea that there could be compressibility effects at very low $M_{c1}^{(i)}$ appears absurd at first glance; however, the flow may be capable of generating *local* Mach numbers far in excess of $M_{c1}^{(i)}$ due to acceleration around shear layer vortices (Section 4.3). Furthermore, there is direct evidence that a supersonic M_1 can decrease growth rates even when $M_{c1}^{(i)}$ is quite low. Nevertheless, a counter-argument can certainly be made that changing initial conditions (*i.e.*, splitter plate boundary layers) could be responsible for the non-constant $\delta_{\text{vis}}/\delta_{\text{inc}}$ at very low $M_{c1}^{(i)}$. Unfortunately, a thorough study of the splitter-plate boundary layers was beyond the scope of the current investigation, leaving the issue unresolved.

---

‡ In a private communication, Clemens & Mungal have indicated that their Schlieren observations of two-dimensional structure in the low compressibility flow were very sensitive to knife edge location. It is possible that differences in the knife edge position can account for the non-detection of two-dimensional structure in the current experiments as compared to the Clemens & Mungal experiment.

CHAPTER 5

Results For Reacting Flows

5.1 Overview

This chapter will present and discuss results for the reacting experiments that were performed in this study. A complete list of these experiments can be found in Table 5.1. These experiments are divided into two groups: medium compressibility flows based on N_2/N_2 diluents (Cases 3a to 3e); and high compressibility flows based on He/N_2 diluents (Cases 2a to 2c) or He/Ar diluents (Cases 1a and 1b). The methodology employed was first to conduct a kinetics study at $\phi = 1$ in order to establish the fast-chemistry regime for a given flow. The second step was then to perform a flip experiment in this regime in order to estimate the entrainment ratio, E_n, and the fraction of mixed fluid in the layer, δ_m/δ. In all cases, the NO concentration was kept constant at a low value of 0.25%. It can be seen in Table 5.1 that the high compressibility flip experiment was performed with He/Ar diluents, whereas the kinetics experiment was based on He/N_2 diluents. This is the result of a late recognition of the fact that the flip experiment requires constant molar heat capacity across the layer, or exact knowledge of $C_p(\xi, y)$, in order to yield valid estimates of E_n and δ_m/δ. Constant molar heat capacity, in turn, requires $\gamma_1 = \gamma_2$ since, for a perfect gas,

$$C_{p_i} = \frac{\gamma_i R_\circ}{\gamma_i - 1} , \tag{5.1.1}$$

where $R_\circ$ is the universal gas constant. This motivated the use of He/Ar diluents for the flip experiment. It should be noted, however, that the fast-chemistry regime for He/N_2 flow should be very close to that of He/Ar flow. Specifically, He/Ar flow has a slightly higher u_c (therefore lower test section residence time, τ_x), but $C_p\,(Ar) \simeq 0.7\, C_p\,(N_2)$, resulting in higher temperatures and faster chemistry.

Ideally, one would like to perform the flip experiment in the limit of negligible heat release. In this limit, the estimates for E_n and δ_m/δ also apply to the corresponding non-reacting flow. However, it will be shown that the attainment of fast chemistry in these ambient total temperature flows requires fairly large heat release (see Table 5.1). This heat release must be expected to have *some* effect on the flow itself, thereby contaminating the estimates for E_n and δ_m/δ. An assessment of the errors involved will be included in the discussion of the results in the following sections.

The exposed-junction thermocouple probes used in these experiments (Fig. A5) suffer from two limitations that must be considered in the analysis. First, there is significant heat conduction to the support prongs because the length-to-diameter ratio of the sensing wire is only about 100. As a result, it is found that the probes in the high-speed stream do not reach a steady-state temperature until the $t \sim 1.5$ *sec* mark. Therefore, all temperatures reported here were obtained after this time. The second limitation of the probes is that stagnation conditions are achieved only at the leading edge of the wire, resulting in a measurement of somewhat less than the true total temperature. This difference between the measured temperature, T_{meas}, and the true total temperature, T_t, is usually quantified in terms of the recovery factor, $\mathcal{R}$, defined here as

$$\mathcal{R} = \frac{T_{\text{meas}} - T_s}{T_t - T_s} \ , \tag{5.1.2}$$

where T_s is the true static temperature. For a given geometry, $\mathcal{R}$ is generally a complex function of the local heat transfer characteristics between the wire on the flow; fortunately, this function does not have to be known in order to measure the temperature change that is due to heat release in these compressible shear layer experiments. Specifically, it can be shown that the true *static* temperature difference between two flows is equal to the *measured* temperature difference, if $\mathcal{R}$ is equal in both flows and C_p is not a function of position. In other words, as long as the reacting temperature measurements for each probe are referenced to the corresponding non-reacting temperature measurement for that probe, the effect of a non-unity recovery factor can be factored out of the problem. This technique will be illustrated in the following sections discussing specific flows.

5.2 Results For Medium Compressibility Reacting Flows

The measured temperature profile for the Case 3 flow without chemical reactions is shown in Fig. 5.1. The profile shape is seen to be rather unusual, with the fitted line of the form

$$T_{\text{meas}}(y) = a_1 + a_2 \tanh(a_3 + a_4 y) + a_5 \tanh(a_6 + a_7 y) , \qquad (5.2.1)$$

where the a_i are the fitted constants. Note that these temperatures are all referenced to the ambient temperature in the lab; therefore, the value of $T_{\text{meas}} \sim 0$ in the low-speed flow is to be expected. The value of $T_{\text{meas}} \sim -17\ K$ in the high-speed stream provides an estimate of the recovery factor for the thermocouple probes using Eq. 5.1.2; *i.e.*,

$$\mathcal{R} = \frac{(295 - 17) - 207}{295 - 207} = 0.81 . \qquad (5.2.2)$$

A composite Schlieren photograph of the Case 3c reacting flow is shown in Fig. 5.2. The presence of significant heat release in the shear layer can be inferred from the pronounced banded structure seen in the photograph. Specifically, black indicates a positive density gradient ($\partial\rho/\partial y$) and white indicates a negative gradient. Therefore, the density is seen to be lower in the shear layer than in either free stream, with the black/white interface indicating the point of lowest density and highest temperature. It is interesting to note that this photograph does not indicate any vortical structures inside the shear layer. This lack of hot vortex cores provides further evidence that the underlying large-scale structure, if it exists at all, is highly distorted by three-dimensionality.

The results of the kinetics study (Cases 3a, 3b and 3c) are presented in Fig. 5.3. The temperature rise that is due to heat release, ΔT_j, of probe j at location y_j is computed from

$$\Delta T_j = T_{rj} - T_{nj}(y_j) , \qquad (5.2.3)$$

where T_{rj} is the measured reacting temperature for probe j, and $T_{nj}(y_j)$ is the non-reacting temperature profile shown in Fig. 5.1. The normalization by ΔT_{flm} (listed in Table 5.1) removes the effect of different molar concentrations on the overall heat release, and allows for direct comparison of the relative kinetic rates. The solid lines shown in Fig. 5.3 are best-fit lines of the form

$$\frac{\Delta T}{\Delta T_{\text{flm}}} = \exp(a_1 + a_2 y + a_3 y^2 + a_4 y^3 + a_5 y^4) , \qquad (5.2.4)$$

where the a_i are the fitted coefficients. This function is identical to the one used in Mungal & Dimotakis (1984). The temperature thickness, δ_1, of the shear layer is computed from this fitted profile with the edges defined by a normalized temperature rise of 1% of the maximum value. The integral of this fitted line yields the product thickness, δ_P as defined in Eq. 2.3.10.

The close agreement between the 2% and 4% reactant concentration profiles in Fig. 5.3 is a strong indication that the fast-chemistry limit has been attained in both flows. This can be contrasted with the 1% reactant concentration profile which shows much less chemical product formation, presumably because of incomplete (slow) chemical reactions. Remarkably enough, the Damköhler number for the 2% experiment is only 1.4, considerably below the limiting value of 5.3 suggested by Mungal & Frieler (1988). In addition to the inherent uncertainties with the model employed in this analysis, there are two other possible explanations for this difference. The first is that the Mungal & Frieler (1988) limiting value may be too conservative; as can be seen from their data, the product thickness at roughly half the limiting Damköhler number ($[NO]/[NO]_* = 1/4$ in their notation) is within 7% of their stated fast-chemistry value. In other words, the designation of the fast-chemistry limit is somewhat arbitrary, and a reasonable case can be made that the limiting Damköhler number in the Mungal & Frieler study is smaller than 5.3, perhaps as low as half that value.

The second explanation for the difference stems from the fact that the Mungal & Frieler (1988) experiments were conducted at $\phi = 1/8$ (hydrogen rich), whereas the current experiments were performed at $\phi = 1$. There are indications[♯] that the very high molecular diffusivity of hydrogen can have a significant impact on the chemistry, particularly when $\phi \neq 1$. Specifically, the hydrogen will diffuse into the fluorine stream faster than the nitric oxide will, thereby reducing the effective NO concentration, and hence the kinetic rate, in the flame sheet regions of the flow. Since this effect is completely neglected in the current flow/kinetics model, the computed characteristic chemical times for the $\phi = 1/8$ cases may be much too low as compared to the chemical times for the $\phi = 1$ cases. Whether or not this effect can completely account for the observed discrepancy must await a more comprehensive model capable of accounting for the effects of differential diffusion.

Another noteworthy result of this kinetics study is that the shear layer thickness derived from the fitted temperature profile, δ_1, is seen to increase with increasing

---

♯ Unpublished computations performed by Cliff Frieler.

heat release. Specifically, δ_1 increases by roughly 10% over the three experiments. This difference, though not large, is opposite to that found in Hermanson & Dimotakis (1989) for incompressible shear layers, as was discussed in Section 2.2. This suggests a compressibility effect in the present experiments which reverses the thinning behaviour seen in incompressible shear layers. Nevertheless, the effect of heat release on the flow remains weak and suggests that significant heat release will not significantly compromise the validity of the flip experiment.

Given the result that the 2% experiment (Case 3b) produced fast chemistry in the flow, the flip experiment was designed such that the *lean* reactant was also 2%. Ideally, one would like to set the rich reactant concentration arbitrarily high in order to drive $\xi_0 \rightarrow 0$ as was discussed in Section 2.3. However, there are practical constraints in the laboratory that limit the maximum acceptable fluorine concentration to roughly 10%.* Therefore, it was decided to set the rich reactant concentration to 8%, thereby producing a flip experiment with $\xi_0 = 0.2$ ($\phi = 1/4, 4$). The results of this flip experiment (Cases 3d and 3e) are plotted in Fig. 5.4, along with the $\phi = 1$ flow (Case 3b).

Several key features can be seen in Fig. 5.4. First, the temperature profile shifts *away* from the rich reactant in both cases. This behaviour has been seen before in the incompressible experiments (*e.g.* Mungal & Dimotakis, 1984) and stems from the fact that compared to the $\phi = 1$ case, the rich reactant will penetrate further into the other stream before being consumed. The second feature to be noted is that the normalized product thicknesses for the flip experiment are lower than for the $\phi = 1$ case. Since it is expected that the maximum product thickness will occur when $\xi_\phi \simeq \bar{\xi}$ (Section 2.3), this result suggests that $\bar{\xi}$ is closer to 0.5 than it is to 0.2 or 0.8. Finally, it is seen that the temperature thickness of the $\phi = 1/4$ experiment is considerably larger than the other profiles.

This last point is difficult to understand. It cannot be *solely* a heat-release effect because ΔT_{flm} is virtually the same for the $\phi = 1/4$ and $\phi = 4$ experiments. The presence of 8% H_2 *does* change the gas properties of the high-speed flow ($+3\%\, u_1$, $-7\%\, \rho_1$), but these changes are seemingly too small to account for the 30% change in growth rate. The possibility of differential hydrogen diffusion must be considered, and yet it is difficult to believe that a diffusion process can affect the overall growth rate of a turbulent shear layer. A more plausible hypothesis is that there is a coupling between compressibility effects and the *distribution* of heat release within

---

* These constraints are largely dictated by safety considerations in the present configuration.

the layer, which changes the growth rate. More specifically, the fact that most of the heat release occurs near the low-speed free stream perhaps negates some of the layer thinning that is due to overall compressibility effects. This speculation is very tentative, of course, and requires further investigation to be properly assessed. This issue will be reconsidered in the next section when the $\phi = 1/3$ high compressibility flow (Case 1a) is discussed.

The different growth rate of the $\phi = 1/4$ flow calls into question the validity of the flip experiment under these conditions. It is perhaps reasonable to postulate that E_n and δ_m/δ would not be much affected by this change in growth rate; witness the facts that the temperature profile for $\phi = 1/4$ extends further in *both* free streams, and that the measured value of δ_P/δ for $\phi = 1/4$ is not obviously absurd. Nevertheless, the confidence in this flip experiment cannot be considered high and therefore the derived results need to be confirmed by other experiments before they can be considered reliable.

Given the δ_P/δ results for the flip experiment (see Table 5.1), the calculations for E_n and δ_m/δ are straightforward. From Eqs. 2.3.11, 2.3.12 and 2.3.5:

$$\frac{\delta_m}{\delta} \simeq (1 - 0.2)(0.259 + 0.243) = 0.40 \,, \tag{5.2.5a}$$

$$\bar{\xi} \simeq \frac{0.259}{0.243 + 0.259} = 0.52 \tag{5.2.5b}$$

and

$$E_n \simeq \frac{0.516}{1 - 0.516} = 1.07 \,. \tag{5.2.5c}$$

These values can be compared to $\delta_m \simeq 0.49$ (Dimotakis 1989) for incompressible shear layers and $E_n \simeq 1.44$, a theoretical value computed from Eqs. 2.3.6, 2.3.7 and 2.2.12. It is interesting to note that the current value of $\delta_m/\delta \simeq 0.40$ may *not* be entirely the result of a compressibility effect. The two experiments employed different flip ratios, namely $\phi = 1/4, 4$ for the current compressible experiment versus $\phi = 1/8, 8$ for the earlier incompressible experiment. This change alone will reduce δ_m/δ by roughly 0.04, a value estimated from the incompressible data of Mungal & Dimotakis (1984). Furthermore, the incompressible experiments of Mungal *et al.* (1985) and Hermanson & Dimotakis (1989) indicated a weak Reynolds number dependence for δ_P/δ; namely, δ_P/δ decreasing by roughly 20% per factor of ten increase in Re_δ. Since $Re_\delta \sim 10^6$ for the current experiments versus $Re_\delta \sim 10^5$ for that earlier work, one might expect a 20% decrease in δ_P/δ (hence δ_m/δ), which is

almost exactly what is found. It must be noted, however, that the extrapolation of the incompressible Re_δ data by a factor of ten to match the current experiments is highly speculative.

The compressibility effect on E_n is seen to be rather large, changing the mixture from high-speed fluid-rich to an almost equal composition. If Eqs. 2.3.6 and 2.3.7 are assumed to be applicable to compressible flows, this allows an inference to be drawn concerning the structure convection velocity (u_c) in this flow. Specifically, a value of $u_c \simeq 370\ m/s$ is required in order for this theoretical analysis to yield $E_n \simeq 1.07$. This value is 92 m/s (+33%) higher than that predicted by the usual model, Eq. 2.2.12. Unfortunately, it was not possible to measure u_c directly for this flow with the available instrumentation. Nevertheless, a plausibility argument exists that supports this higher value for u_c. For the high compressibility flows (Cases 1 and 2) it is seen that the measured convection velocities are much higher than Eq. 2.2.12 suggests. To the extent that this behaviour accompanies compressibility effects in the flow, one can infer that the compressibility effect in Case 3 flow must also be accompanied by a higher than predicted convection velocity.

5.3 Results For High Compressibility Reacting Flows

The measured temperature profiles for the Case 1 and Case 2 flows without chemical reactions are shown in Fig. 5.5. Remarkably enough, the profile shapes show a *deficit* inside the shear layer, with lower measured temperatures than in the high-speed free stream. It is unlikely that this deficit is reflects the actual temperature field (indicating a lingering effect of the splitter-plate thermal boundary layers, for example), since the Case 3 profile (Fig. 5.1) shows no such deficit. A more plausible explanation is that the recovery factor of the thermocouple probes is lower in the turbulent shear layer, for reasons that are currently unknown. In any case, the temperature increase in the subsequent kinetics and flip experiments is so high that those results are not very sensitive to such small variations in the non-reacting temperature profiles. The fitted lines shown in Fig. 5.5 are of the form

$$T_m(y) = a_1 + a_2 \tanh(a_3 + a_4 y) - a_5 \exp\left[a_6 + (y - a_7)^2\right], \qquad (5.3.1)$$

where the a_i are the fitted constants. The value of $T_m \sim -20\ K$ in the high-speed stream suggests a recovery factor of 0.84 (Eq. 5.1.2) which is slightly higher than that of the high-speed nitrogen flow (Case 3).

A comparison between the upstream shadowgraph views of the non-reacting and reacting Case 2 flows is presented in Fig. 5.6. The persistence of the travelling wave system in the presence of large heat release ($\Delta T_{\text{flm}} = 425\,K$) is confirmed here. Also note that the top edge of the shear layer is almost invisible in the reacting flow, indicating a close balance of density increase that is due to N_2 mixing and density decrease that is due to heat release. As with the medium compressibility flow (Fig. 5.2), there is no indication of hot vortex structures in these photographs.

The results of the kinetics study (Cases 2a, 2b and 2c) are presented in Fig. 5.7. The data reduction used here is exactly the same as that described for the Case 3 reacting flow except for the use of the slightly different non-reacting temperature profile (Fig. 5.5). The close agreement between the 4% and the 6% temperature profiles in Fig. 5.7 indicates that the fast chemistry regime has been attained in both flows. A problem arises, however, when one attempts to compute the characteristic chemical time, τ_c, of these cases on the basis of the model described in Section 2.4. Specifically, the model predicts very high mixed fluid temperatures ($T \sim 385\ K$) *prior* to any chemical reactions. This is due to the very high kinetic energy of the low-speed fluid in the convective reference frame (*i.e.* high M_{c2}), which is assumed to be completely converted to thermal energy in the mixed fluid (Eq. 2.4.9). However, such high temperatures are not confirmed by the thermocouple measurements (Fig. 5.5), the Schlieren photographs (Figs. 4.11 and 5.6) or the kinetics experiment (see discussion of Damköhler numbers to follow). Moreover, it is clear that the mean total temperature flux across the shear layer cannot be higher than the free stream stagnation temperatures because that would violate the law of conservation of energy.

To the extent that a steady-state stagnation point exists in the shear layer, however, the model prediction of $T \sim 385\ K$ has to be correct for the mixed fluid *at that stagnation point.* One must conclude, therefore, that this temperature is simply not representative of the rest of the fluid in the shear layer, particularly the mixed fluid which is undergoing chemical reactions. In other words, the non-detection of high average temperatures is the product of *intermittency*, in which a small amount of fluid is hot and the rest is cold. This conclusion basically contradicts the flow/kinetics model assumption that all or most of the kinetic energy of the free streams is converted into thermal energy upon entering the mixed fluid region (Eq. 2.4.9).

What the existing model *can* do is provide estimates for τ_c in the limiting cases of 0% and 100% kinetic energy conversion into thermal energy. It is these values

that are listed in Table 5.1 in the form of a Damköhler number range. Significantly, the low limiting value for Da in the fast kinetics, high compressibility flow (Case 2b) is exactly equal to the fast kinetics value of $Da \simeq 1.4$ found for the medium compressibility flow (Case 3b). This result suggests that there is very little kinetic energy conversion to thermal energy in this flow.

If one accepts the observaton that most of the shear layer fluid is cold and not hot, then one must also conclude that most of the shear layer fluid is travelling *slower* than the measured convection velocity, u_c. This is because mixed fluid convecting at the measured u_c must have a high stagnation temperature in the convective frame of reference ($T \sim 385\,K$ as discussed above), and these high temperatures are not observed. To emphasize this point, the measured shock wave convection velocity is apparently *not* a representative convection speed for the bulk of the fluid in the shear layer. The difficulties of understanding this difference in the context of travelling wave creation mechanisms remain unresolved.

Despite these unresolved questions, the experimental results in Fig. 5.7 are sufficient to establish the fast chemistry limit for this high compressibility flow. On this basis then, was the flip experiment conducted. Unfortunately, the previously noted limitations on the maximum fluorine concentration restricted this flip experiment to $\xi_0 = 0.25$ ($\phi = 1/3, 3$). Note the implicit assumption that a 3% lean concentration would be sufficient to produce fast chemistry, an assumption supported by the computed Damköhler numbers listed in Table 5.1. The temperature profiles for this flip experiment (Cases 1a and 1b) are presented in Fig. 5.8, along with the $\phi = 1$ run (Case 2b).

The first thing to note is that the temperature thickness of the $\phi = 1/3$ run (Case 1a) is about the same as that of the $\phi = 3$ run. The curious layer thickening observed in the medium compressibility experiment is not seen here. Again, this result cannot be adequately explained at the present time; however, one can speculate that the travelling waves in the high compressibility flow serve as a stabilization mechanism, which resists the perturbing influence of the heat release in the layer. Whatever the reason, the confidence in this flip experiment can be considered higher than the medium compressibility flow because of the near constancy of the overall growth rate.

The observation that the product thickness of the $\phi = 1/3$ profile is clearly much lower than of the other profiles immediately suggests that $E_n > 1$. From Eqs.

2.3.11, 2.3.12 and 2.3.5:

$$\frac{\delta_m}{\delta} \simeq (1 - 0.25)(0.188 + 0.226) = 0.31 \ , \tag{5.3.2a}$$

$$\bar{\xi} \simeq \frac{0.226}{0.226 + 0.188} = 0.55 \tag{5.3.3b}$$

and

$$E_n \simeq \frac{0.546}{1 - 0.546} = 1.2 \ . \tag{5.3.4c}$$

The mixed fluid fraction of this flow is significantly lower than that of the Case 3 flow (recall $\delta_m/\delta \simeq 0.40$). This $\sim 23\%$ reduction is almost certainly a compressibility effect because Re_δ is almost the same for the Case 1 and Case 3 flows. Here then is strong evidence that compressibility not only reduces the overall growth rate of the shear layer, it also reduces the normalized mixing rate inside the shear layer.

If one again accepts the validity of Eqs. 2.3.6 and 2.3.7 for estimating E_n, then the measured value of $E_n \simeq 1.2$ requires a convection velocity of $u_c = 747\ m/s$. This is considerably larger than the isentropic pressure matching model value from Eq. 2.2.12 of $u_c = 411\ m/s$, but also less than the measured convection velocity of $905\ m/s$. Note that for $u_c = 411\ m/s$, $E_n = 4.68$ and for $u_c = 905\ m/s$, $E_n = 0.58$, which demonstrates the sensitivity of this model to the specific value of u_c.

CHAPTER 6
Conclusions

A new wind tunnel facility has been constructed and utilized to study two-dimensional, compressible, turbulent shear layers. The experiments consisted of both non-reacting and reacting flows designed to investigate the various properties of the shear layer: structure, growth rate, entrainment, mixing and combustion. These experiments were, in many respects, limited to fairly small excursions into the rather large parameter space of compressible, turbulent shear layer phenomena. Nevertheless, a number of conclusions can be drawn from the available data, with varying degrees of confidence. These conclusions are listed below:

1. Large-scale, two-dimensional structure was generally not seen in these shear layers, except for the two experiments in which *both* free stream velocities were subsonic. This compressibility effect does not appear to be uniquely scaled by the convective Mach number, but rather depends on the existence of *supersonic* free stream flow on the high speed side. The inference to be drawn from this is that the hyperbolic character of such a supersonic region inhibits a downstream-to-upstream feedback mechanism, which promotes the formation of large scale, two-dimensional structure.

2. There were two exceptions to the preceding conclusion; that is, supersonic flows were found in which large-scale, two-dimensional structure *was* observed. The first involved planar shock wave interactions with the shear layer, in which a suspected resonance condition enhanced the two-dimensional structure content of the shear layer. The shock wave in question was deliberately produced by a pressure mis-match at the splitter tip. This structure enhancement was seen only in the medium compressibility flow (Case 3) with $M_{c1} \simeq 0.51$. The second exception involved a strange transitional behaviour seen in the low compressibility, low density ratio flows (see 9 below).

3. Travelling shock and expansion wave systems were observed in the high compressibility flows, evidently created by turbulent structures convecting at supersonic velocities. For the two flows in which such waves were observed, they existed *only* in the low-speed fluid.

4. The convection velocities derived from the analysis of these travelling waves are significantly higher than those predicted by the usual isentropic pressure-matching arguments. They are also in general agreement with the earlier results of Papamoschou (1989).

5. However, these travelling wave propagation velocities are apparently much higher than the mean convection velocity of the fluid inside the shear layer. The specific creation mechanism for these waves remains unknown at the present time.

6. On the basis of the simple flow/kinetics model described herein, the fast-chemistry limit was found to be $Da \simeq 1.4$, although the modelling difficulties alluded to in Item 5 above render this value somewhat tentative. This is somewhat lower than the results for incompressible flow as obtained by Mungal & Frieler (1988).

7. The flip experiments yield $\delta_m/\delta \simeq 0.40$ and $\delta_m/\delta \simeq 0.31$ for the medium and high compressibility flows, respectively. The difference is attributable to compressibility effects because the flows have roughly the same Re_δ. Both results are lower than the value of $\delta_m/\delta \simeq 0.49$ (Dimotakis 1989), for incompressible flow, although some of *this* difference may be due to the factor of ten increase in Re_δ for the compressible experiments.

8. The flip experiments yield $E_n \simeq 1.07$ and $E_n \simeq 1.2$ for the medium and high compressibility flows, respectively. On the basis of the Dimotakis (1984) model for incompressible flow, these results suggest higher convection velocities than would be predicted from the usual isentropic pressure matching arguments. Alternatively, one could say that compressibility effects *decrease* E_n as compared to the extrapolated incompressible values. However, for the high compressibility flow, the value of $E_n \simeq 1.2$ suggests $u_c = 747\ m/s$ as compared to $u_c = 905\ m/s$ as derived from the travelling wave-system analysis.

9. The measured normalized growth rates for this study agree with the previous measurements by other experimenters, except at the low convective Mach numbers, *i.e.* $M_{c1} < 0.3$. The current data show unexpectedly low growth rates for the supersonic flows in this range. These flows also happen to possess lower density ratios than any published data to date. On the basis of the growth rate data and the photographic evidence of unusual structure, one can conclude that a new growth rate mechanism has been encountered. An understanding of this new mechanism does not exist at the present time.

10. The measured growth rates of the supersonic M_1 shear layers were remarkably insensitive to the effects of incident shock/expansion waves and of large heat release inside the shear layer. In both cases, the changes in δ/x were on the order of $\pm 10\%$ at most.

Perhaps the greatest limitation of these experiments has been the inability to peer inside the shear layer and visualize its interior structure. Resolution of many of the unsolved problems discussed herein is probably contingent on something like planar Rayleigh scattering diagnostics which would be capable of "slicing" the flow and negating the masking effects of spanwise integration across the test section. In view of the current results and outstanding problems, such experiments should be placed at or near the top of the priority list for future experiments.

References

BAULCH, D. L., DUXBURY, G. J., GRANT, S. J. and MONTAGUE, D. C. [1981] "Evaluated Kinetic Data for High Temperature Reactions, Vol. 4", J. Phys. Chem. Ref. Data, Vol. 10, Suppl. 1.

BERNAL, L. P. and ROSHKO, A. [1986] "Streamwise vortex structure in plane mixing layers", *J. Fluid Mech.* **170**, 499–525.

BOGDANOFF, D. W. [1983] "Compressibility Effects in Turbulent Shear Layers", (TN) *AIAA J.* **21**(6), 926–927.

BRADSHAW, P. [1966] "The Effect of Initial Conditions on the Development of a Free Shear Layer", *J. Fluid Mech.* **26**(2), 225–236.

BREIDENTHAL, R. E. [1981] "Structure in Turbulent Mixing Layers and Wakes Using a Chemical Reaction", *J. Fluid Mech.* **109**, 1–24.

BROADWELL, J. E. and BREIDENTHAL, R. E. [1982] "A Simple Model of Mixing and Chemical Reaction in a Turbulent Shear Layer", *J. Fluid Mech.* **125**, 397–410.

BROADWELL, J. E. and MUNGAL, M. G. [1988] "Molecular Mixing and Chemical Reactions in Turbulent Shear Layers", Proceedings, 22nd *Symposium (International) on Combustion* (The Combustion Institute), 579–587.

BROADWELL, J. E. and MUNGAL, M. G. [1990] "Large-scale Structures and Molecular Mixing", Presented, *IUTAM Symposium of Fluid Mechanics of Stirring and Mixing* (La Jolla, California), 20-24 August 1990.

BROWAND, F. K. and LATIGO, B. O. [1979] "Growth of the Two-Dimensional Mixing Layer from a Turbulent and Non-Turbulent Boundary Layer", *Phys. Fluids* **22**(6), 1011–1019.

BROWN, G. L. [1974] "The Entrainment and Large Structure in Turbulent Mixing Layers", Proceedings, 5th *Australasian Conf. on Hydraulics and Fluid Mechanics*, 352–359.

BROWN, G. L. and ROSHKO, A. [1971] "The Effect of Density Difference on the Turbulent Mixing Layer", *Turbulent Shear Flows*, AGARD–CP–93, 23.1–12.

BROWN, G. L. and ROSHKO, A. [1974] "On Density Effects and Large Structure in Turbulent Mixing Layers", *J. Fluid Mech.* **64**(4), 775–816.

CHINZEI, N., MASUA, G., KOMURO, T. MURAKAMI, A. and KUDOU, K. [1986] "Spreading of two-stream supersonic turbulent mixing layers", *Phys. Fluids* **29**(5), 1345-1347.

CLARK, JR. R. L., NG, W. F., WALKER, D. A. and SCHETZ, J. A. [1990] "Large-Scale Structure in a Supersonic Slot-Injected Flow field", *AIAA J.* **28**(6), 1045–1051.

CLEMENS, N. T., MUNGAL, M. G., BERGER, T. E. and VANDSBURGER, U. [1990] "Visualizations of the structure of the turbulent mixing layer under compressible conditions", *AIAA* 28th *Aerospace Sciences Meeting*, 8–11 January 1990 (Reno, Nevada), paper AIAA–90–0500.

CLEMENS, N. T. and MUNGAL, M. G. [1990] "Two- and Three-Dimensional Effects in the Supersonic Mixing Layer", 26th *AIAA/SAE/ASME/ASEE Joint Propulsion Conference* (Orlando, FL), 10–12 July 1990, AIAA–90–1978.

COHEN, N. and BOTT, J. F. [1982] "Review of Rate Data for Reactions of Interest in HF and DF Lasers", AFWL Report SD–TR–82–86.

COLES, D. [1985] "Dryden Lecture: The Uses of Coherent Structure", *AIAA* 23rd *Aerospace Sciences Meeting*, 14–17 January 1985 (Reno, Nevada), AIAA Paper 85–0506.

DIMOTAKIS, P. E. [1984] "Two-dimensional shear-layer entrainment", *AIAA* 22nd *Aerospace Sciences Meeting*, 9–12 January 1984 (Reno, Nevada), AIAA–84–0368. Published, *AIAA J.* **24**(11), 1791–1796 (1986).

DIMOTAKIS, P. E. [1987] "Turbulent shear layer mixing with fast chemical reactions", US-France Workshop on Turbulent Reactive Flows (Rouen, France), 7–10 July 1987. Published: *Turbulent Reactive Flows*, (eds. R. Borghi and S. N. B. Murthy, *Lecture Notes in Engineering* **40**, Springer-Verlag New York Inc., 1989), 417–485.

DIMOTAKIS, P. E. [1989] "Turbulent Free Shear Layer Mixing", *AIAA* 27th *Aerospace Sciences Meeting*, 9–12 January 1989 (Reno, Nevada), AIAA–89–0262.

DIMOTAKIS, P. E. and BROWN, G. L. [1976] "The Mixing Layer at High Reynolds Number: Large-Structure Dynamics and Entrainment", *J. Fluid Mech.* **78**(3), 535–560 + 2 plates.

DIMOTAKIS, P. E. and HALL, J. L. [1987] "A simple model for finite chemical kinetics analysis of supersonic turbulent shear layer combustion", AIAA/SAE/-ASME/ASEE 23^{rd} Joint Propulsion Meeting (La Jolla, CA), 29 June – 1 July 1987, AIAA Paper 87–1879.

DUTTON, J. C., BURR, R. F., GOEBEL, S. G. and MESSERSMITH, N. L. [1990] "Compressibility and Mixing in Turbulent Free Shear Layers", Twelfth Symposium on Turbulence (preprints), September 24-26, at the University of Missouri-Rolla.

FOURGUETTE, D. and DIBBLE, R. [1990] "Time Evolution of the Shear Layer of a Supersonic Jet at Matched Conditions", *AIAA* 28th *Aerospace Sciences Meeting*, 8–11 January 1990 (Reno, Nevada), AIAA–90–0508.

FRIELER, C. E. and DIMOTAKIS, P. E. [1988] "Mixing and Reaction at Low Heat Release in the Non-Homogeneous Shear Layer", *First National Fluid Dynamics Congress*, 24–28 July 1988 (Cincinatti, Ohio), AIAA Paper 88–3626.

GOEBEL, S. G. and DUTTON, J. C. [1990] "An Experimental Investigation of Compressible, Turbulent Mixing Layers", Technical Report Number UILU ENG 90-4005.

HALL, J. and DIMOTAKIS, P. E. [1989] "Design Overview of the Supersonic Hydrogen-Fluorine Facility (V4.0)", GALCIT Internal Report, 30 August 1989 (available from the authors on request).

HERMANSON, J. C. and DIMOTAKIS, P. E. [1989] "Effects of heat release in a turbulent reacting shear layer", *J. Fluid Mech.* **199**, 333–375.

— [1989] *IMSL User Manual: Fortran Subroutines for Mathematical Applications, Version 1.1* (Printed by IMSL Inc., Houston, Texas).

JACHIMOWSKI, C. J. [1988] "An Analytical Study of the Hydrogen-Air Reaction Mechanism With Application to Scramjet Combustion", NASA Tech. Paper 2791.

KEE, R. J., MILLER, J. A. and JEFFERSON, T. H. [1980] "CHEMKIN: A General Purpose, Problem-independent, Transportable, Fortran Chemical Kinetics Code Package", SANDIA Report SAND80–8003.

KONRAD, J. H. [1976] *An Experimental Investigation of Mixing in Two-Dimensional Turbulent Shear Flows with Applications to Diffusion-Limited Chemical Reactions*, Ph.D. thesis, California Institute of Technology (also Project SQUID Technical Report CIT–8–PU, December 1976).

KOOCHESFAHANI, M. M. and DIMOTAKIS, P. E. [1986] "Mixing and chemical reactions in a turbulent liquid mixing layer", *J. Fluid Mech.* **170**, 83–112.

KOOCHESFAHANI, M. M. and FRIELER, C. E. [1987] "Inviscid Instability Characteristics of Free Shear Layers with non-Uniform Density", *AIAA* 25^{th} *Aerospace Sciences Meeting*, 12–15 January 1987 (Reno, Nevada), AIAA Paper 87-0047.

LELE, S. K. [1989] "Direct Numerical Simulation of Compressible Free Shear Flows", *AIAA* 27^{th} *Aerospace Sciences Meeting*, 9–12 January 1989 (Reno, Nevada), AIAA Paper 89–0374.

LESSEN, M., FOX, J. A. and ZIEN, H. M. [1965] "On the Inviscid Stability of the Laminar Mixing of Two Parallel Streams of a Compressible Fluid", J. Fluid Mech., **23**, 355-367..

LOEHRKE, R. I. and NAGIB, H. [1972] "Experiments on Management of Free-Stream Turbulence", *AGARD Rep. No. 598.*

LOWSON, M. V. and OLLERHEAD, J. B. [1968] "Visualization Of Noise From Cold Supersonic Jets", *Journal of the Acoustical Society of America,* **44**, *No. 2.*

MUNGAL, M. G. [1983] *Experiments on Mixing and Combustion with Low Heat Release in a Turbulent Shear Flow*, Ph.D. thesis, California Institute of Technology.

MUNGAL, M. G. and DIMOTAKIS, P. E. [1984] "Mixing and combustion with low heat release in a turbulent mixing layer", *J. Fluid Mech.* **148**, 349-382.

MUNGAL, M. G, HERMANSON, J. C. and DIMOTAKIS, P. E. [1985] "Reynolds Number Effects on Mixing and Combustion in a Reacting Shear Layer", *AIAA J.* **23**(9), 1418–1423.

MUNGAL, M. G. and FRIELER, C. E. [1988] "The Effects of Damköhler Number in a Turbulent Shear Layer", *Comb. and Flame* **71**, 23–34.

OERTEL, H. [1979] *Mach Wave Radiation Of Hot Supersonic Jets Investigated by Means of The Shock Tube and New Optical Techniques* (Shock Tubes and Waves: Proceedings of the 12^{th} International Symposium on Shock Tubes and Waves, Jerusalem, July 16-19, 1979).

ORTWERTH, P. J. and SHINE, A. J. [1977] "On Scaling of Plane Turbulent Shear Layers", Air Force Weapons Laboratory Technical Report AFWL-TR-77-118.

PAPAMOSCHOU, D. [1989] "Structure of the compressible turbulent shear layer", *AIAA* 27^{th} *Aerospace Sciences Meeting*, 9–12 January 1989 (Reno, Nevada), AIAA Paper 89–0126.

PAPAMOSCHOU, D. and ROSHKO, A. [1988] "The Compressible Turbulent Shear Layer: An Experimental Study", *J. Fluid Mech.* **197**, 453–477.

PEPIN, F. E. and DIMOTAKIS, P. E. [1989] "The DUCT Solver", Internal CADRE documentation, California Institute of Technology(unpublished).

PRESS, W. H., FLANNERY, B. P., TEUKOLSKY, S. A. and VETTERLING, W. T. [1989] *Numerical Recipes (Fortran version)* (Press Syndicate of the University of Cambridge).

RAGAB, S. A. and WU, J. L. [1987] "Linear Instability Waves in Supersonic Turbulent Mixing", AIAA *19^{th} Fluid Dynamics, Plasma Dynamics and Lasers Conference* (Honolulu, Hawaii), 6-10 June 1987, AIAA–87–1418.

ROARK, R. J. and YOUNG, W. C. [1982] *Formulas for Stress and Strain, 5^{th} ed.* (McGraw-Hill Book Co.).

SHAU, Y. R. and DOLLING, D. S. [1990] "The Detection of Large Scale Structure in Undisturbed and Disturbed Compressible Shear Layers", *AIAA* 28^{th} *Aerospace Sciences Meeting*, 8–11 January 1990 (Reno, Nevada), AIAA–90–0711.

SIVELLS, J. C. [1978] "A computer program for the aerodynamic design of axisymmetric and planar nozzles for supersonic and hypersonic wind tunnels", AEDC–TR–78–63.

TAM, C. K. W. [1971] "Directional acoustic radiation from a supersonic jet", *J. Fluid Mech.* **46**(4), 757–768.

TAM, C. K. W. and HU, F. Q. [1989] "The instability and acoustic wave modes of supersonic mixing layers inside a rectangular channel", *J. Fluid Mech.* **203**, 51–76.

WALLACE, A. K. [1981] *Experimental Investigation on the Effects of Chemical Heat Release in the Reacting Turbulent Plane Shear Layer*, Ph.D. thesis, University of Adelaide (also distributed as AFOSR-TR-84-0650).

ZHUANG, M., KUBOTA, T. and DIMOTAKIS, P. E. [1988] "On the Stability of Inviscid, Compressible Free Shear Layers", Proceedings, *First National Fluid Dynamics Congress*, 25–28 July 1988 (Cincinnati, Ohio), **II**, 768–773.

ZHUANG, M., DIMOTAKIS, P. E. and KUBOTA, T. [1990] "The Effect of Walls on a Spatially Growing Supersonic Shear Layer", *Phys. Fluids* A **2**(4), 599–604.

Table 2.1: Description Of The Hydrogen-Fluorine-Nitric Oxide Chemical Reaction Mechanism

No.	Reaction	Source	A	β	E
1	$NO + F_2 \rightarrow NOF + F$	Baulch	4.2×10^{11}	0.0	2285
2	$NO + F + M \rightarrow NOF + M$	Baulch	3.0×10^{16}	0.0	0
3	$H + F_2 \rightarrow HF + F$	Cohen-Bott	2.9×10^{9}	1.4	1325
4	$F + H_2 \rightarrow HF + H$	Cohen-Bott	2.7×10^{12}	0.5	634
5	$F_2 + M \rightarrow F + F + M$	Baulch	2.1×10^{13}	0.0	33700
6	$H + F + M \rightarrow HF + M$	Baulch	7.5×10^{18}	-1.0	0
7	$H + H + M \rightarrow H_2 + M$	Jachimowski	6.4×10^{17}	-1.0	0
8	$H + NO + M \rightarrow HNO + M$	Jachimowski	5.4×10^{15}	0.0	-302
9	$H + HNO \rightarrow NO + H_2$	Jachimowski	4.8×10^{12}	0.0	0

The kinetics data listed here are given in cgs units. The use of the symbol M in the above chemical equations denotes *any* chemical species present in the reacting mixture. Hence, n_M is the sum of all constitutent chemical species.

An example of Eq. 2.4.4 showing the chemical production of HF for this chemical system is shown below; *i.e.*,

$$\dot{n}_{HF} = k_{f3}\frac{n_H\, n_{F2}}{V} + k_{f4}\frac{n_F\, n_{H2}}{V} + k_{f6}\frac{n_H\, n_F\, n_M}{V^2} + k_{r3}\frac{n_{HF}\, n_M}{V} + k_{r4}\frac{n_{HF}\, n_H}{V} + k_{r6}\frac{n_{HF}\, n_M}{V^2} \ ,$$

where the k_{fi} are the forward reaction rate coefficients defined in Eq. 2.4.6, and the k_{ri} are the reverse reaction rate coefficients defined in Eq. 2.4.7 .

Table 4.1: Summary Of Non-Reacting Runs

Case	1	2	3	4	5	6
Side 1 Gases	100% He	100% He	100% N_2	100% N_2	100% N_2	100% N_2
Side 2 Gases	100% Ar	100% N_2	100% N_2	33% He 66% Ar	60% He 40% Ar	75% He 25% Ar
M_1	1.50	1.48	1.46	1.48	1.48	1.47
M_2	0.35	0.30	0.29	0.44	0.42	0.36
$r = u_2/u_1$	0.096	0.092	0.235	0.385	0.445	0.459
$s = \rho_2/\rho_1$	5.950	4.120	0.713	0.706	0.484	0.338
$M_{c1}^{(i)}$	0.962	0.906	0.511	0.426	0.336	0.292
$(\delta/x)_{inc}$	0.429	0.395	0.200	0.149	0.122	0.115
$(\delta/x)_{vis}$	0.100	0.108	0.114	0.092	0.083	0.084
$\delta_{vis}/\delta_{inc}$	0.233	0.274	0.570	0.630	0.680	0.730
Re_x	7.4×10^6	7.0×10^6	9.6×10^6	3.7×10^6	2.4×10^6	2.1×10^6
β	0°	1°	2°	0°	0.5°	0.5°

Table 4.1 (Continued)

Case	7	8	9	10	11
Side 1 Gases	100% N_2	100% N_2	100% Ar	100% N_2	100% N_2
Side 2 Gases	90% He 10% Ar	100% He	100% He	33% He 66% Ar	100% He
M_1	1.48	1.48	1.50	0.59	0.65
M_2	0.28	0.23	0.23	0.27	0.10
$r = u_2/u_1$	0.469	0.510	0.636	0.510	0.462
$s = \rho_2/\rho_1$	0.194	0.101	0.058	0.958	0.132
$M_{c1}^{(i)}$	0.240	0.175	0.106	0.143	0.093
$(\delta/x)_{inc}$	0.108	0.094	0.067	0.110	0.107
$(\delta/x)_{vis}$	0.073	0.062	0.040	0.101	0.097
$\delta_{vis}/\delta_{inc}$	0.678	0.660	0.597	0.918	0.907
Re_x	1.8×10^6	1.8×10^6	1.1×10^6	1.5×10^6	6.9×10^5
β	1°	2°	2°	0.5°	1.0°

Here, $M_{c1(isen)}$ was computed by Eq. 2.2.12, and $(\delta/x)_{inc}$ was computed from Eq. 2.2.3 . When different gases were present, their properties were averaged for the computation of Re_x .

Table 5.1: Summary Of Reacting Runs

Case	3a	3b	3c	3d	3e
Side 1 Gases	1% H_2 .25% NO 98.75% N_2	2% H_2 .25% NO 97.75% N_2	4% H_2 .25% NO 95.75% N_2	8% H_2 .25% NO 91.75% N_2	2% H_2 .25% NO 97.75% N_2
Side 2 Gases	1% F_2 99% N_2	2% F_2 98% N_2	4% F_2 96% N_2	2% F_2 98% N_2	8% F_2 92% N_2
ϕ	1	1	1	1/4	4
ΔT_{flm}	89 K	181 K	365 K	295 K	291 K
$(\Delta T/\Delta T_{\text{flm}})_{\max}$	0.344	0.596	0.573	0.522	0.561
δ_T	45.5 mm	48.5 mm	49.8 mm	64.2 mm	48.7 mm
δ_P/δ_T	0.179	0.276	0.276	0.243	0.259
Da	0.23	1.4	5.3	1.7	18
β	2°	0.5°	−1°	0.5°	0.5°

Table 5.1 (Continued)

Case	2a	2b	2c	1a	1b
Side 1 Gases	2% H_2 .25% NO 97.75% He	4% H_2 .25% NO 95.75% He	6% H_2 .25% NO 93.75% He	9% H_2 .25% NO 90.75 He	3% H_2 .25% NO 96.75% He
Side 2 Gases	2% F_2 98% N_2	4% F_2 96% N_2	6% F_2 94% N_2	3% F_2 97% Ar	9% F_2 91% Ar
ϕ	1	1	1	1/3	3
ΔT_{flm}	214 K	425 K	633 K	578 K	575 K
$(\Delta T/\Delta T_{\text{flm}})_{\max}$	0.534	0.627	0.664	0.471	0.620
δ_T	60.5 mm	54.7 mm	55.2 mm	54.3 mm	62.7 mm
δ_P/δ_T	0.198	0.252	0.262	0.188	0.226
Da	0.34 → 1.7	1.4 → 4.0	2.8 → 5.6	0.9 → 3.0	5.4 → 10.5
β	0.2°	−1°	−1.5°	−1.5°	−1.5°

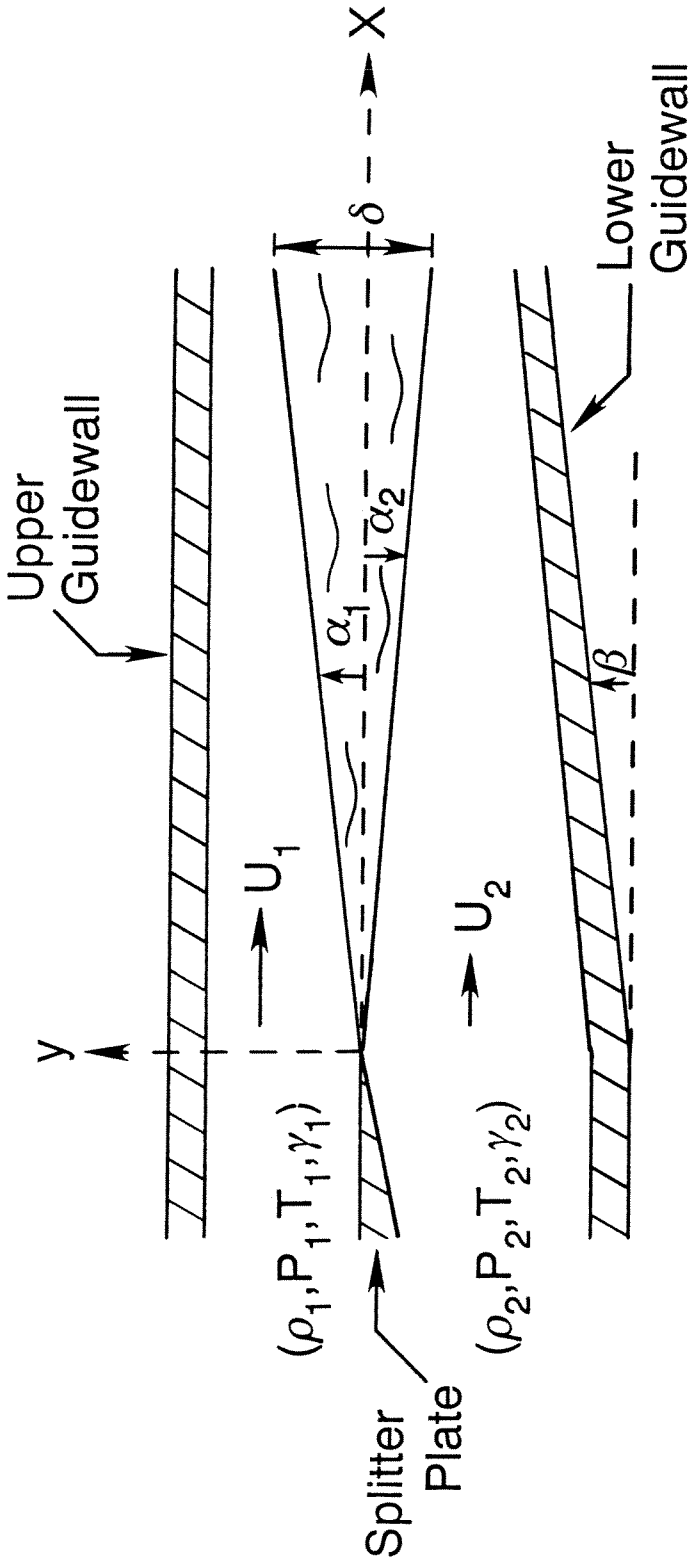

Fig. 2.1: Shear Layer Geometry.

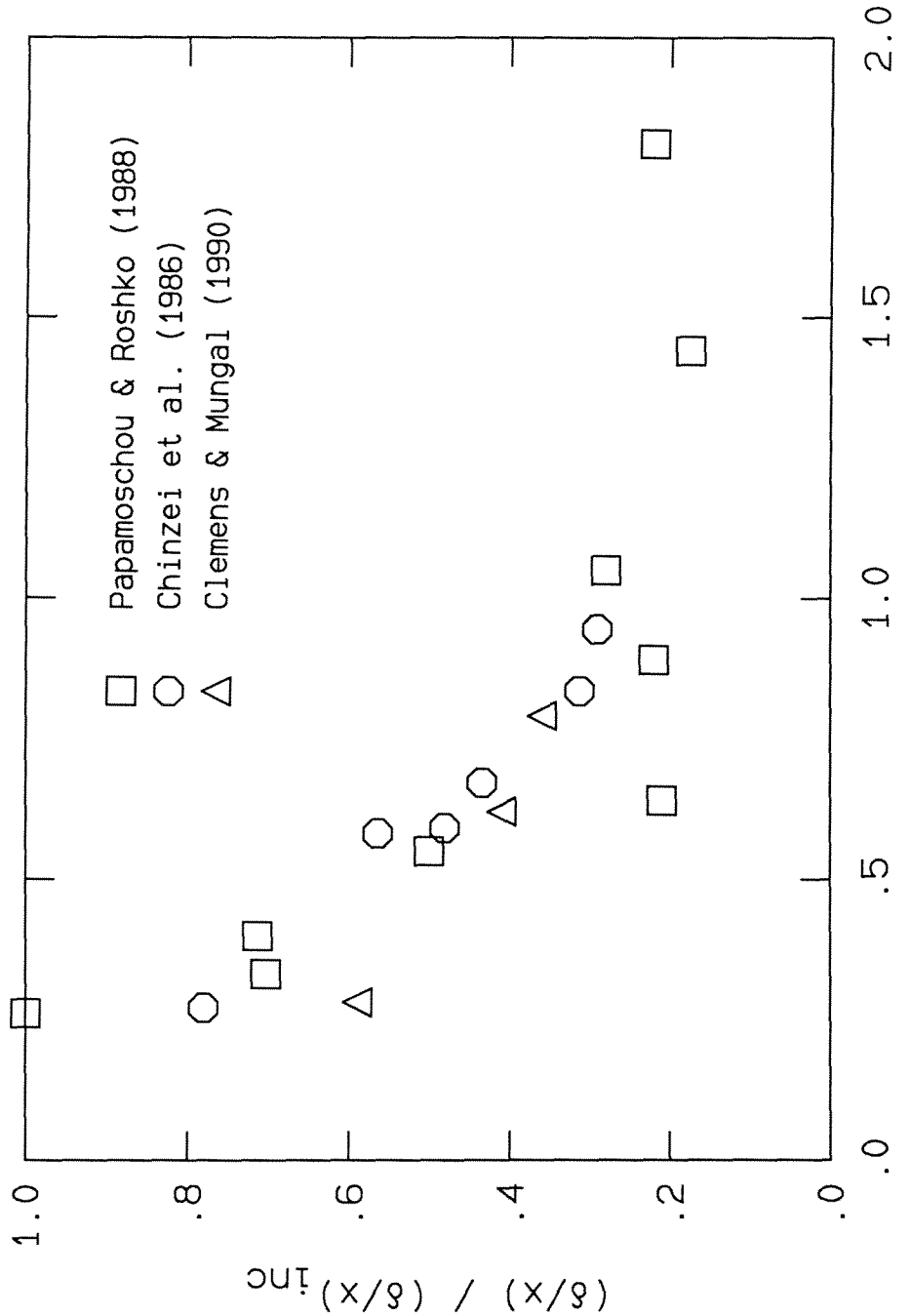

Fig. 2.2: Normalized Growth Rate Data Compiled By Previous Researchers.

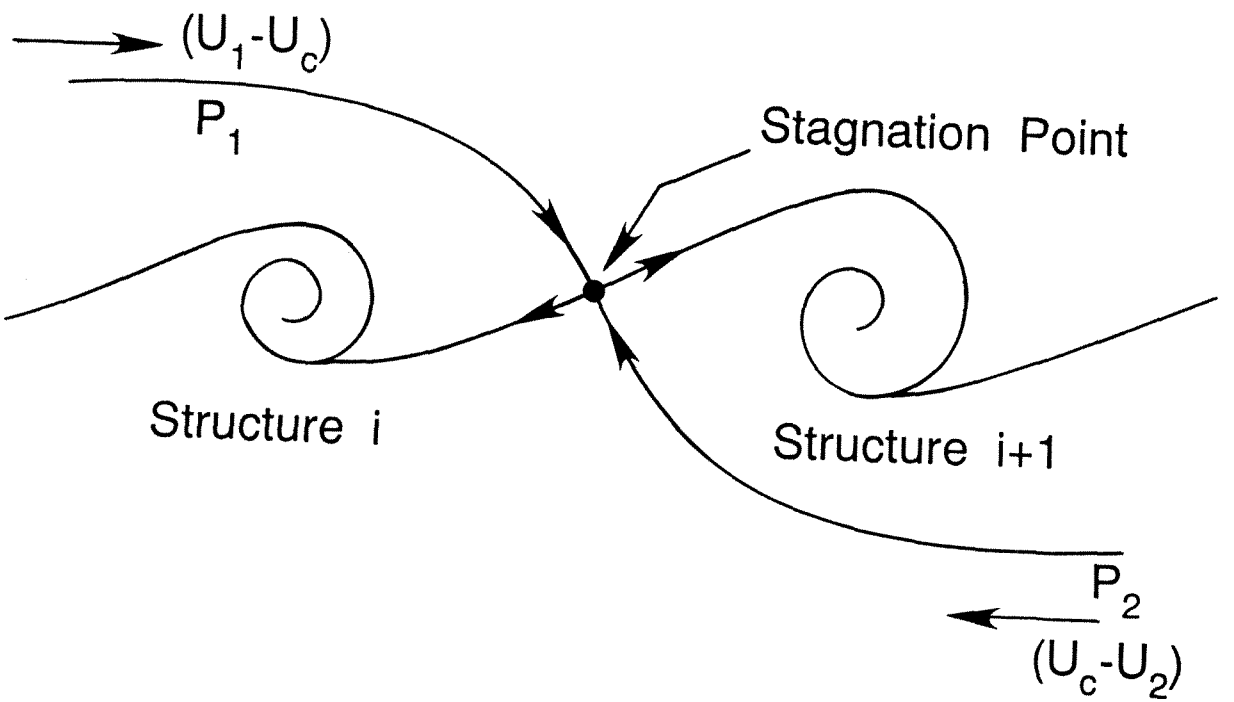

Fig. 2.3: Convective Frame Isentropic Pressure Matching Model For Shear Layer.

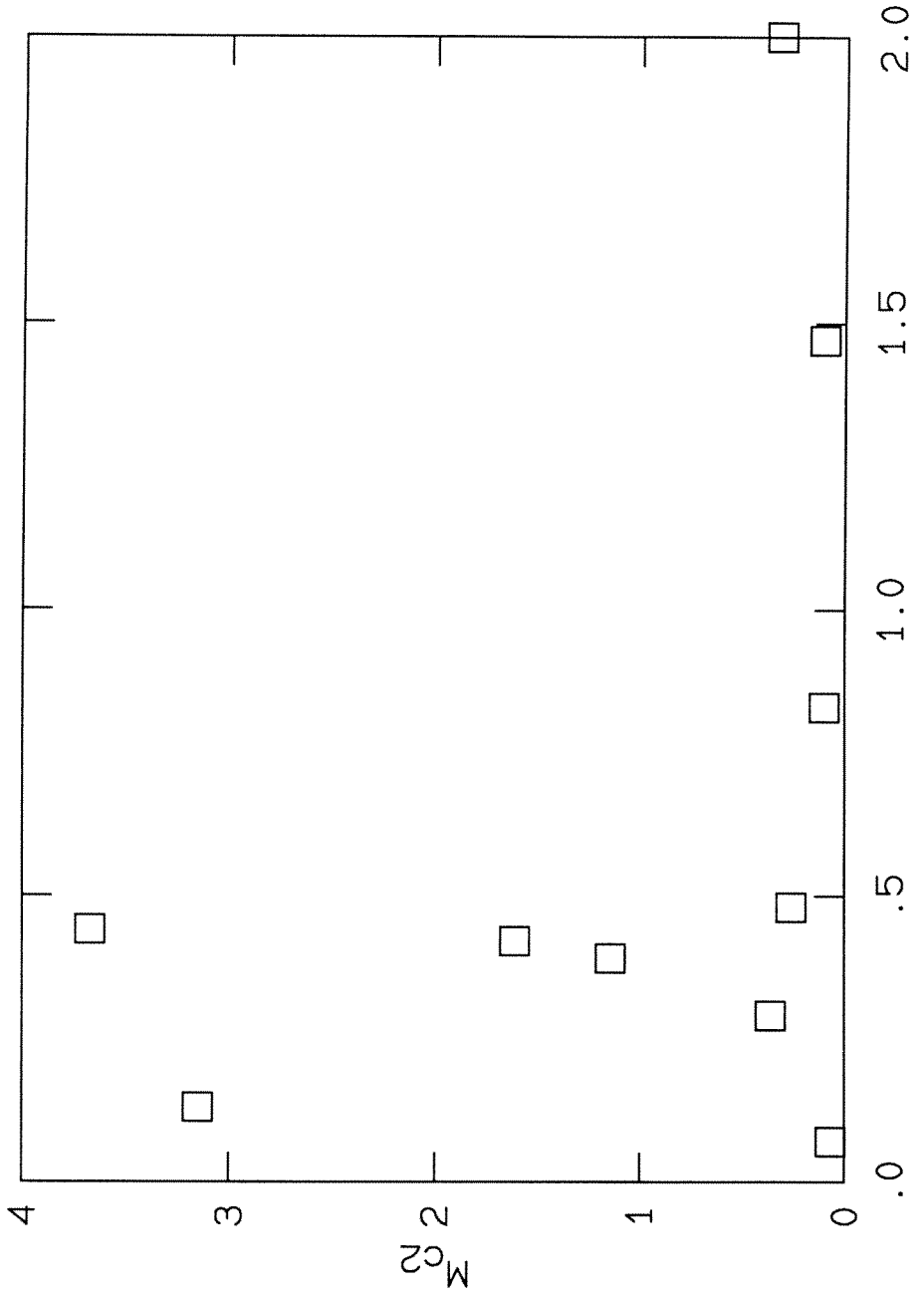

Fig. 2.4: Unequal Convective Mach Numbers Measured by Papamoschou (1989).

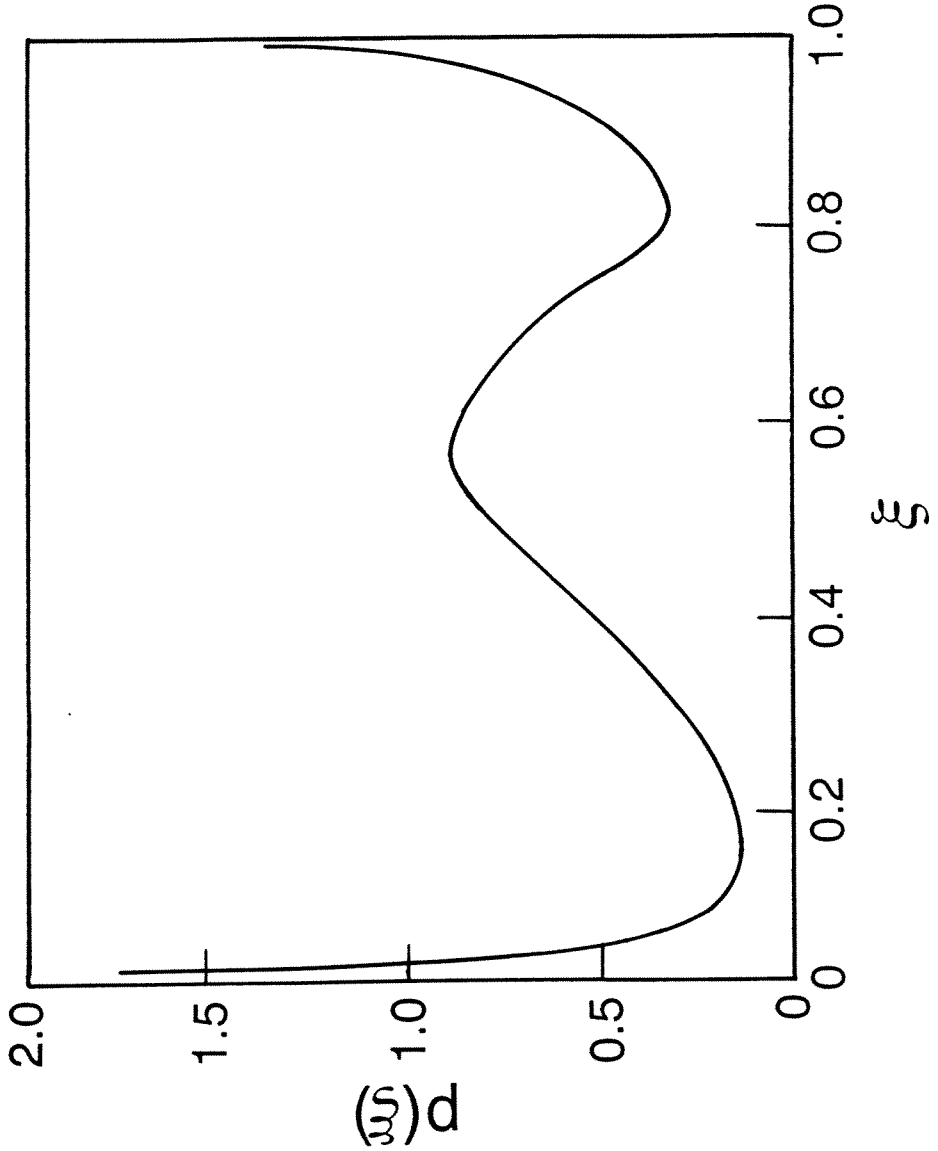

Fig. 2.5: Sketch Of Mixture Ratio PDF For Shear Layer (Dimotakis 1989).

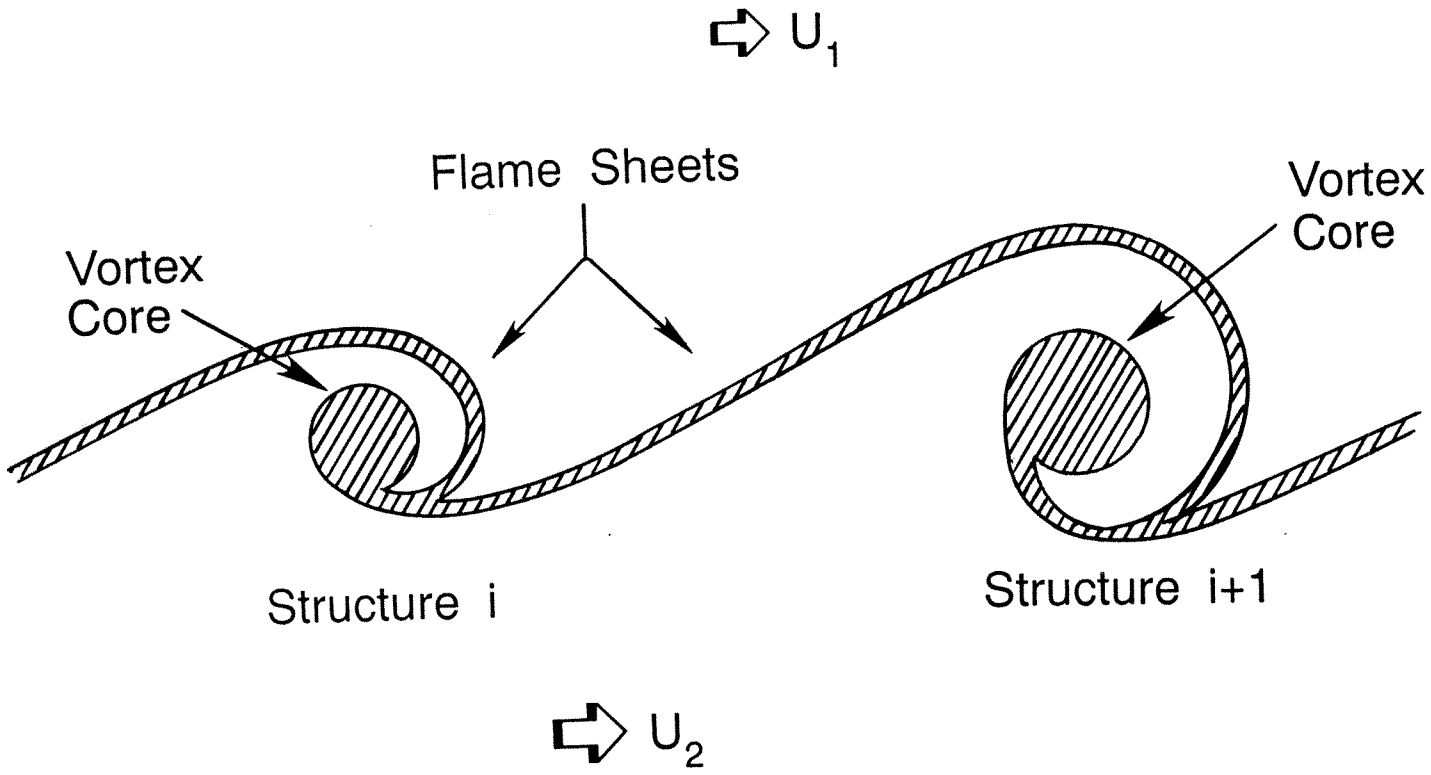

Fig. 2.6: Sketch Of Broadwell-Breidenthal-Mungal Model For Mixed Fluid In A Shear Layer.

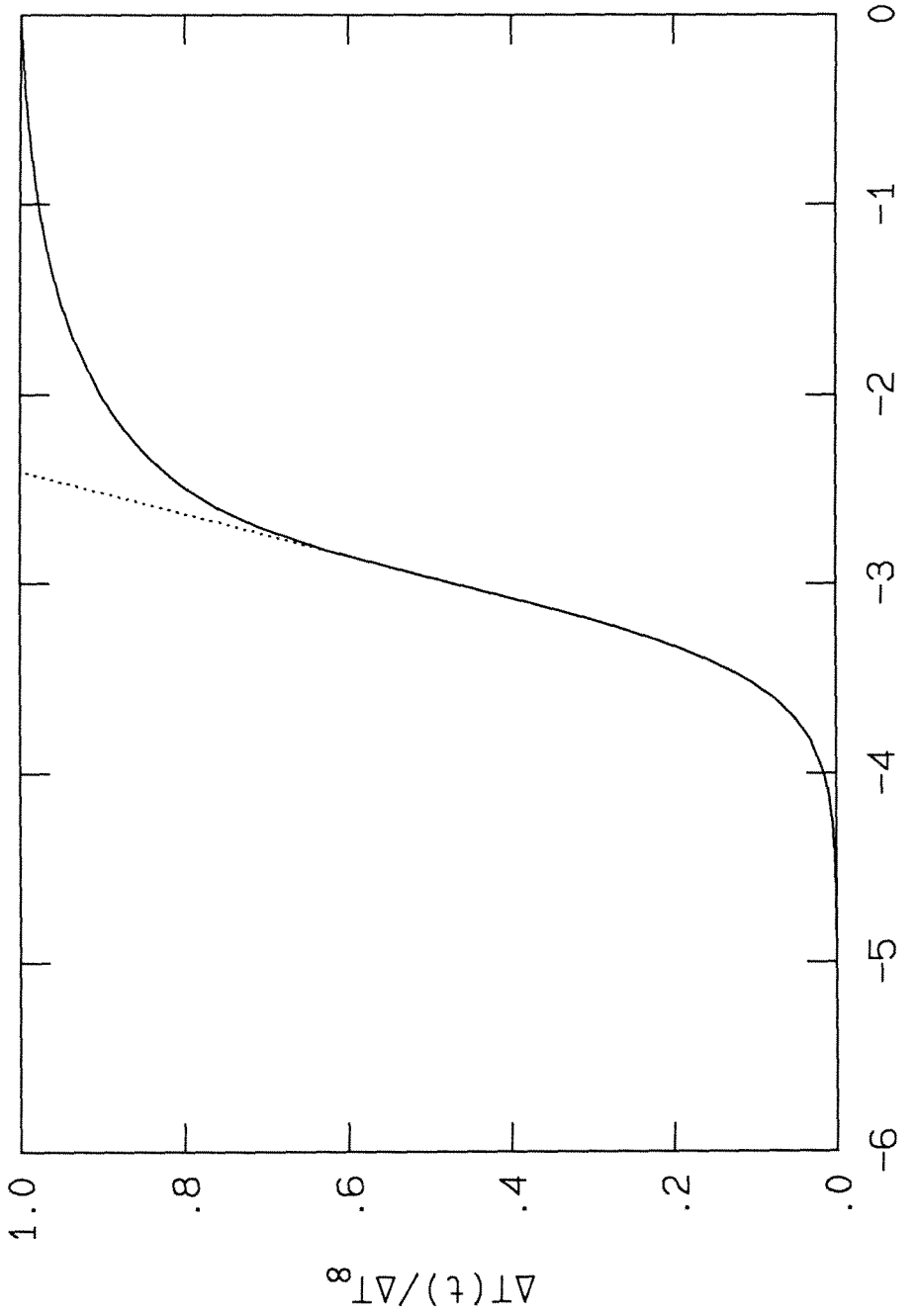

Fig. 2.7: Mungal-Frieler (1988) Fast Chemistry Case Recalculated.

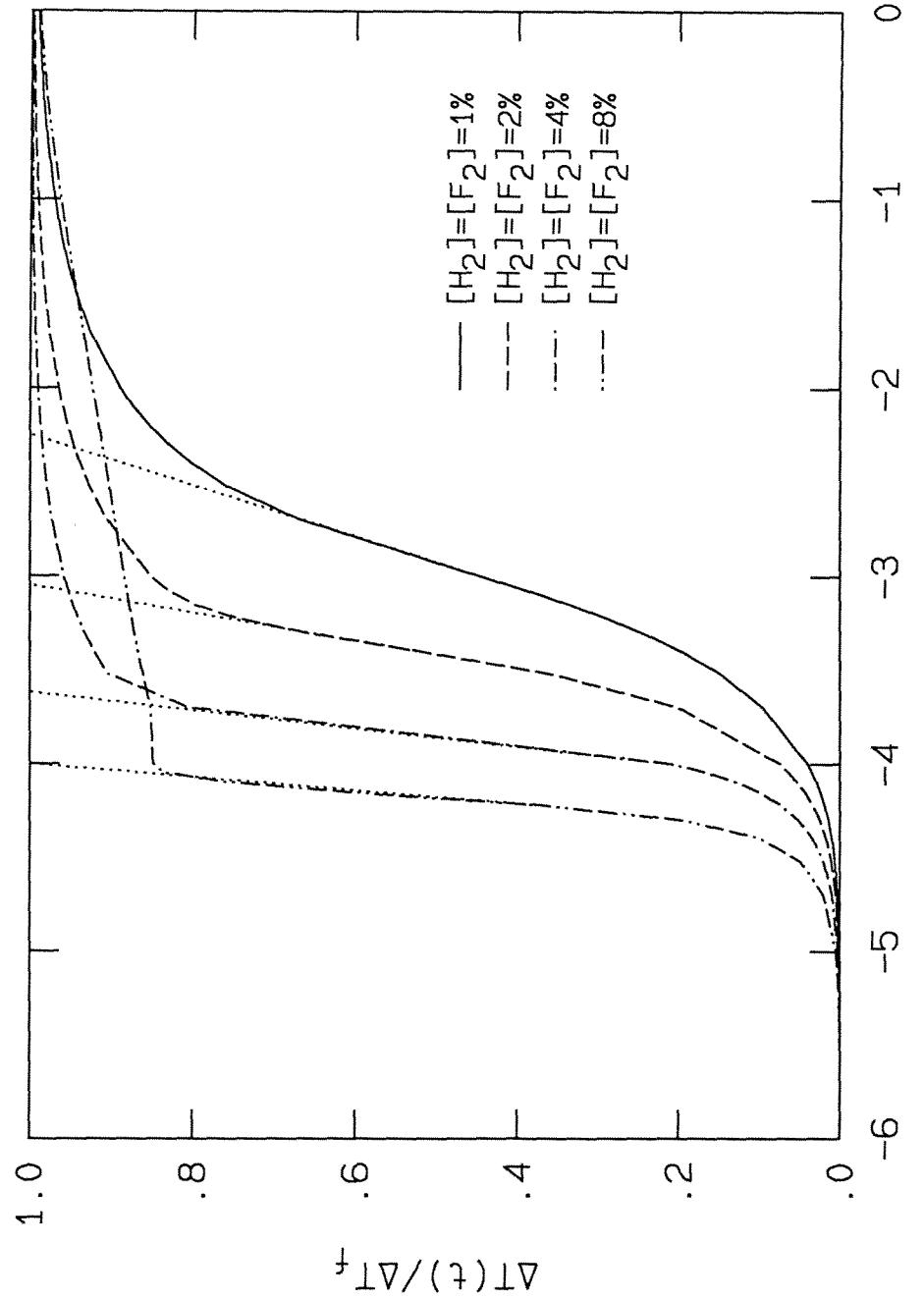

Fig. 2.8: Compressible Flow Kinetics Calculations.
$[H_2]$ and $[F_2]$ variable; $[NO]=0.25\%$, N_2 diluent.
$E_n=1.0$, P=1.0 atm., $T_{1t}=T_{2t}=295$ K.

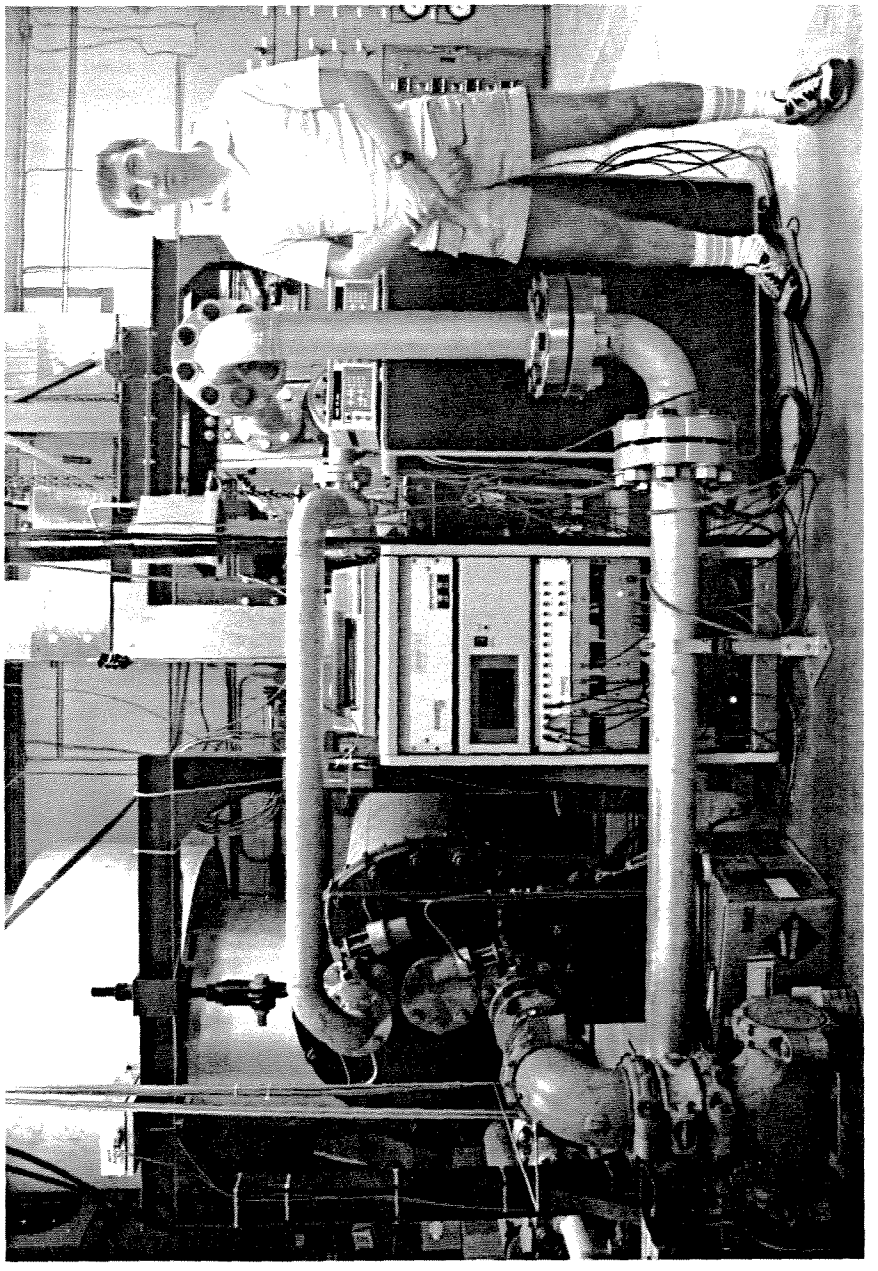

Fig. 3.1 North-Looking View Of Supersonic Hydrogen-Fluorine Reacting Shear Layer Facility.

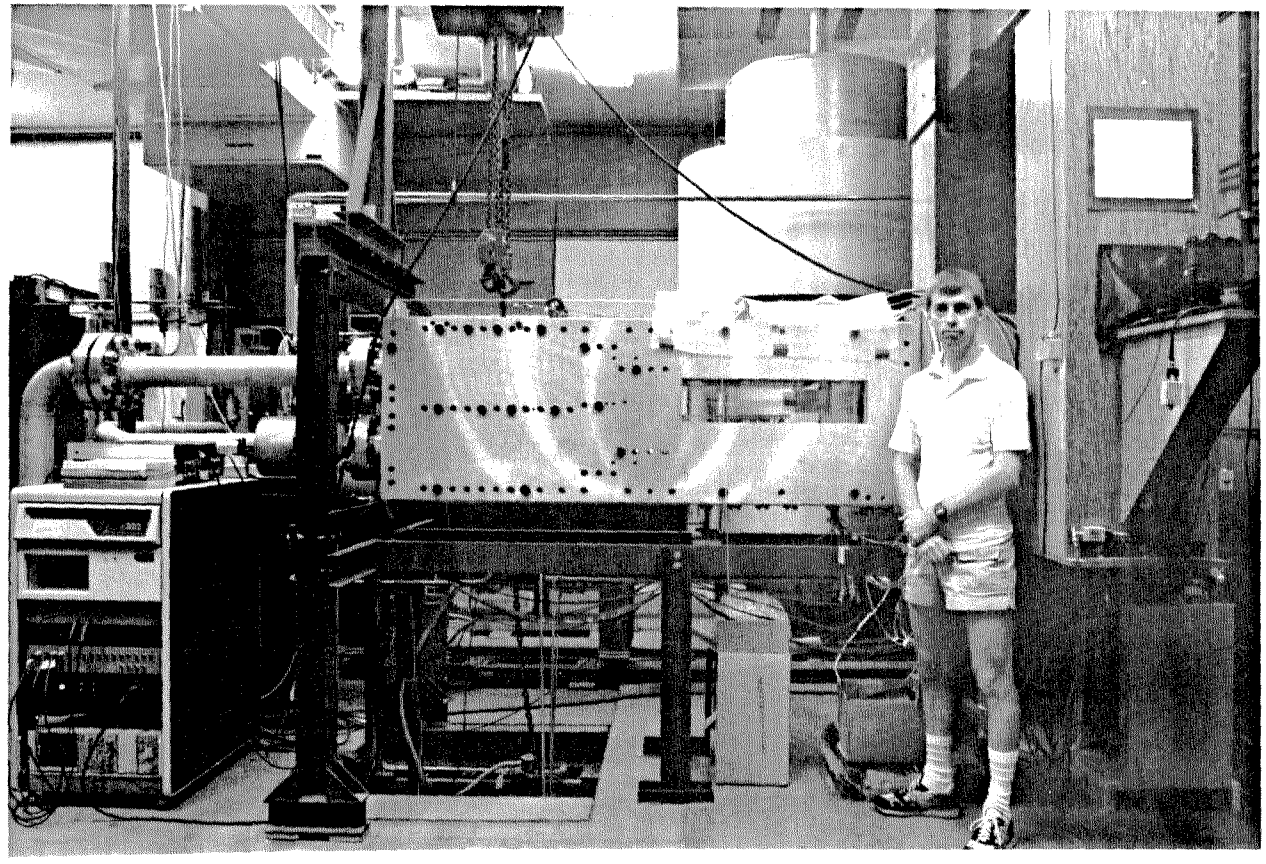

Fig. 3.2 West-Looking View Of Supersonic Hydrogen-Fluorine Reacting Shear Layer Facility.

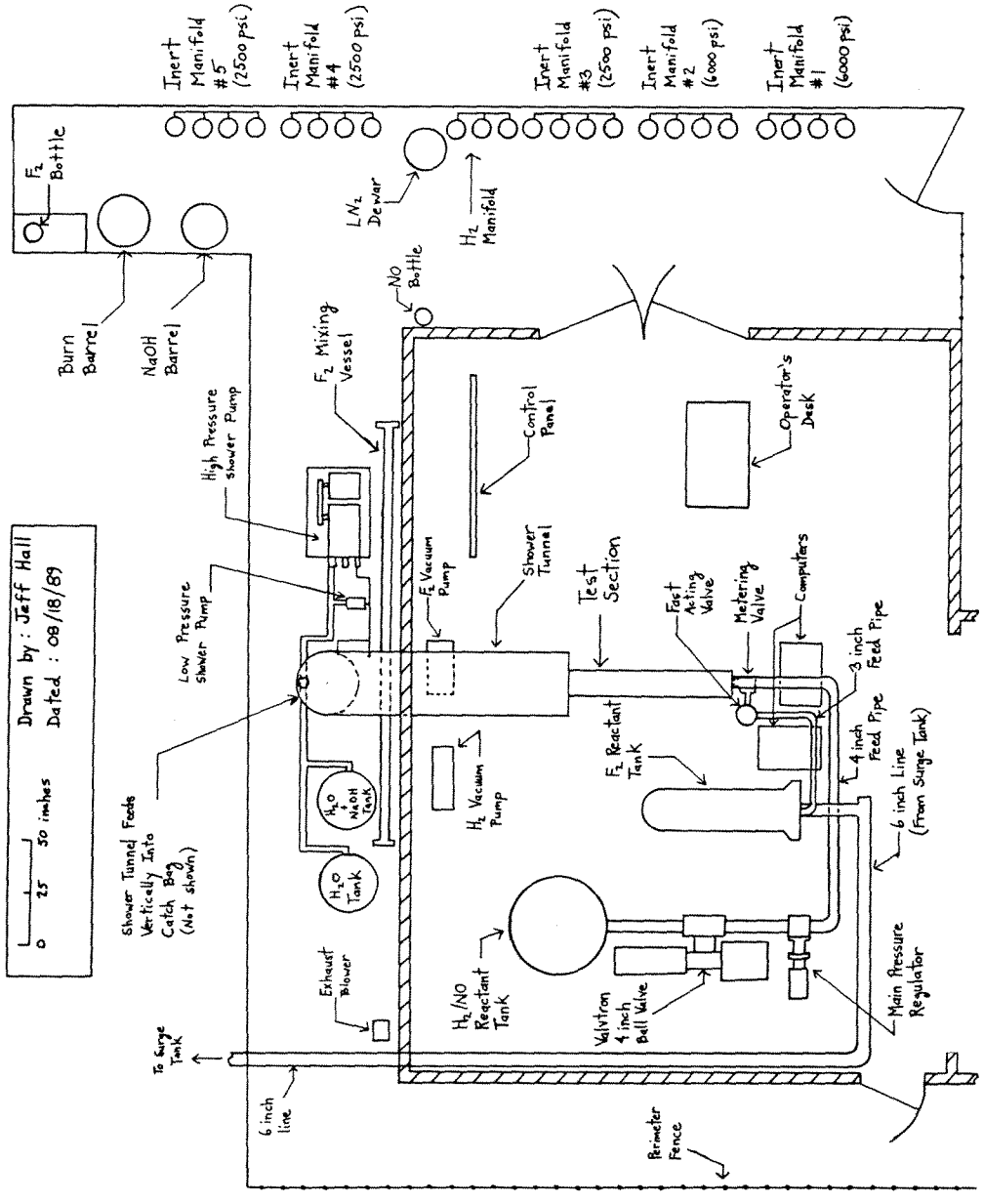

Fig. 3.3: Floor Plan of the Supersonic Hydrogen-Fluorine Combustion Facility.

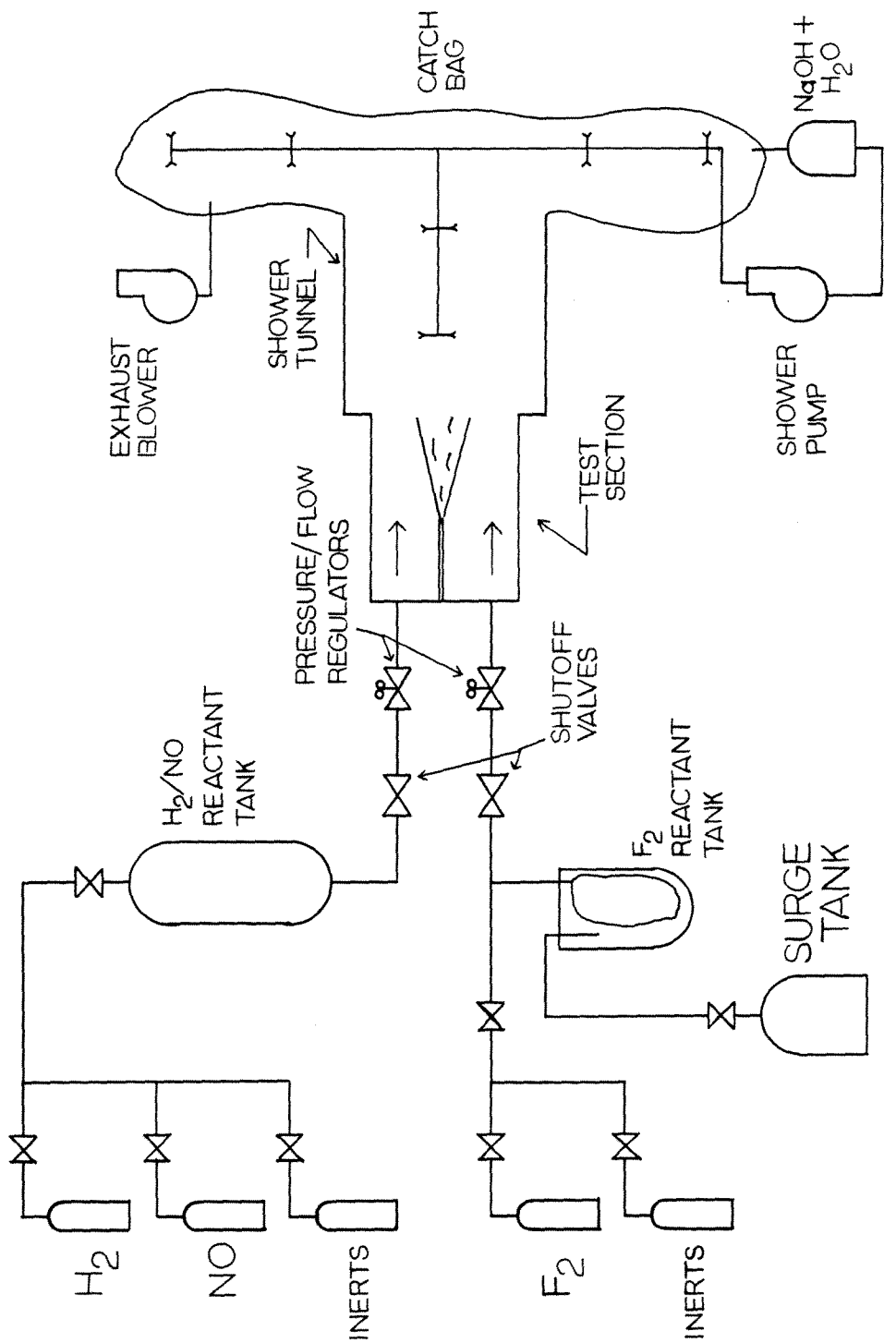

Fig. 3.4: Flow Schematic of the Supersonic Hydrogen-Fluorine Combustion Facility.

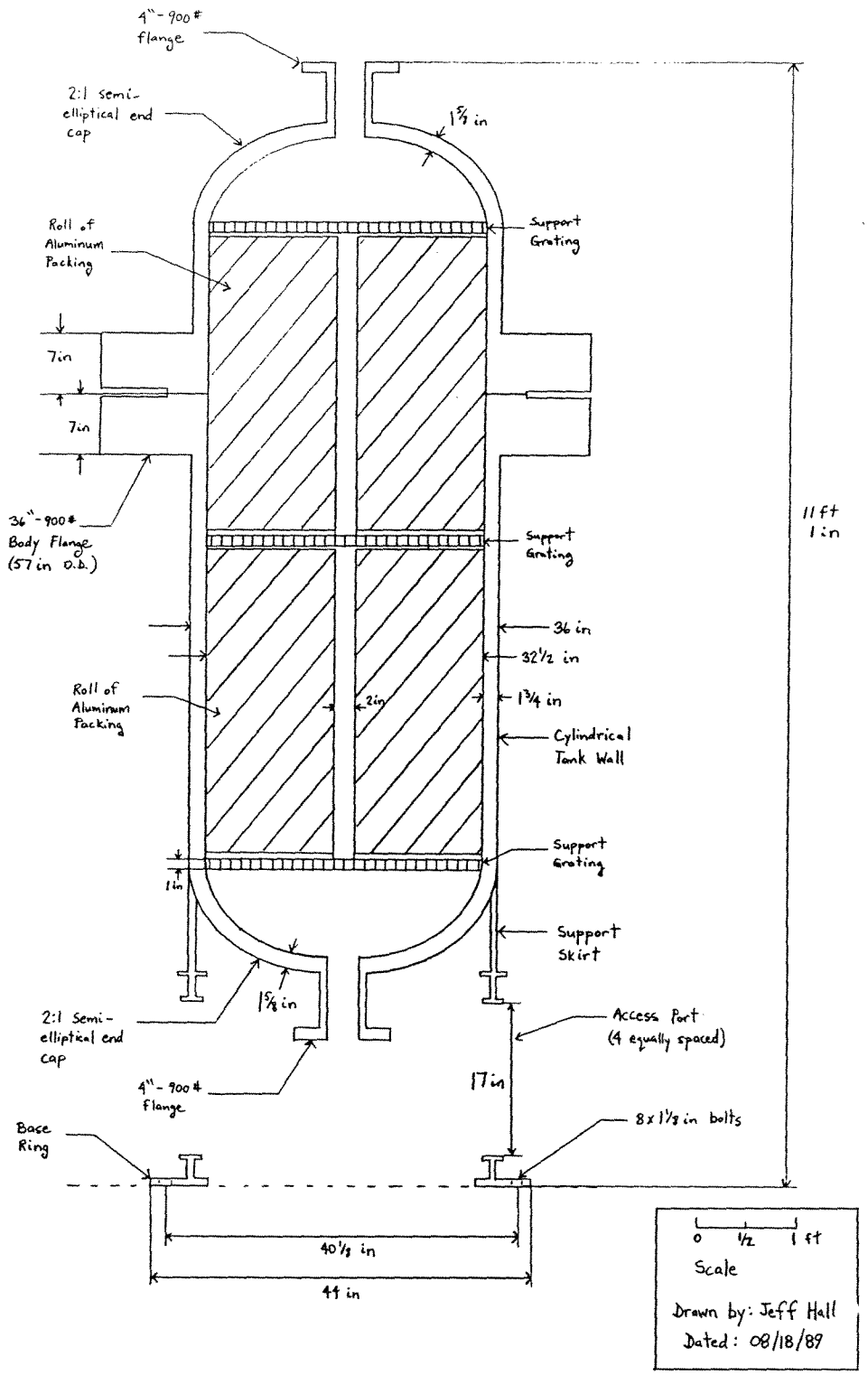

Fig. 3.5: Cut-away Drawing of the H_2/NO Reactant Tank.

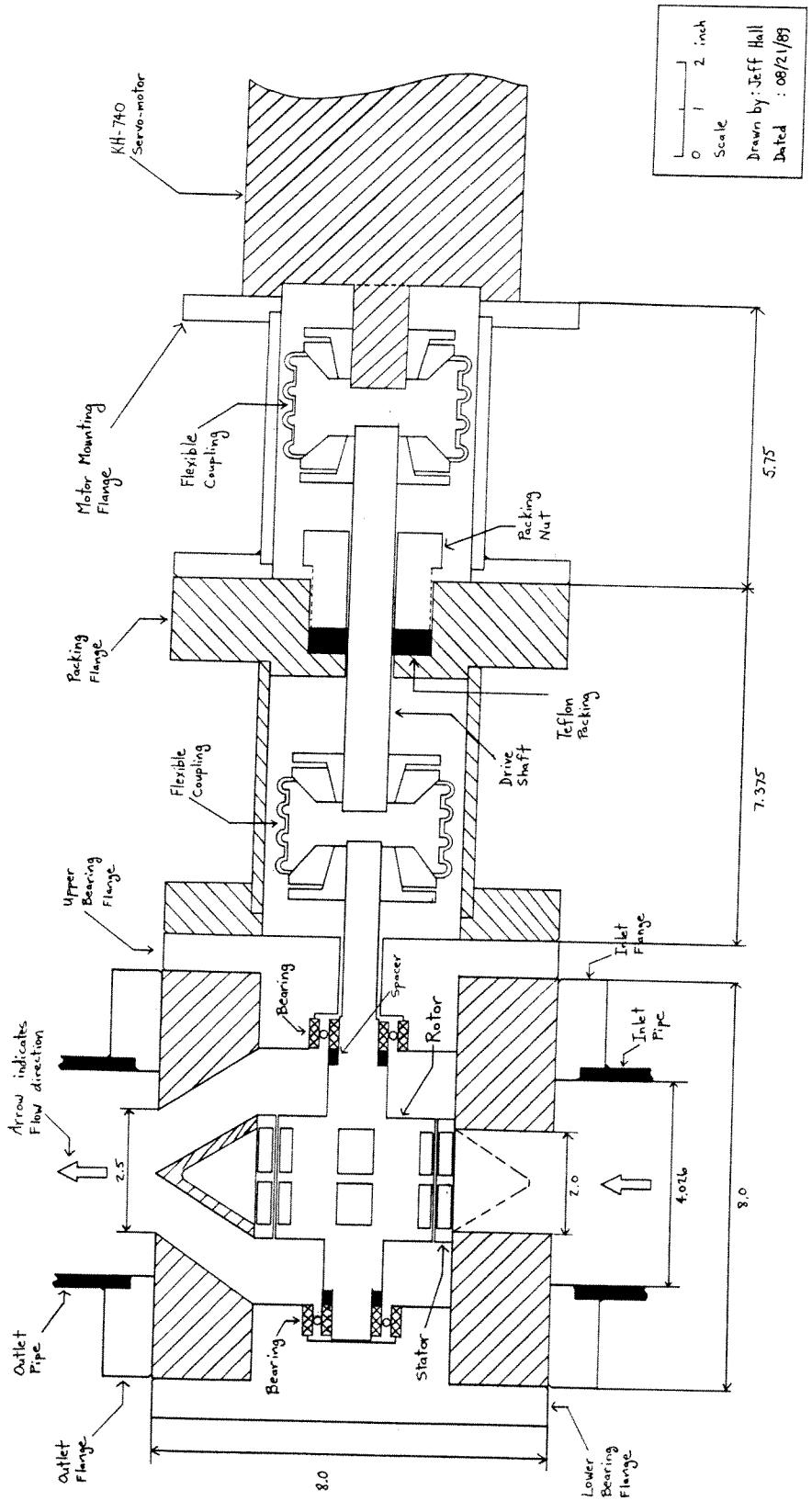

Fig. 3.6: Pressure Regulator/Throttling Valve for High Speed Stream.

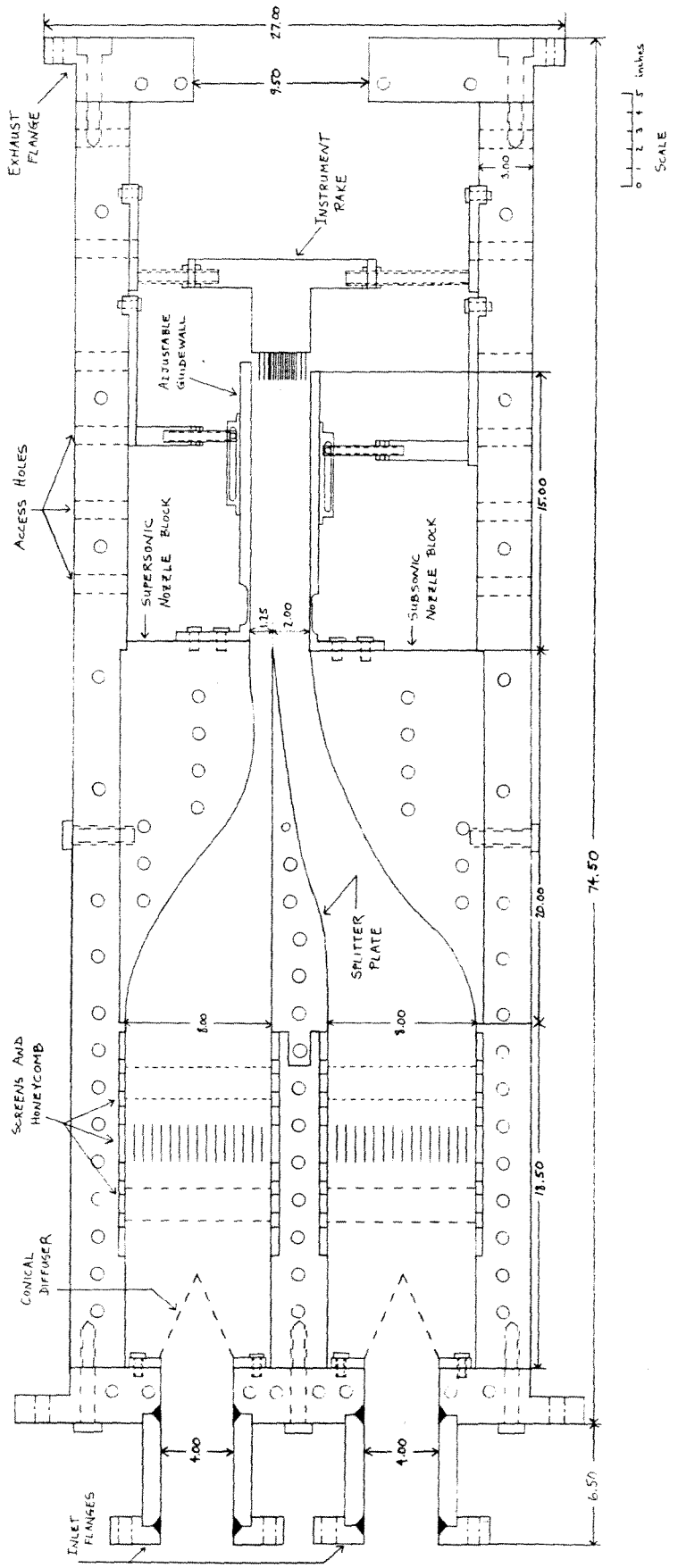

Fig. 3.7: Cut-away Drawing of the Test Section.

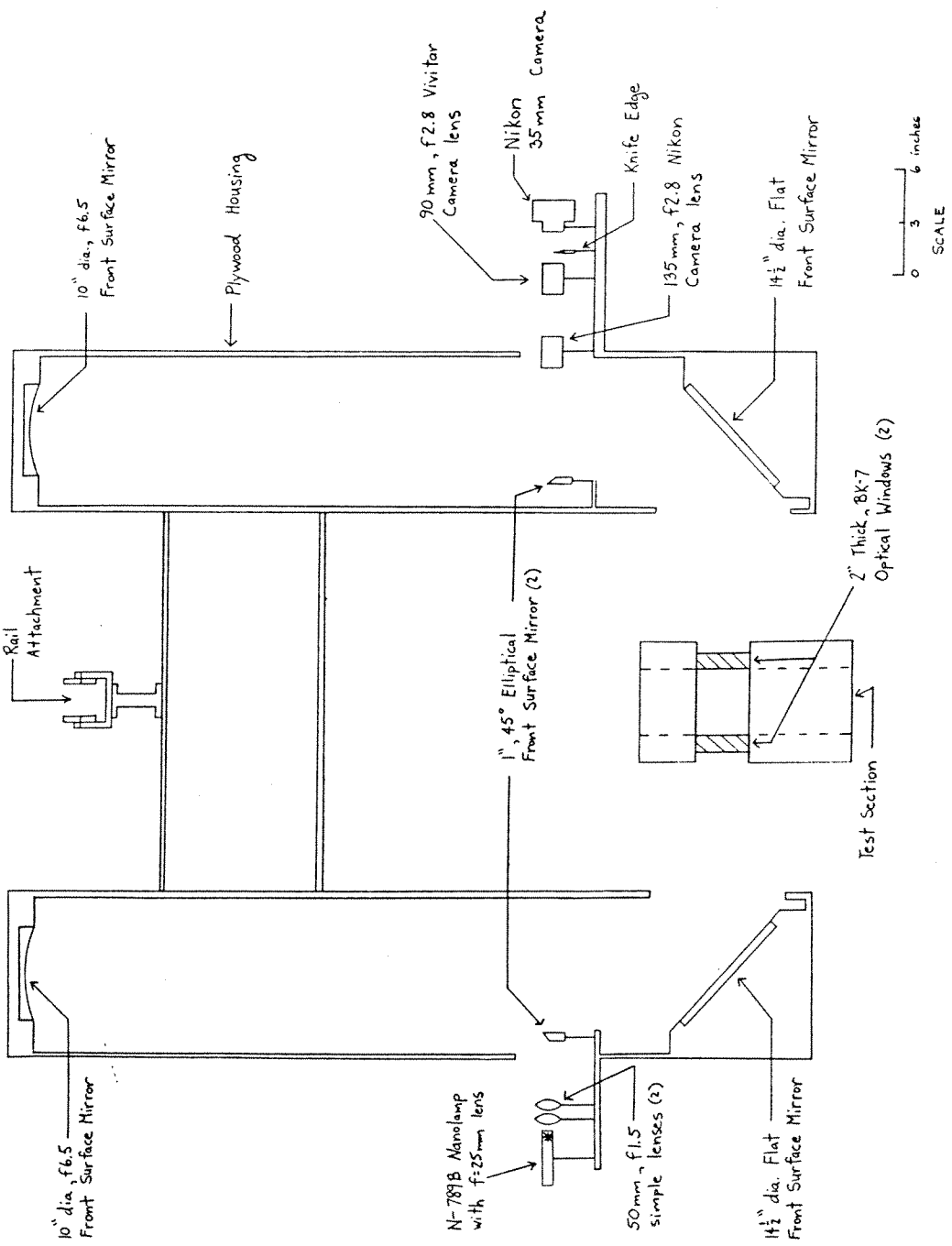

Fig. 3.8: Schematic Drawing of the Schlieren Photography System.

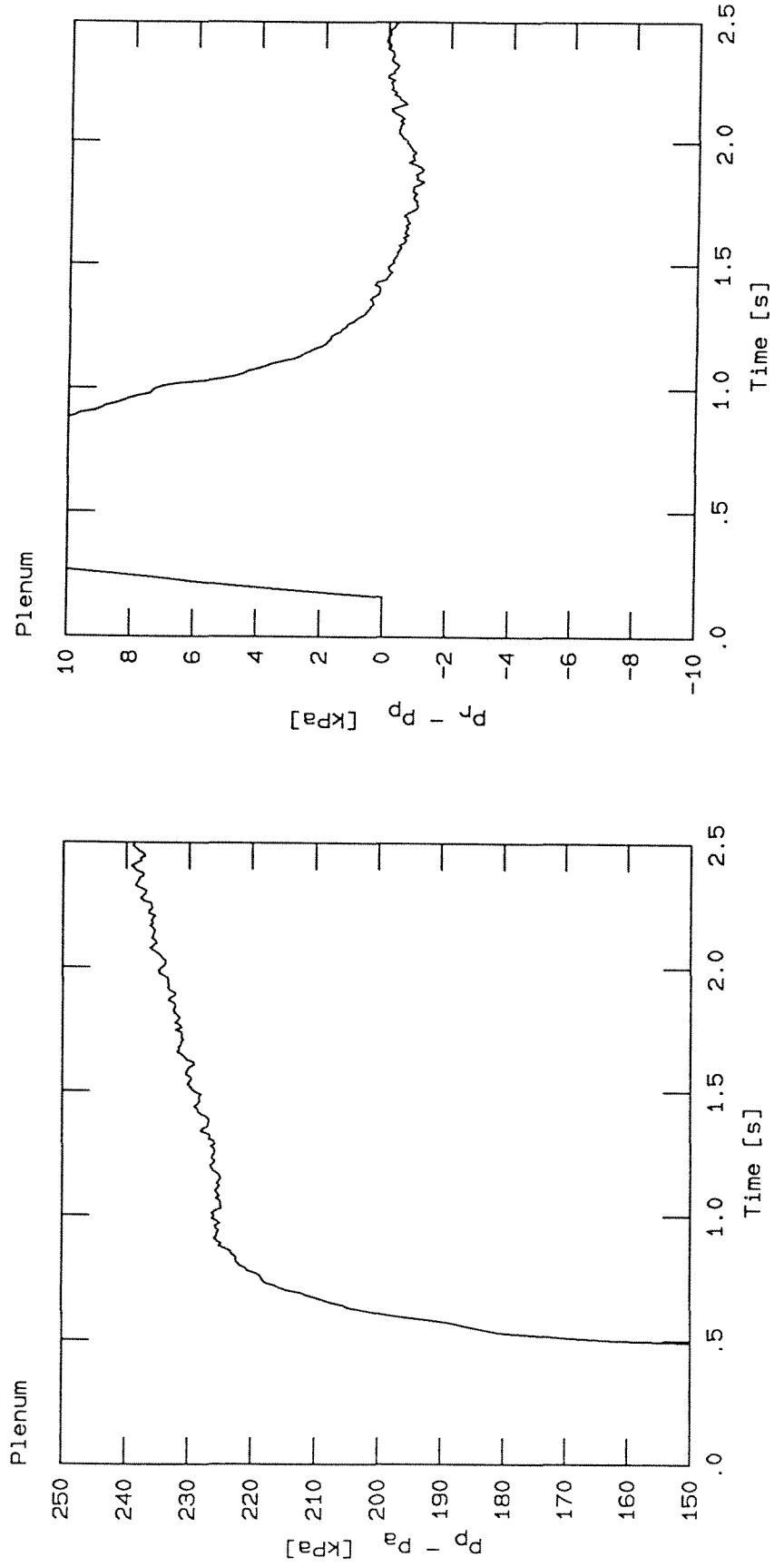

Fig. 4.1: Pressure Time Traces Illustrating Performance Of Feedback Control For N_2 Supersonic Flow.

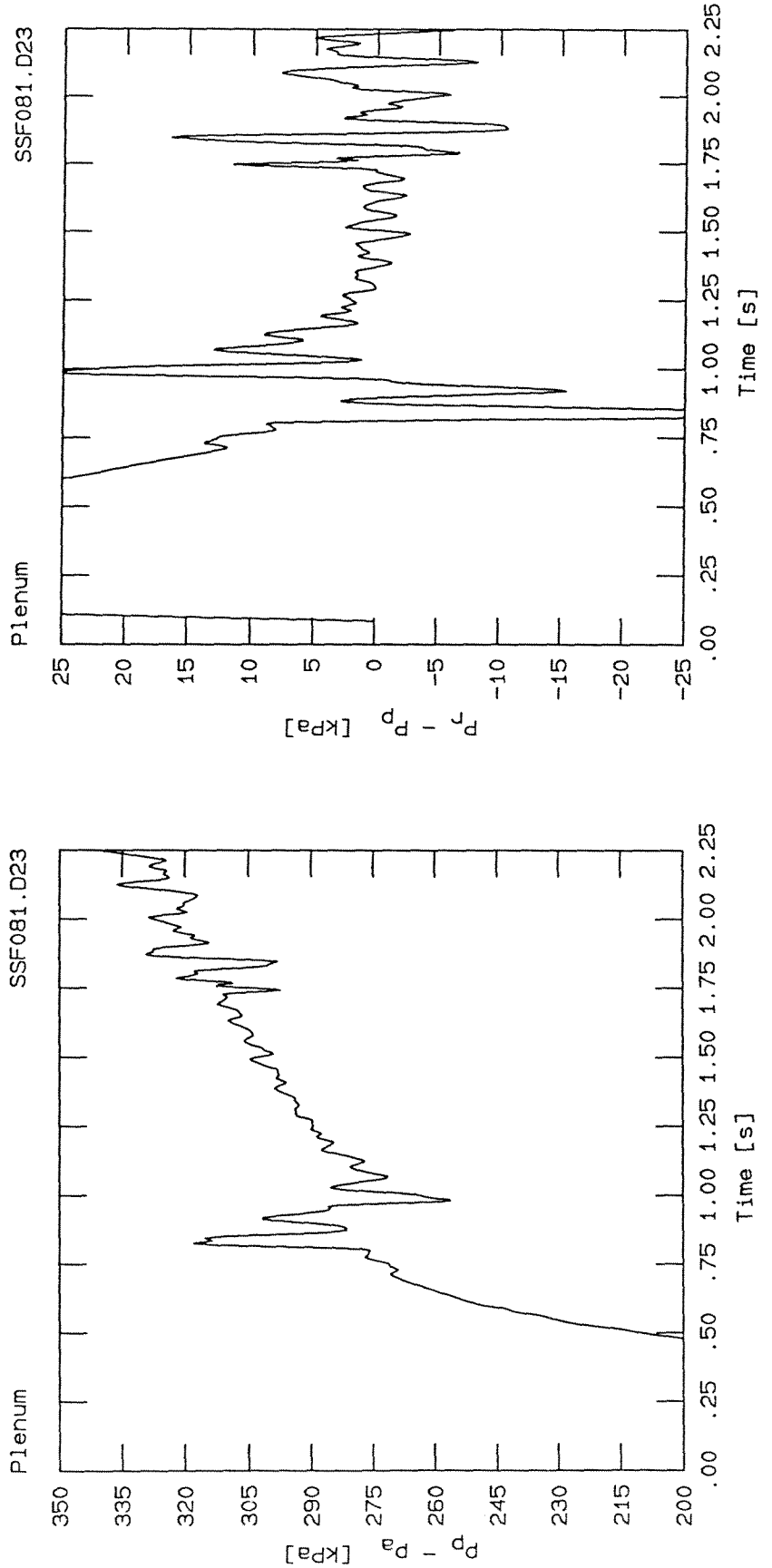

Fig. 4.2: Pressure Time Traces Illustrating Performance Of Feedback Control For He Supersonic Flow.

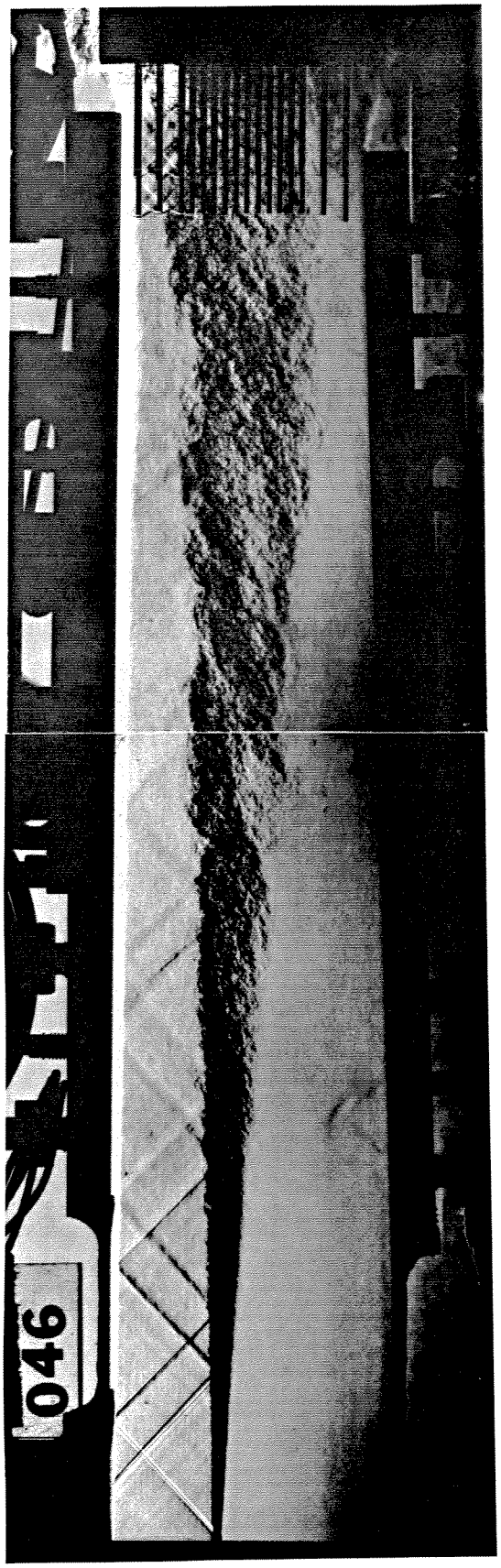

Fig. 4.3: Composite Schlieren Photograph For Case 3 (N_2/N_2 Flow).

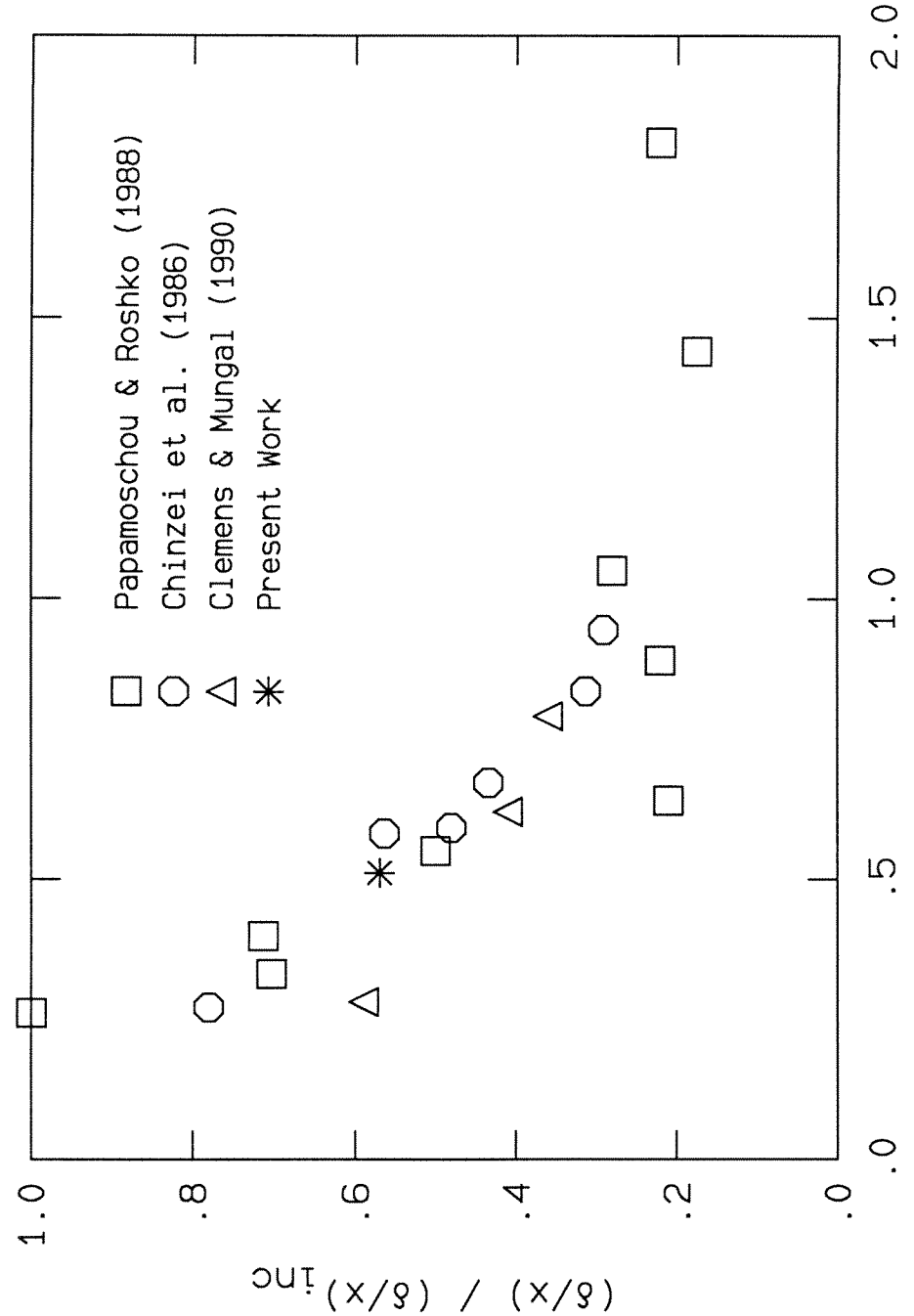

Fig. 4.4: Normalized Growth Rate Of Case 3 Plotted With Other Available Data.

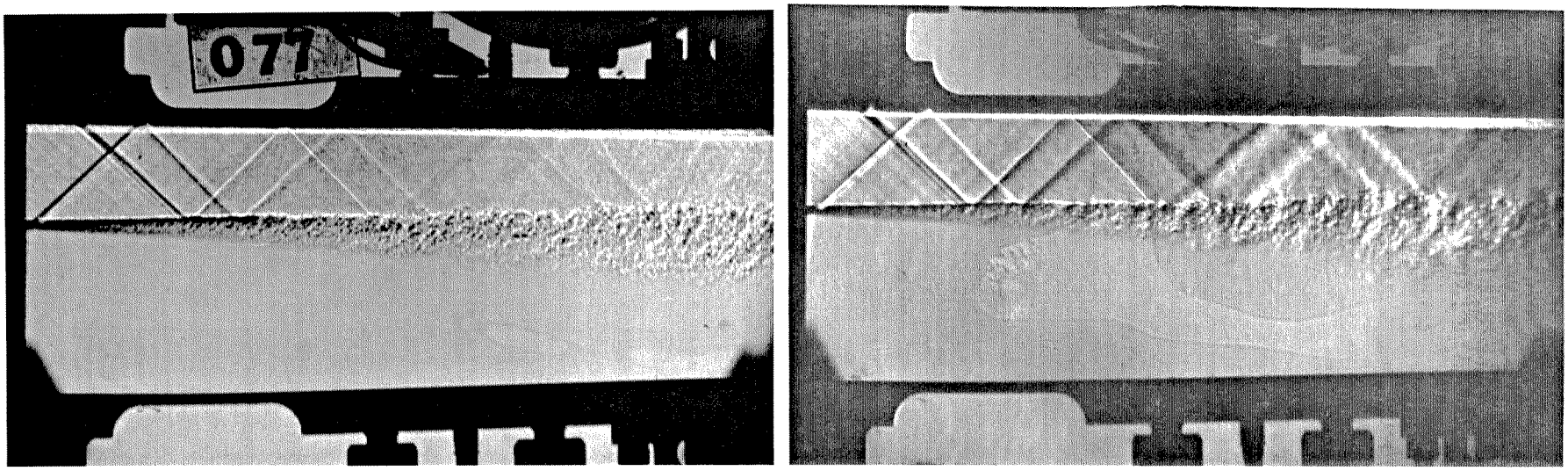

(a) Shadowgraph (b) Vertical Knife Edge Schlieren

Fig. 4.5: Additional Upstream Views Of Case 3 (N_2/N_2) Flow.

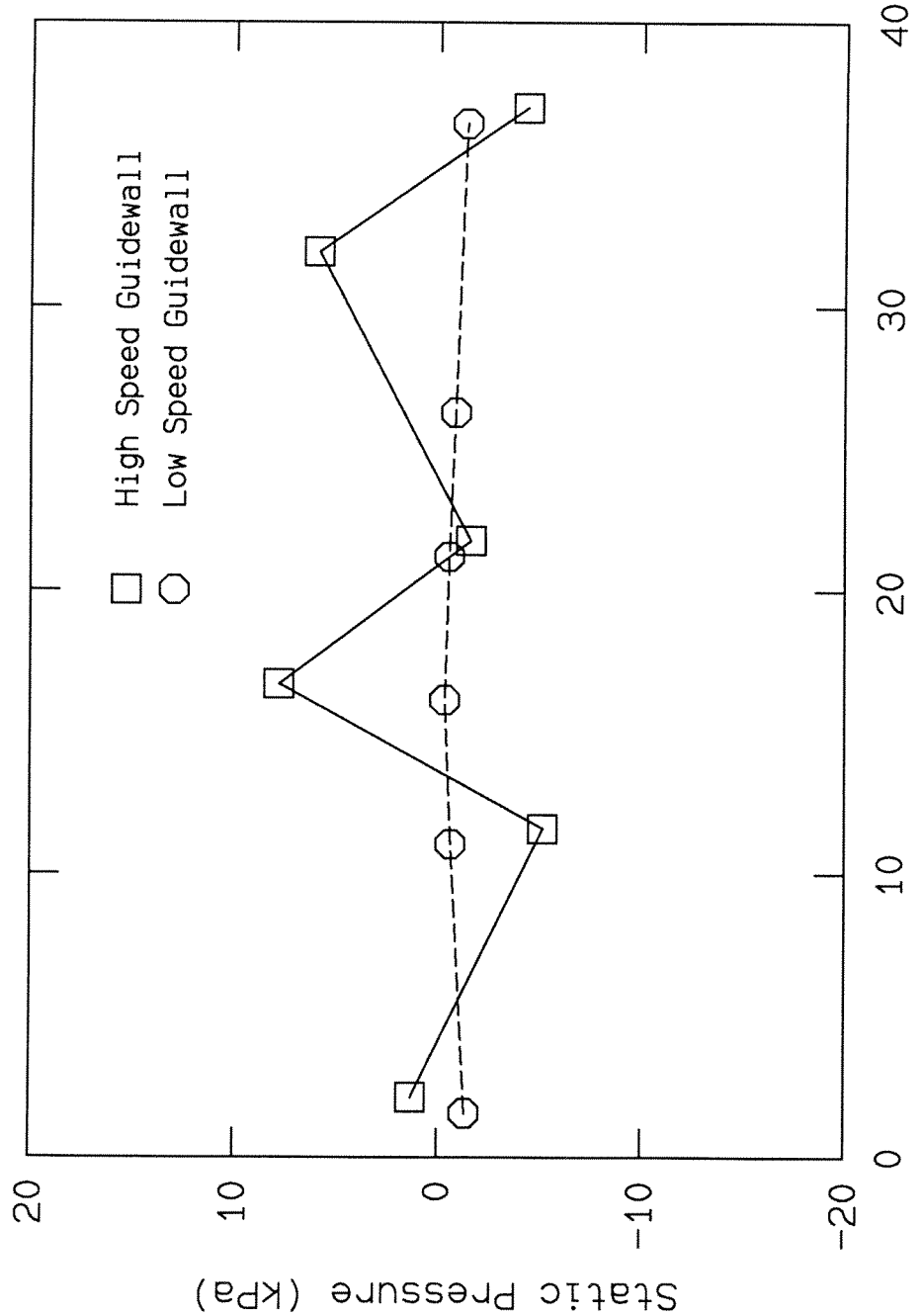

Fig. 4.6: Streamwise Pressure Profiles For Case 3 (N_2/N_2 Flow).

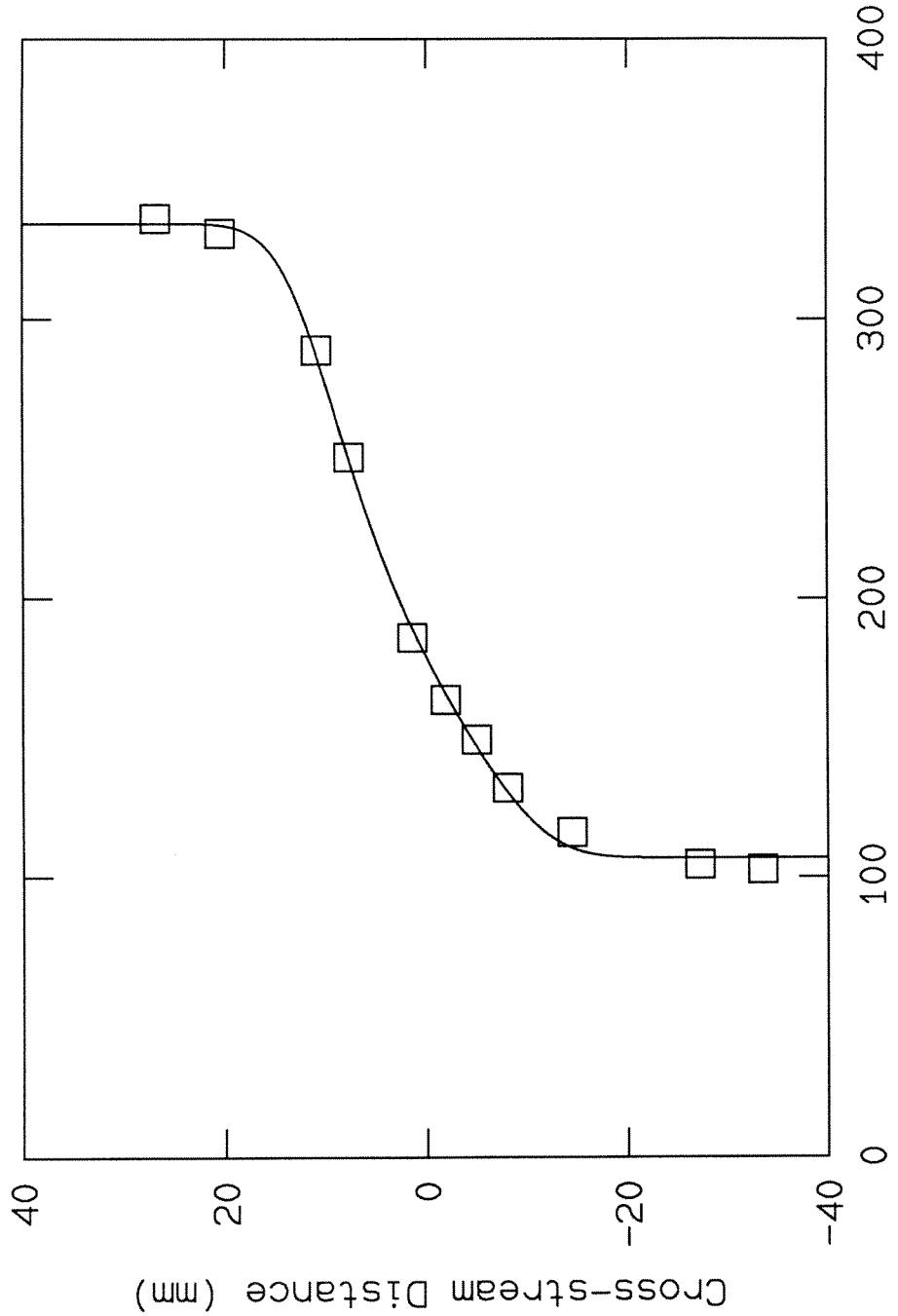

Fig. 4.7: Cross-stream Total Pressure Profile For Case 3 (N_2/N_2 Flow).

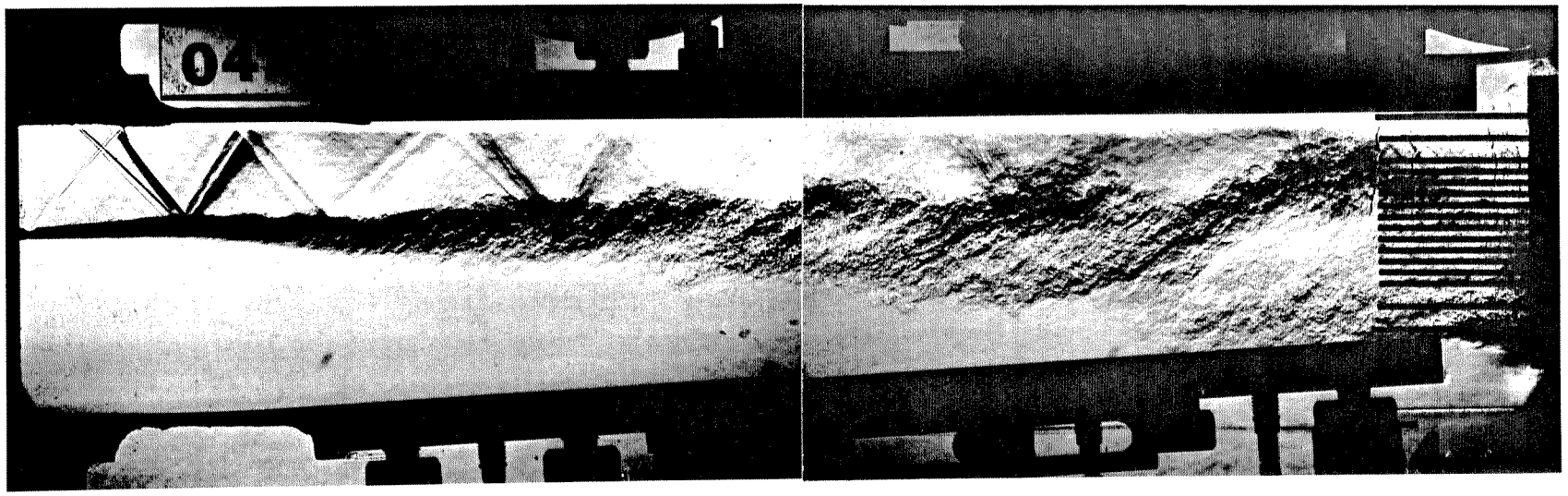

Fig. 4.8: Overexpanded Supersonic Flow Producing Enhanced Two-Dimensional Structure in Case 3 (N_2/N_2) Flow.

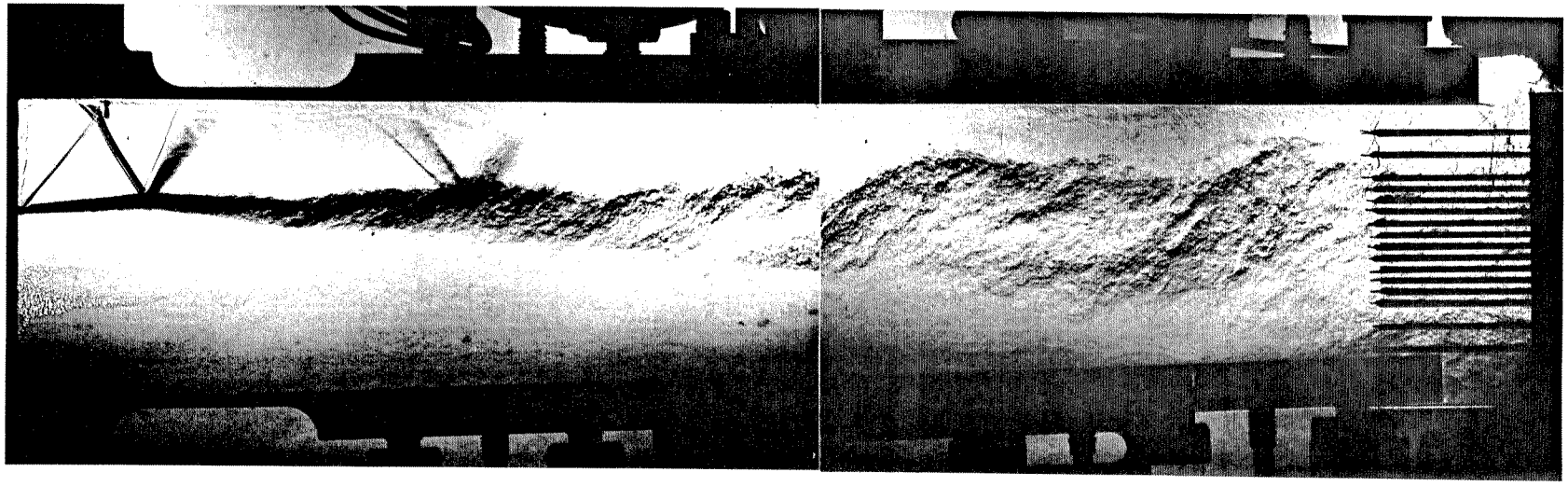

Fig. 4.9 Highly Distorted Shear Layer For Case 3 (N_2/N_2) Flow Illustrating Growth Rate Insensitivity To External Disturbances.

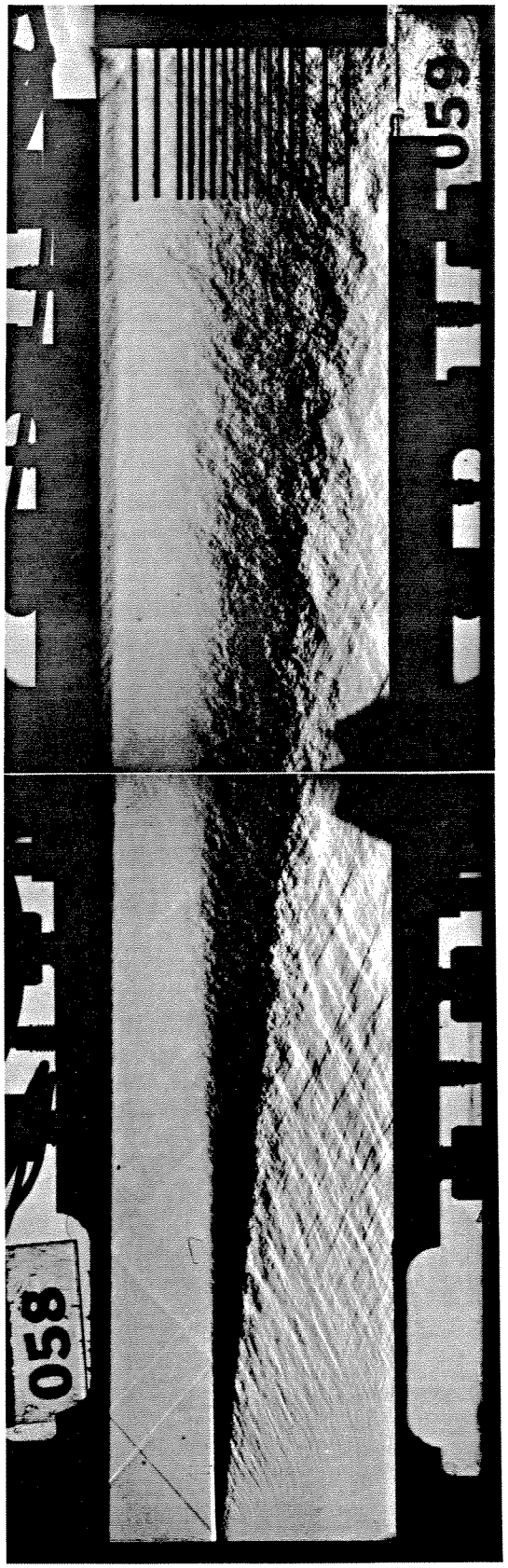

Fig. 4.10: Composite Schlieren Photograph For Case 1 (He/Ar) Flow.

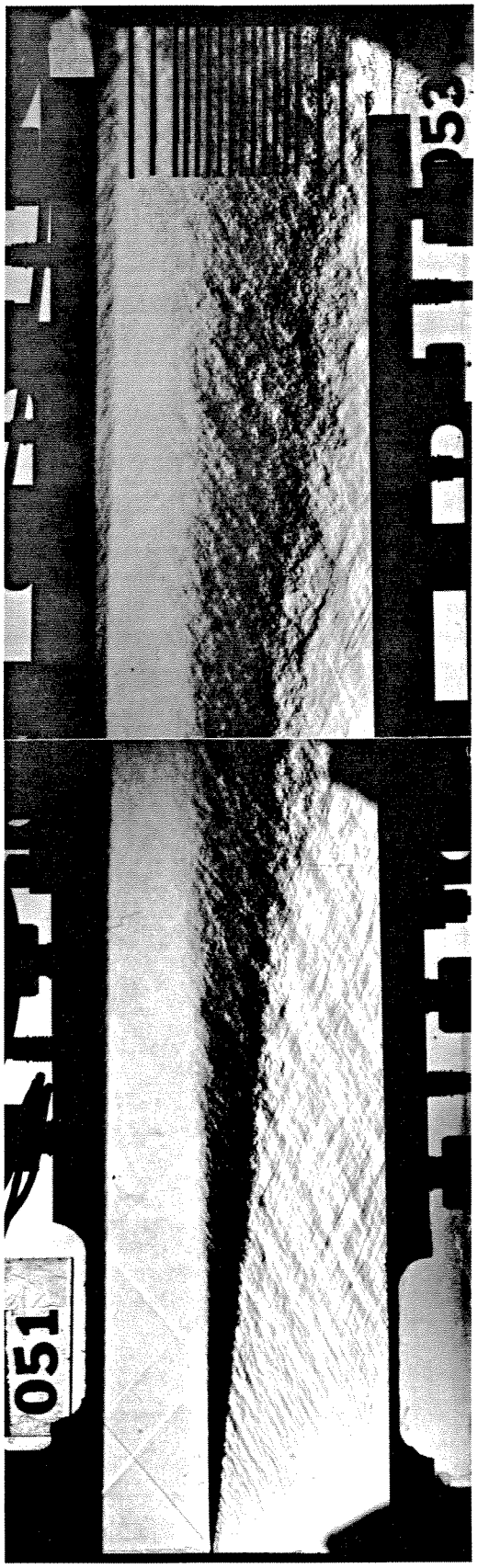

Fig. 4.11: Composite Schlieren Photograph For Case 2 (He/N_2) Flow.

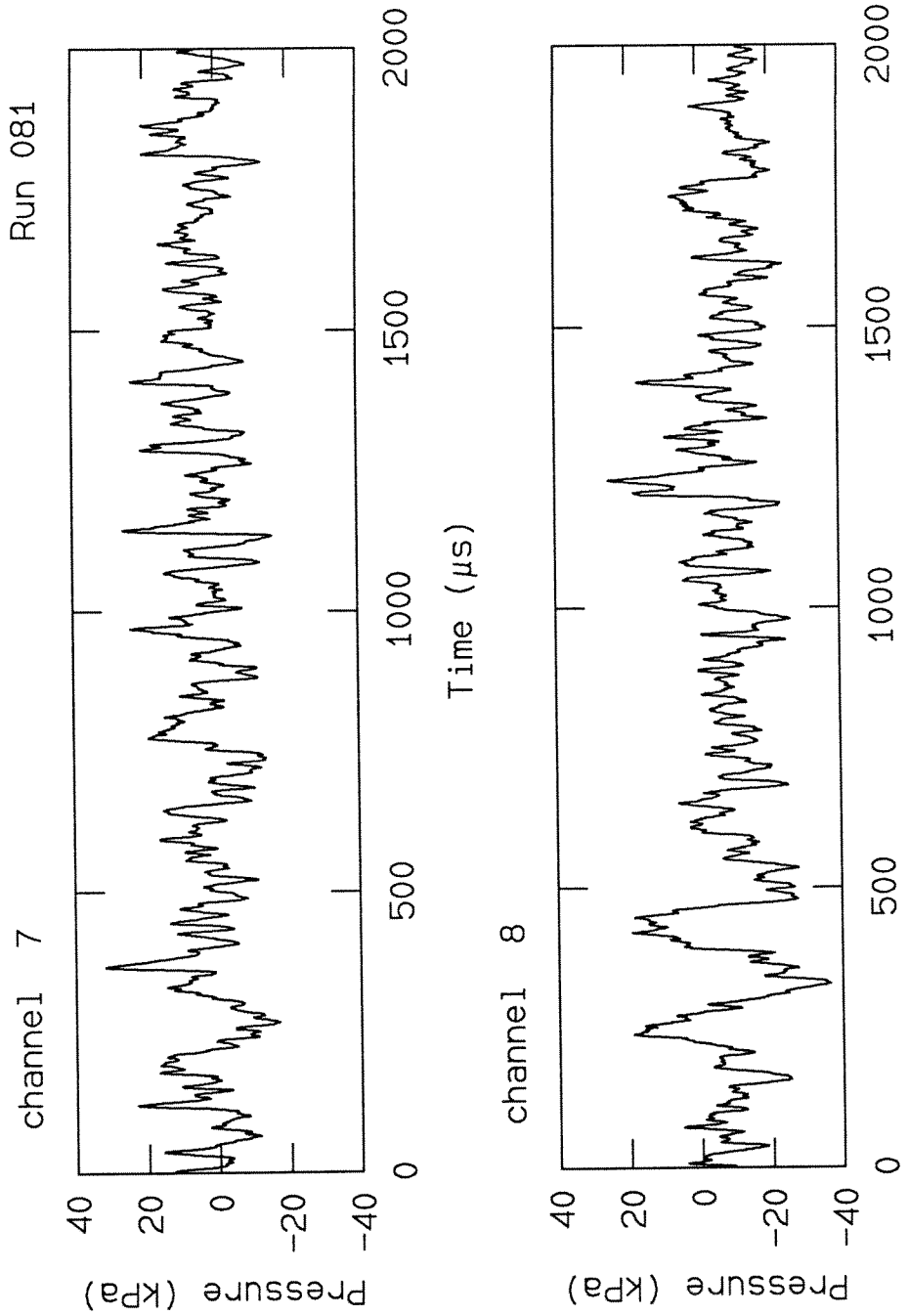

Fig. 4.12: PCB Time Traces For Case 2

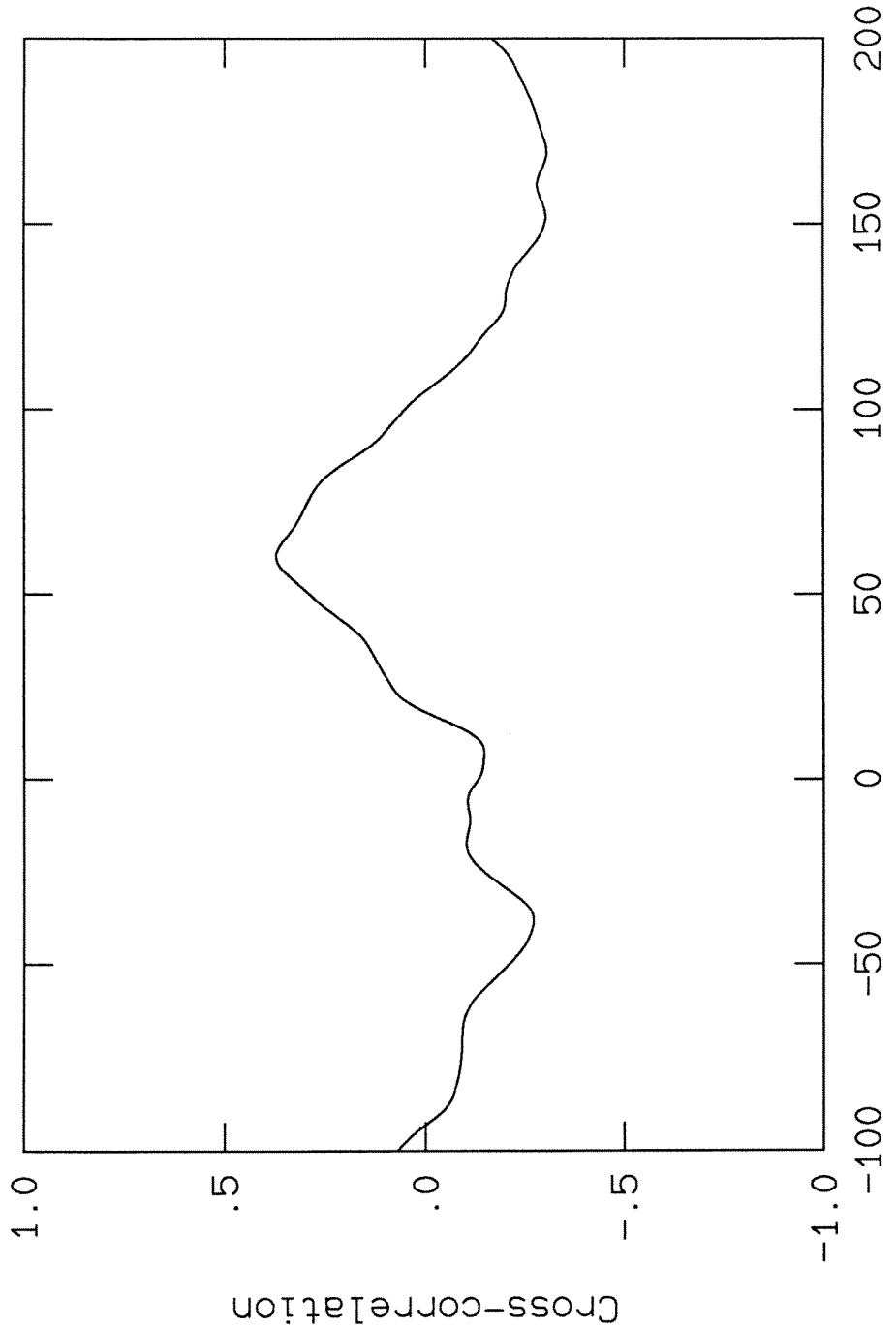

Fig. 4.13: Cross-correlation Of Guidewall Pressure Transducers For Case 2 (He/N_2) Flow.

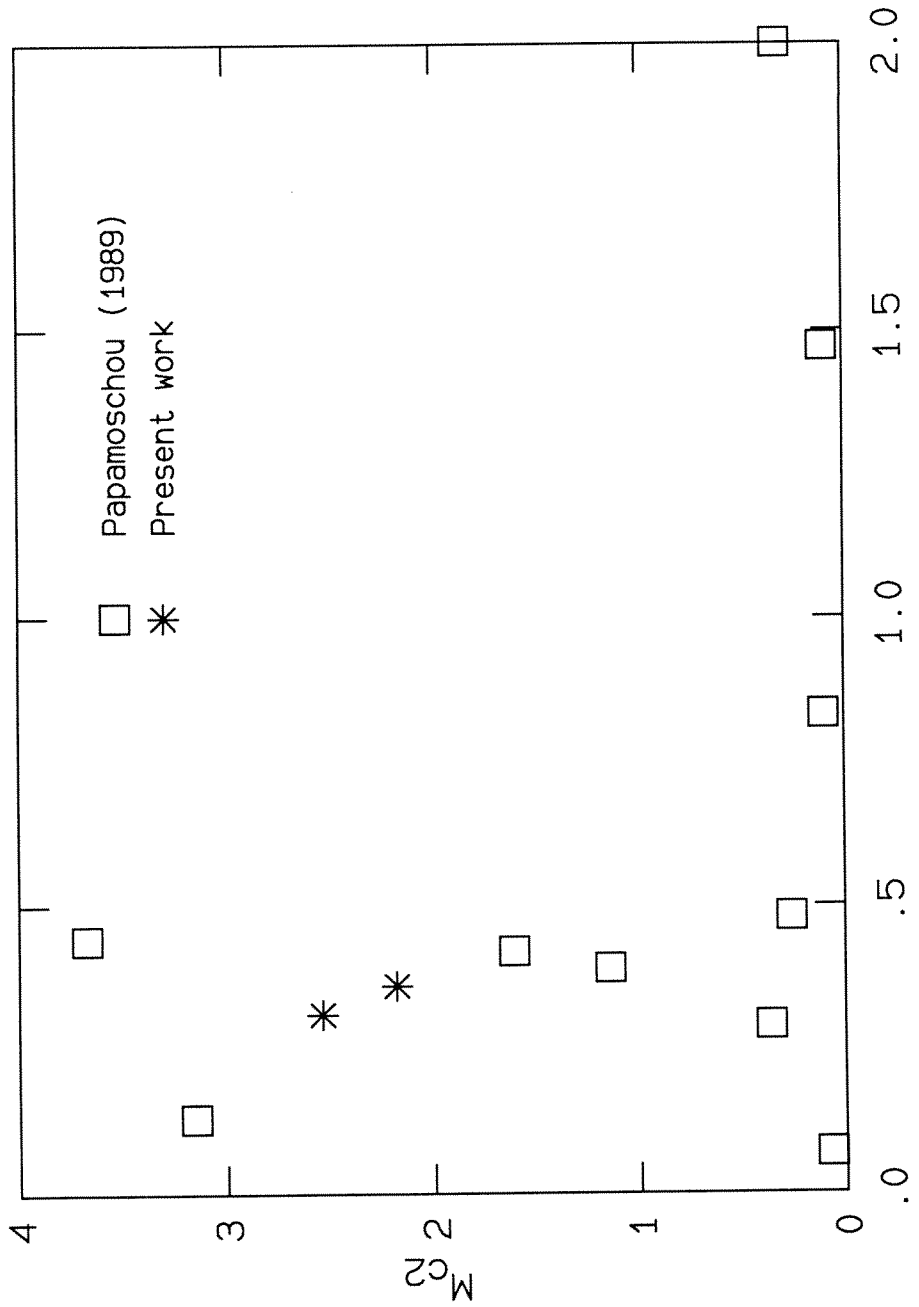

Fig. 4.14: Convective Mach Numbers Measured for Cases 1 and 2 plotted with Papamoschou (1989).

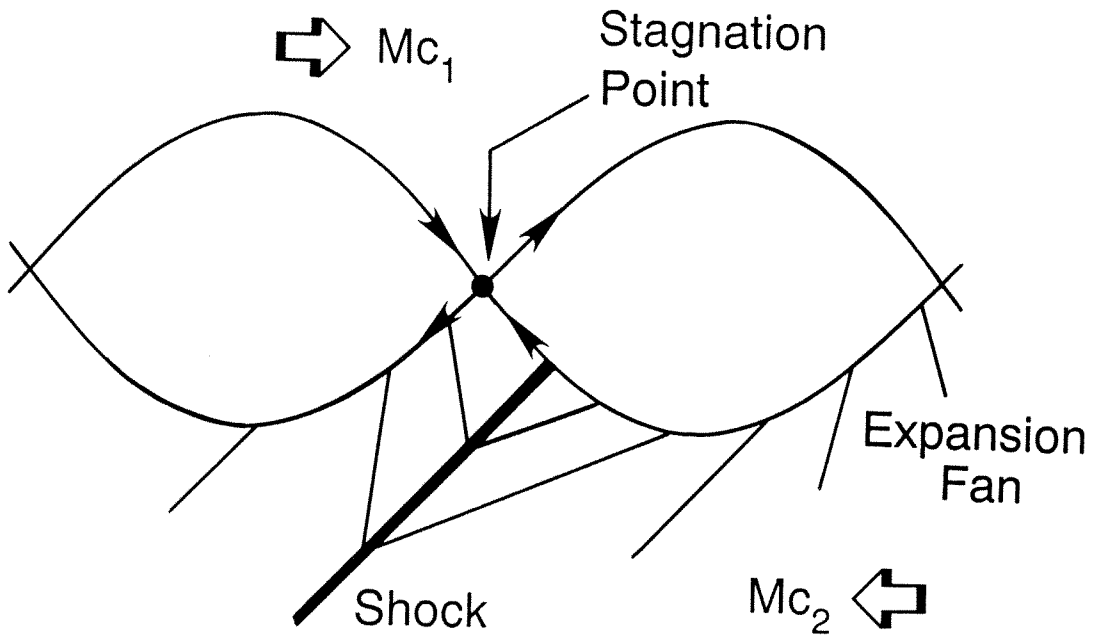

Fig. 4.15: Model For Shear Layer Recompression Shock (Papamoschou 1989).

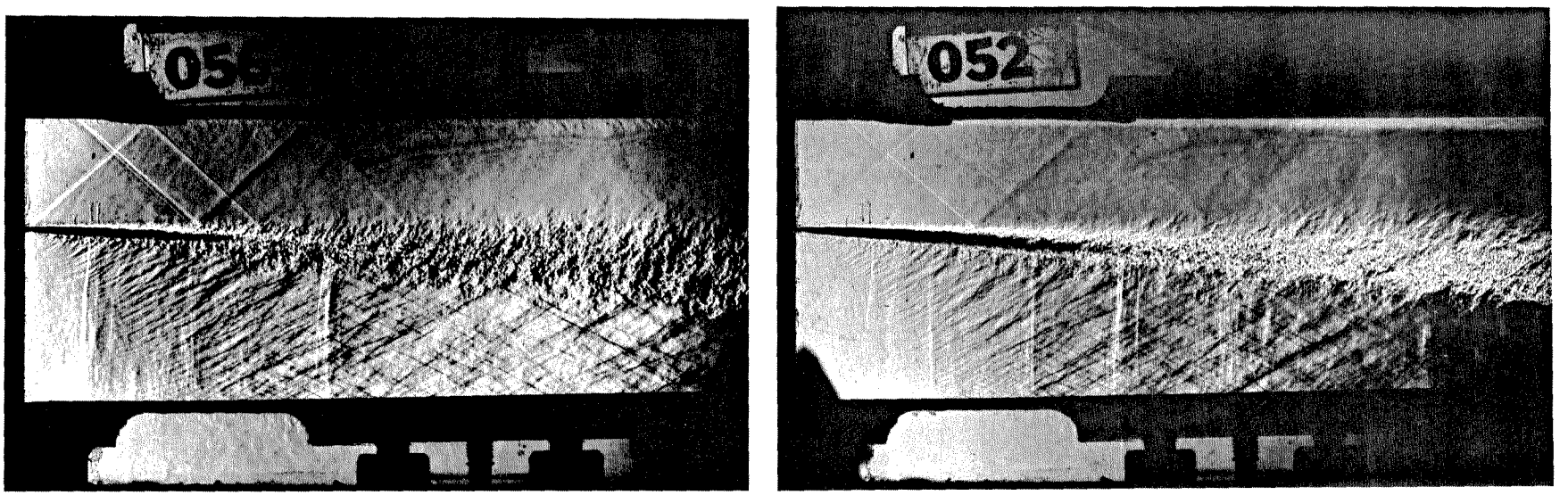

(a) Case 1

(b) Case 2

Fig. 4.16: Vertical Knife-Edge Schlieren Photographs Of Upstream Region For Cases 1 and 2.

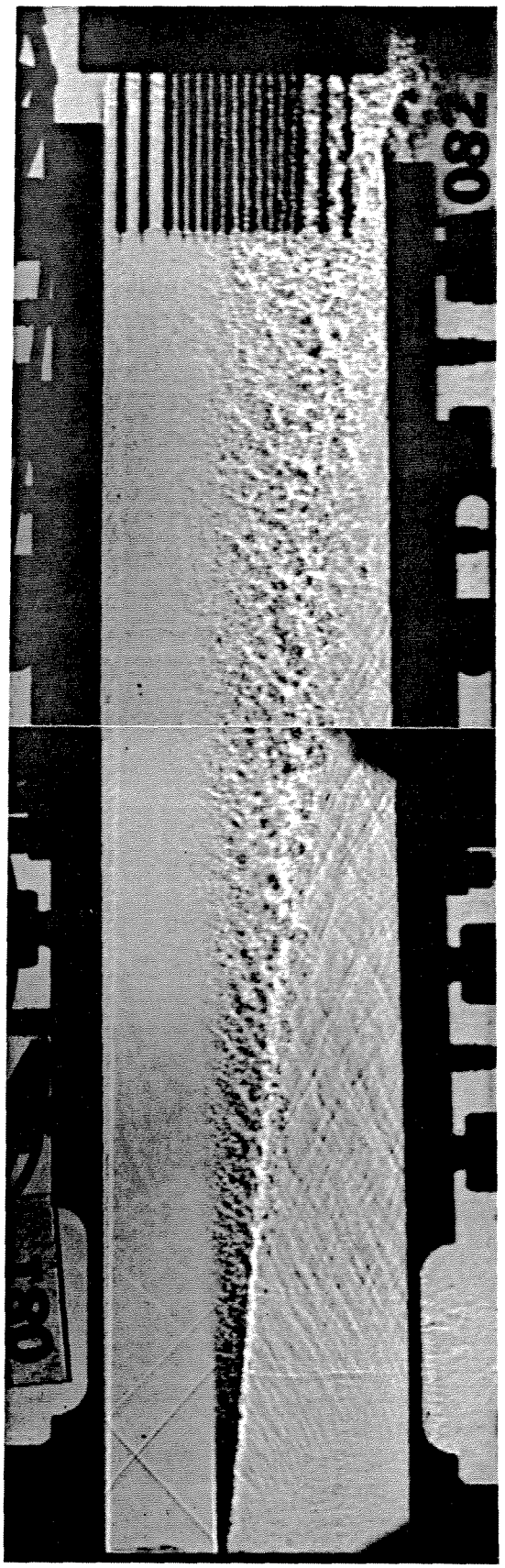

Fig. 4.17: Composite Shadowgraph Photograph For Case 2 (He/N_2) Flow.

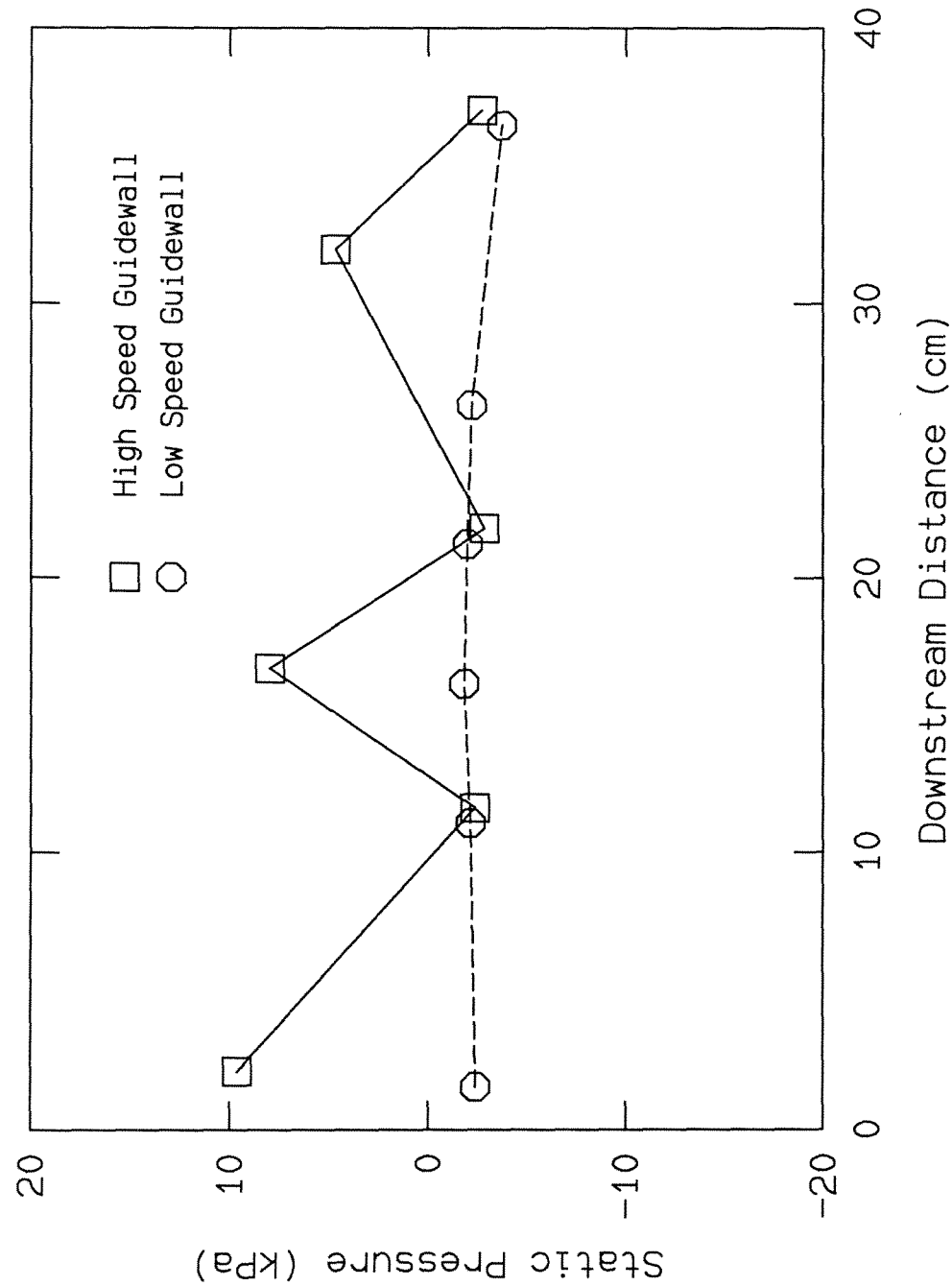

Fig. 4.18: Streamwise Pressure Profiles
For Case 1 (He/Ar) Flow.

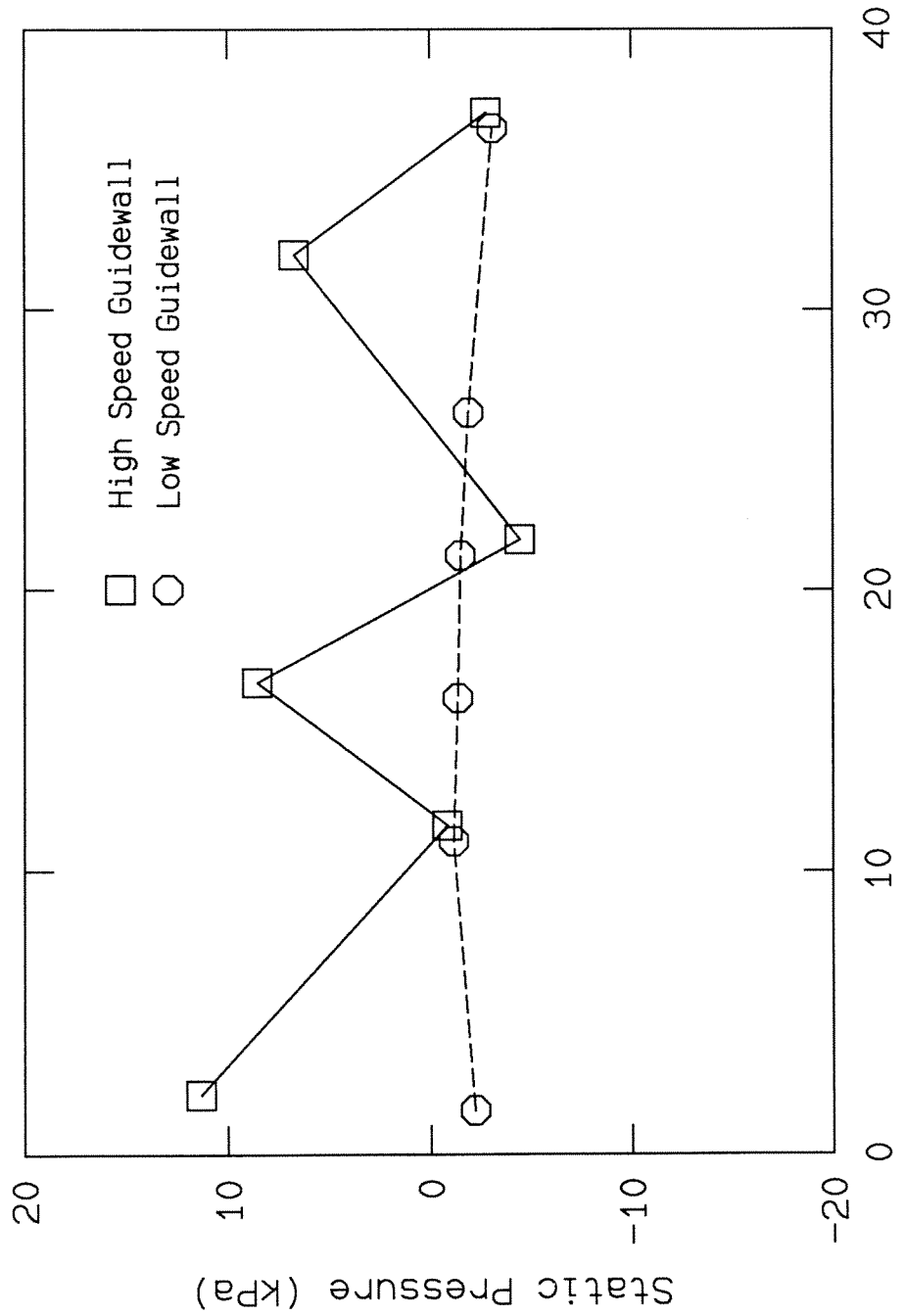

Fig. 4.19: Streamwise Pressure Profiles For Case 2 (He/N_2) Flow.

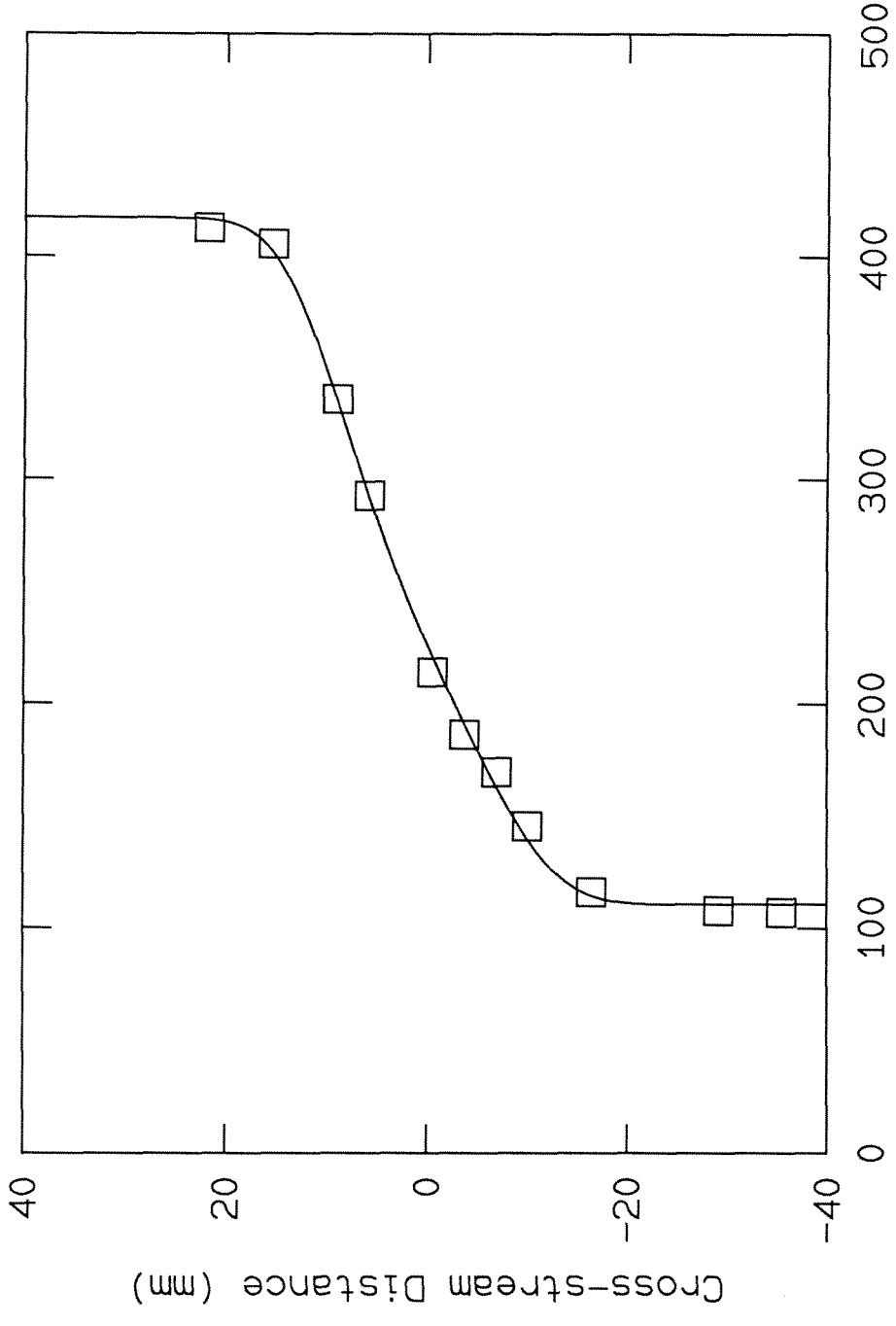

Fig. 4.20: Cross-stream Total Pressure Profile
For Case 1 (He/Ar) Flow.

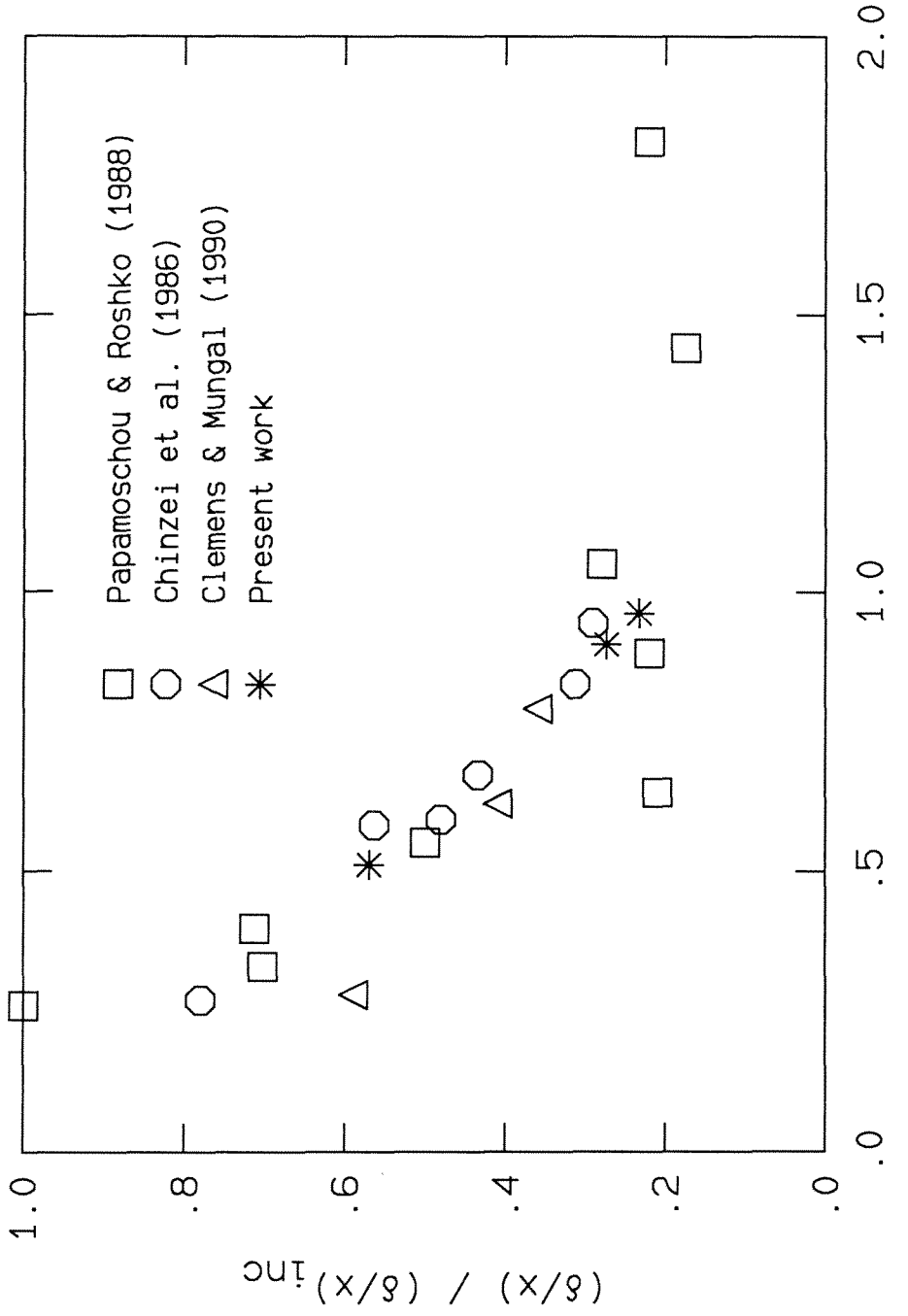

Fig. 4.21: Normalized Growth Rate Of Cases 1-3 Plotted With Other Available Data.

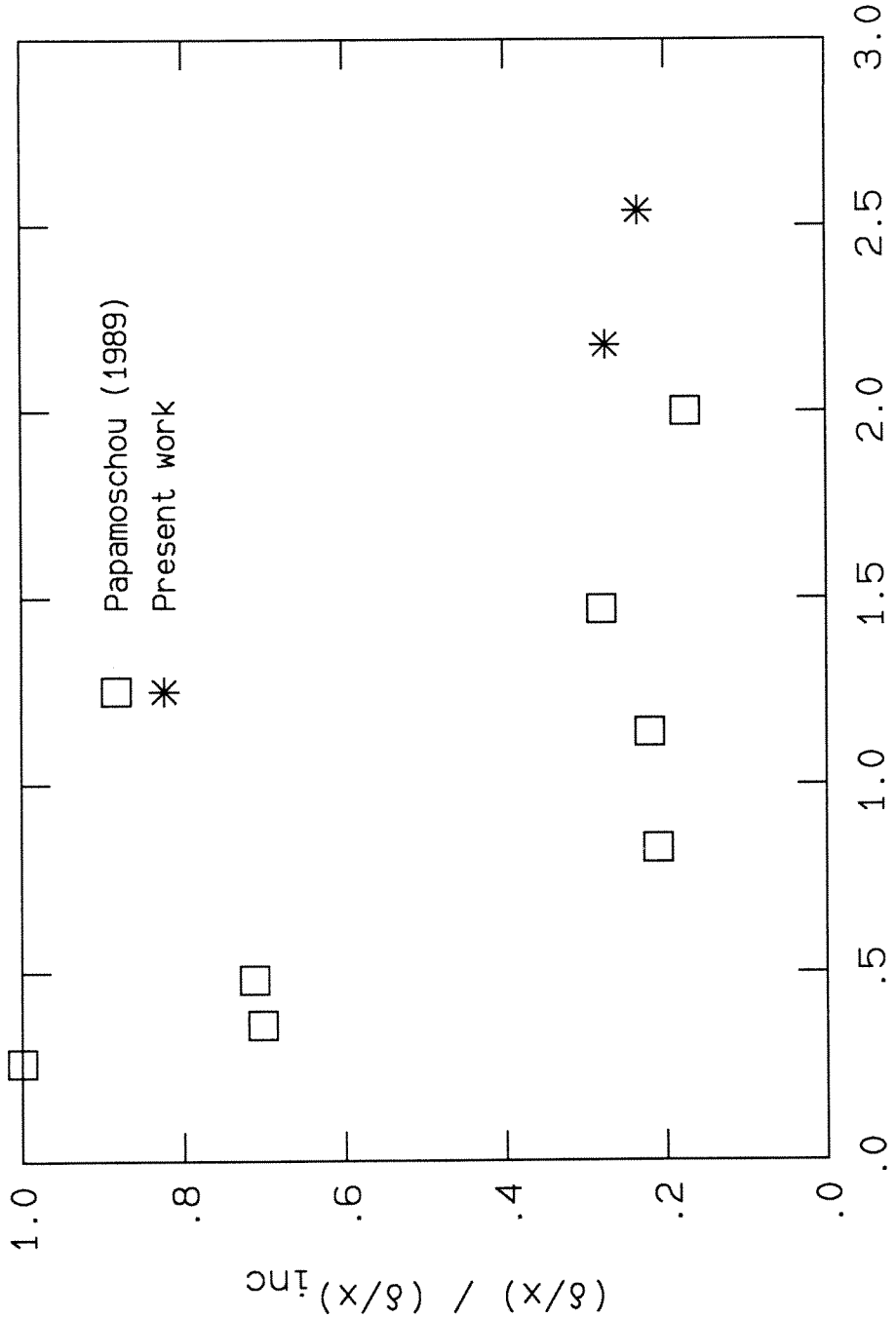

Fig. 4.22: Normalized Growth Rate Of Cases 1 and 2 Plotted With Other Available Data.

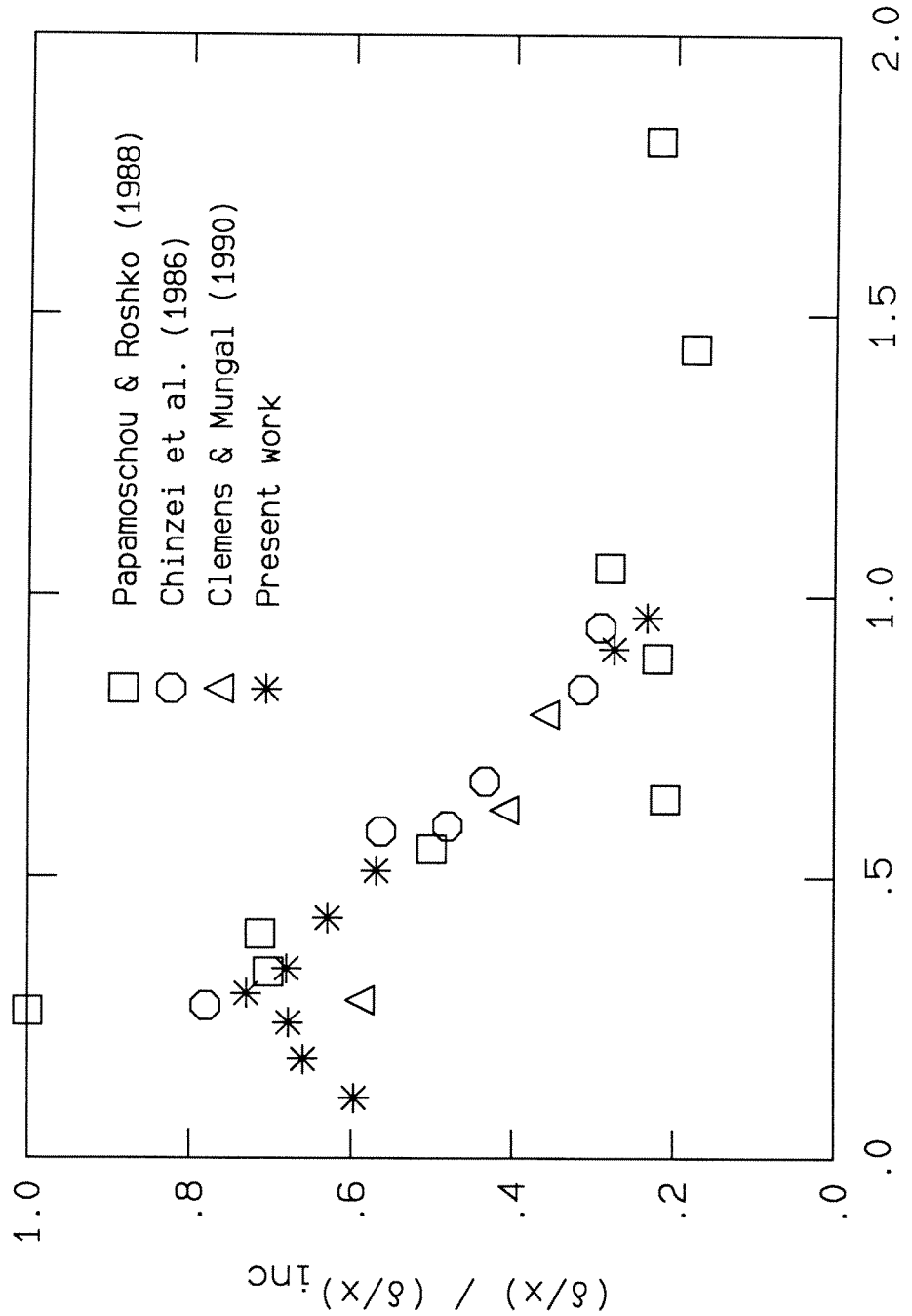

Fig. 4.23: Normalized Growth Rate Of Supersonic Flow Cases 1-9 Plotted With Other Available Data.

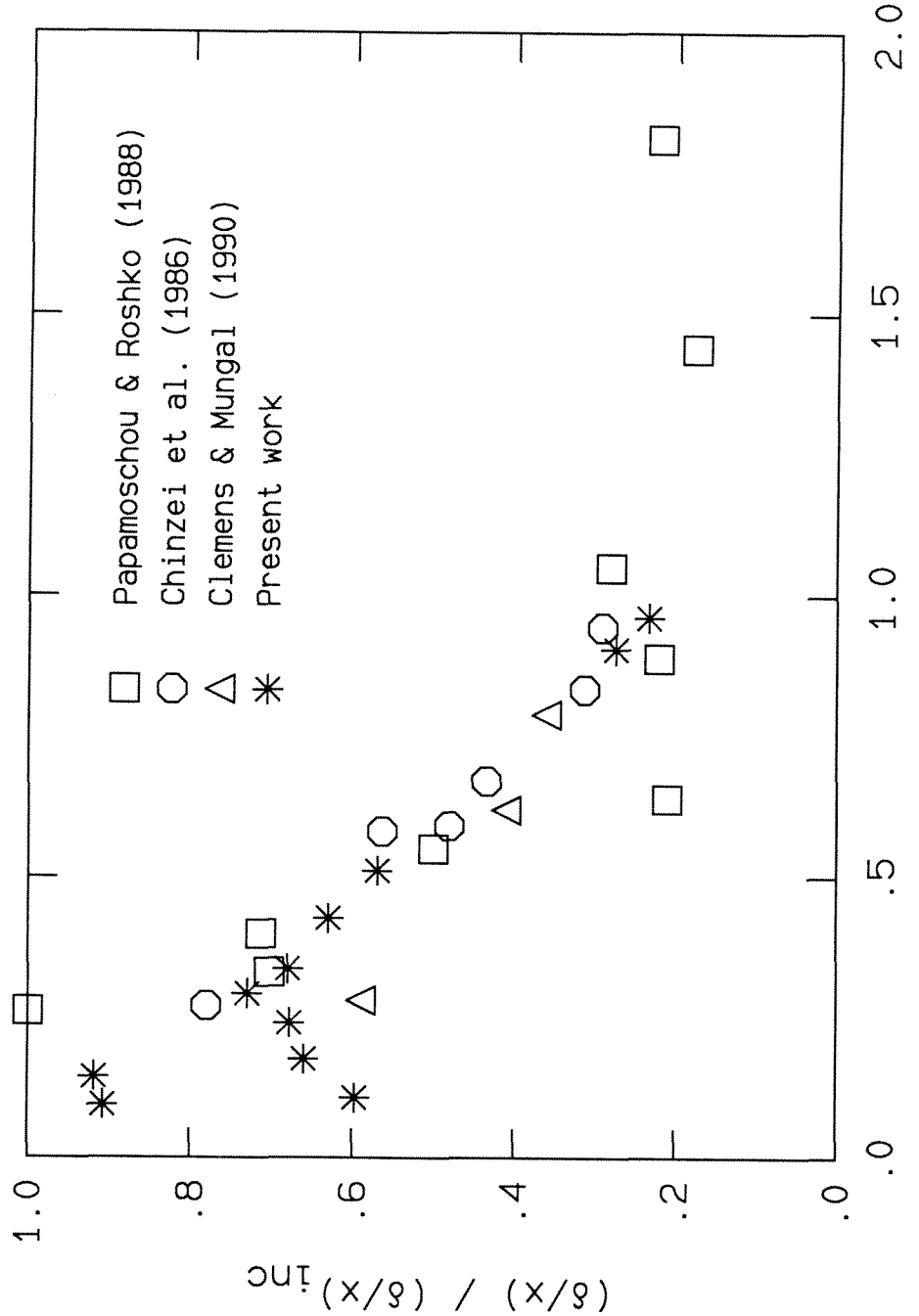

Fig. 4.24: Normalized Growth Rate of All Cases (1-11) Plotted With Other Available Data.

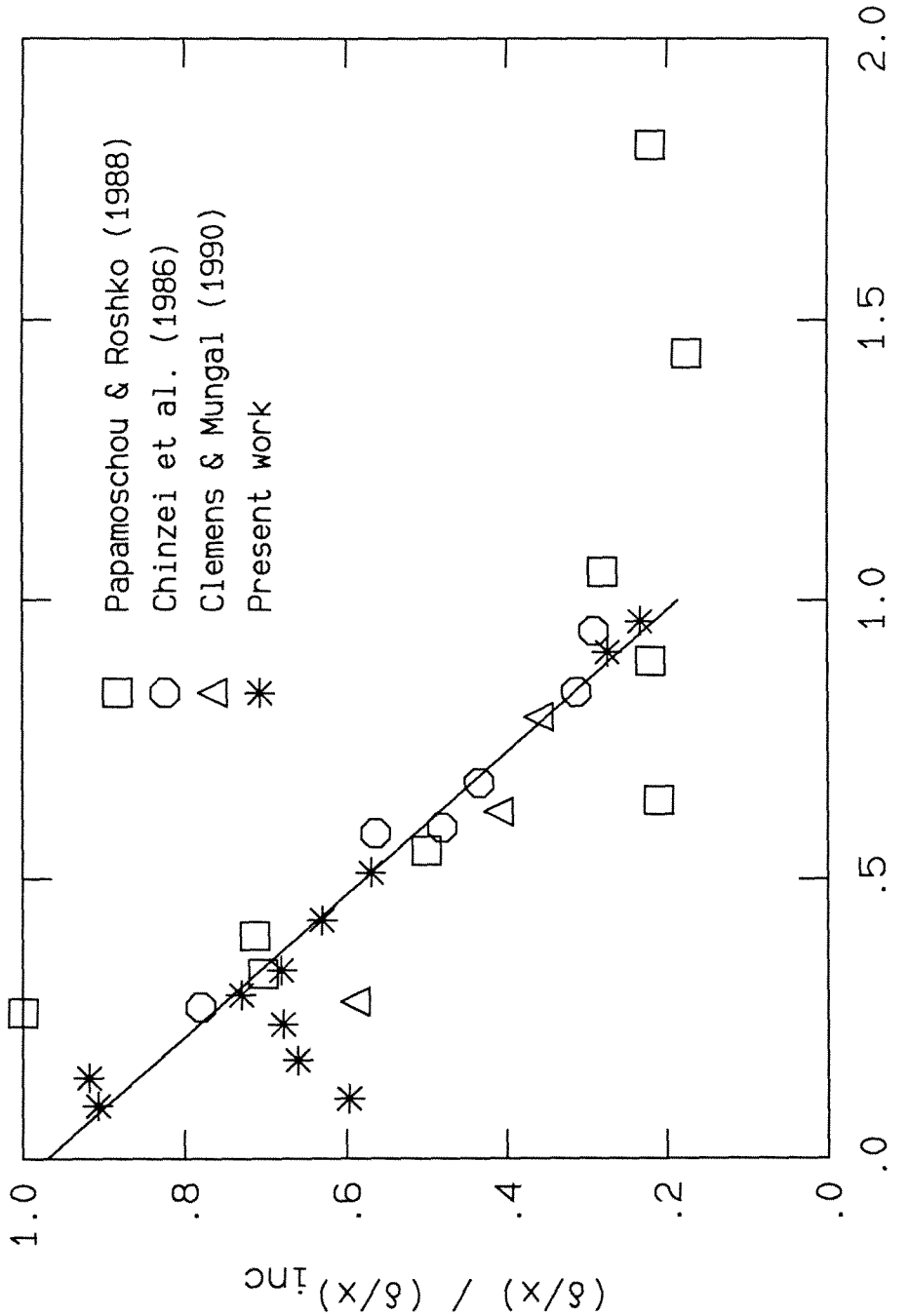

Fig. 4.25: Normalized Growth Rate Of Available Data With Fitted Straight Line Below $M_{c1}=1$.

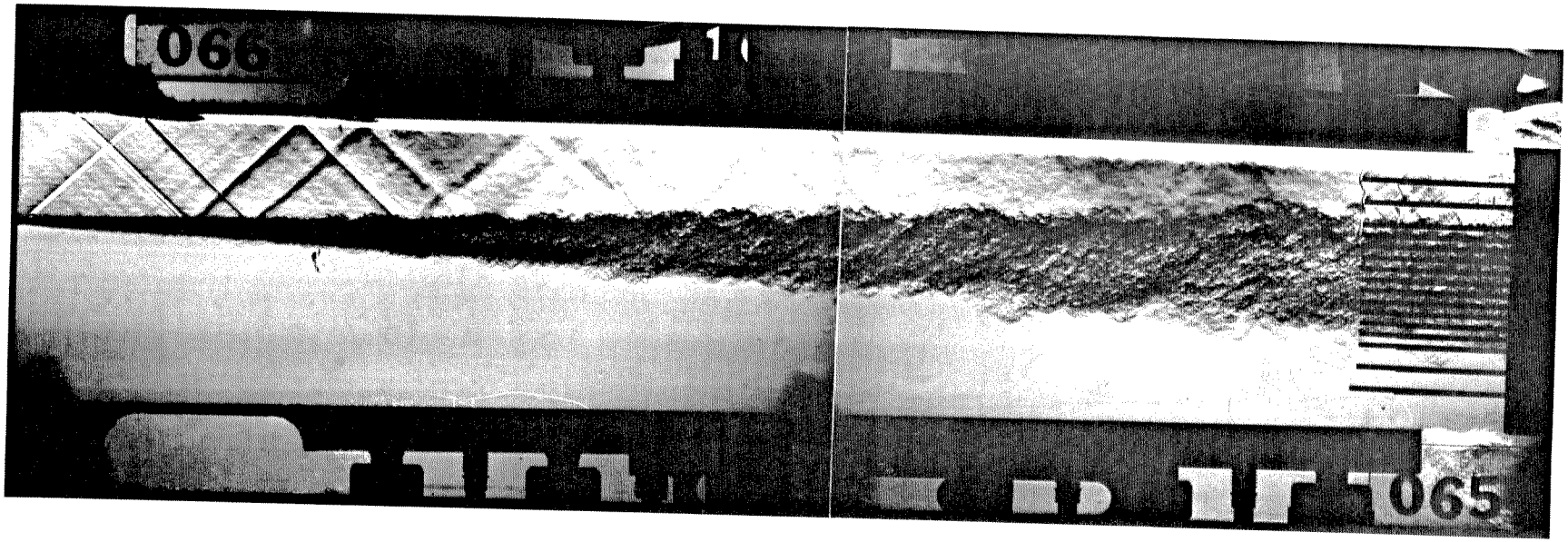

Fig. 4.26: Composite Schlieren Photograph of Case 6 (N_2/75%He+25%Ar) Flow.

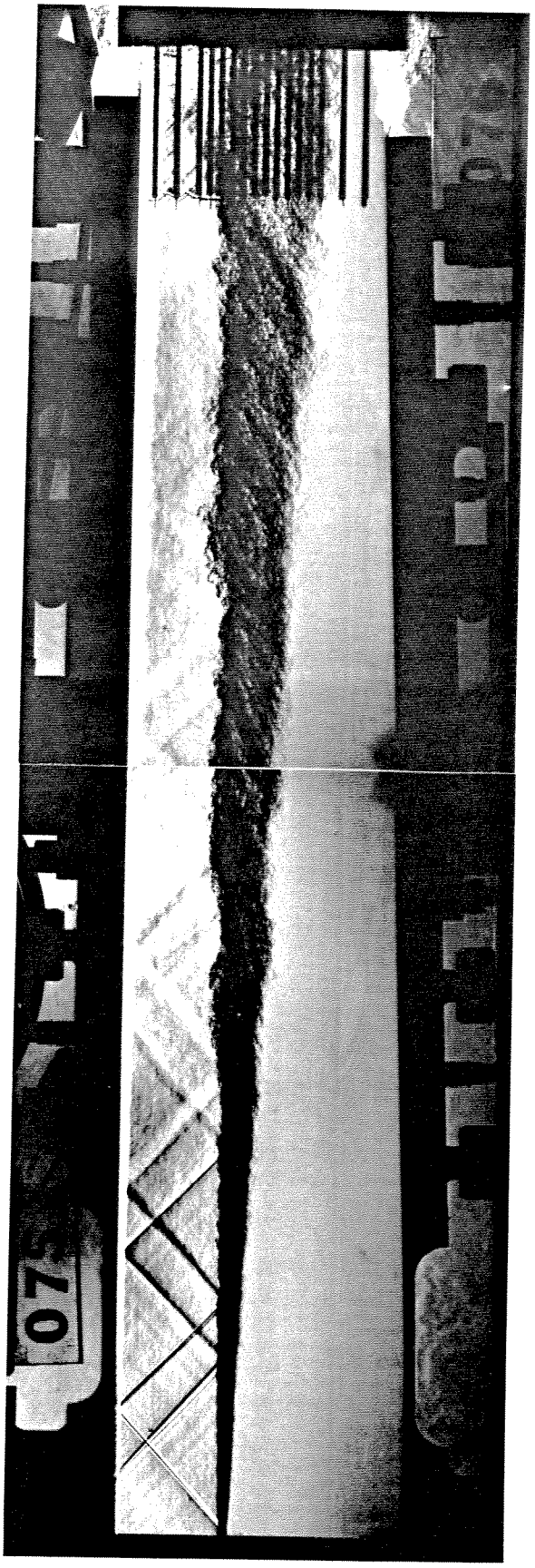

Fig. 4.27: Composite Schlieren Photograph Of Case 7 (N_2/90%He+10%Ar) Flow.

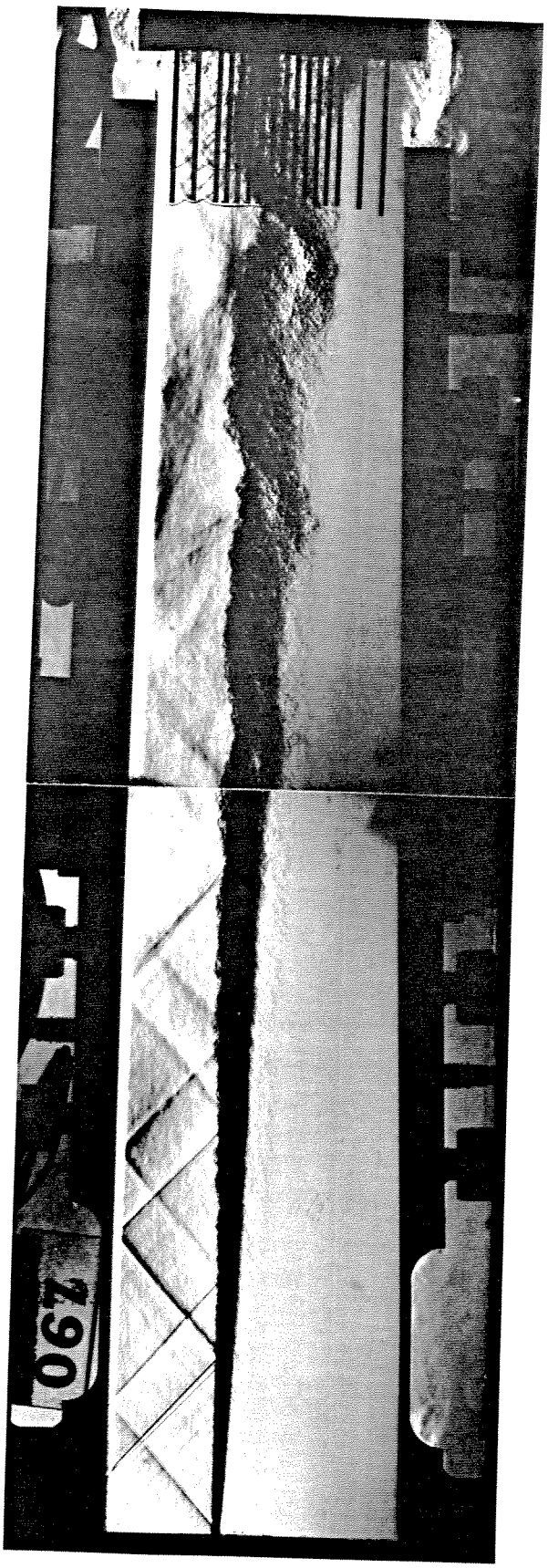

Fig. 4.28: Composite Schlieren Photograph Of Case 8 (N_2/He) Flow.

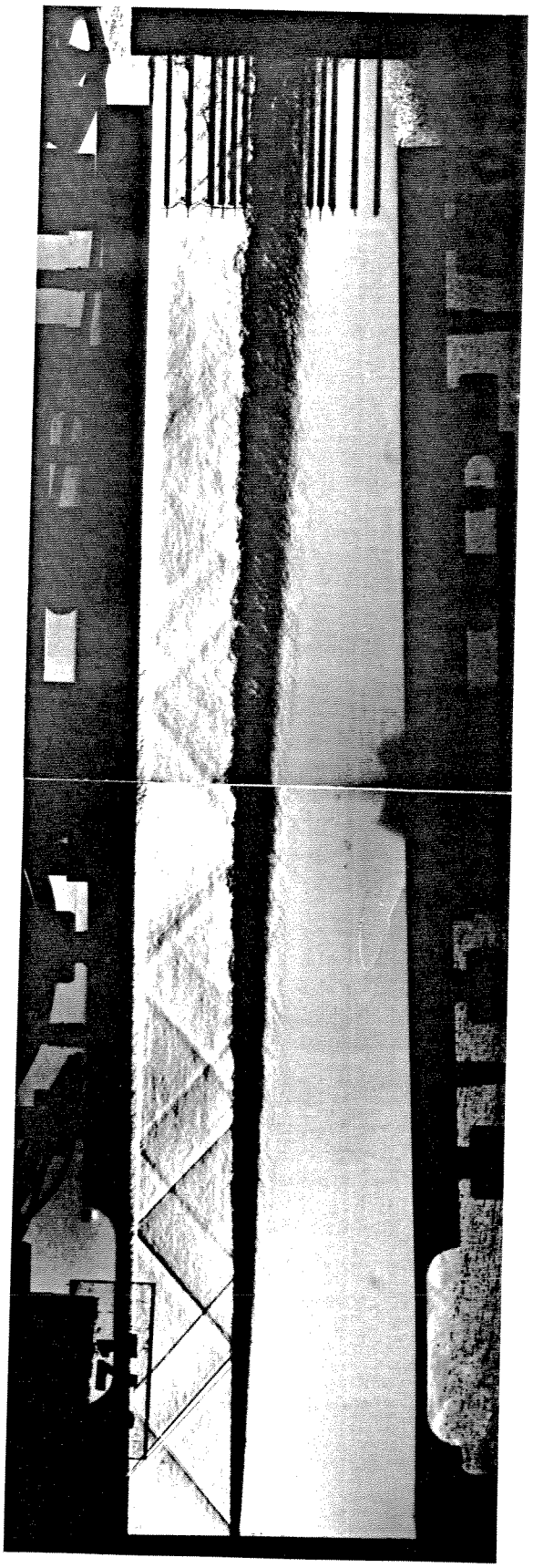

Fig. 4.29: Composite Schlieren Photograph Of Case 9 (Ar/He) Flow.

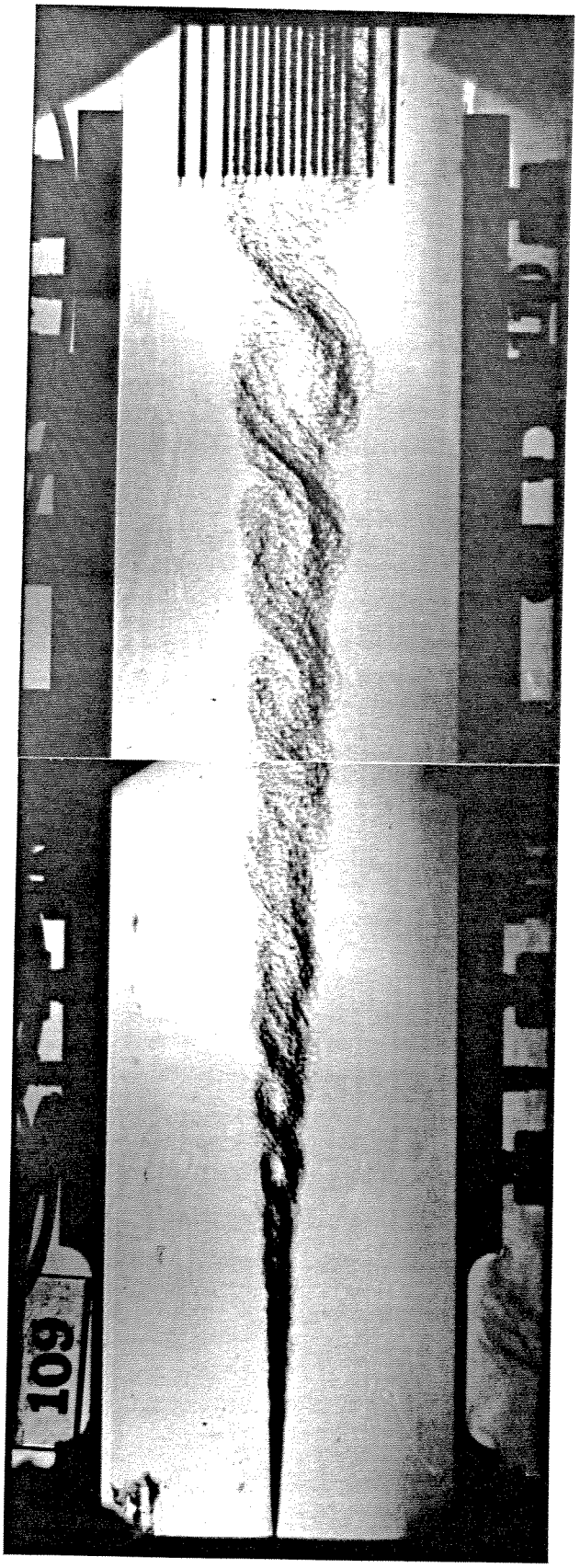

Fig. 4.30: Composite Schlieren Photograph Of Case 10 (subsonic N_2/33%He+66%Ar) Flow.

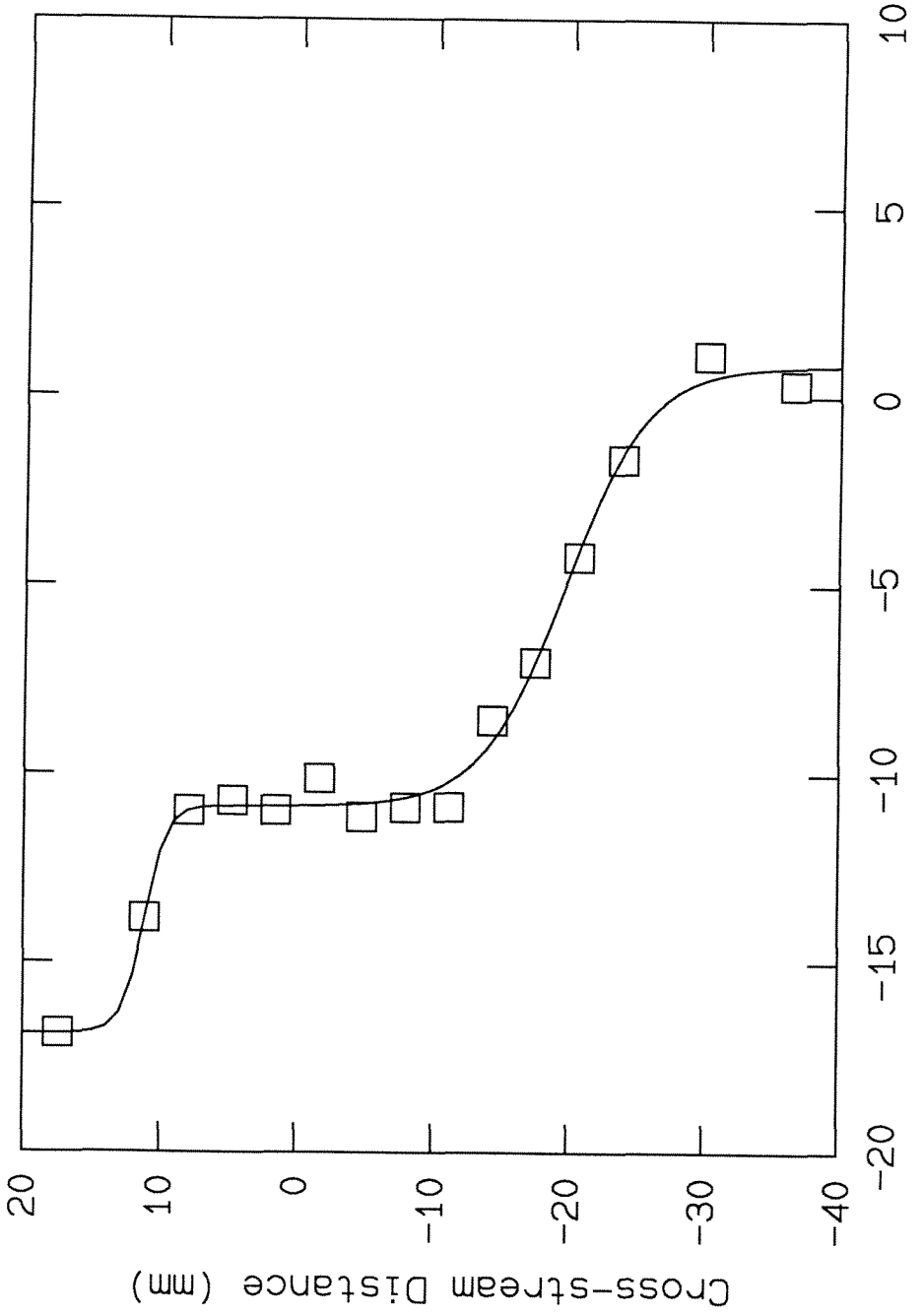

Fig. 5.1: Measured Non-Reacting Temperature Profile For Case 3 (N_2/N_2) Flow.

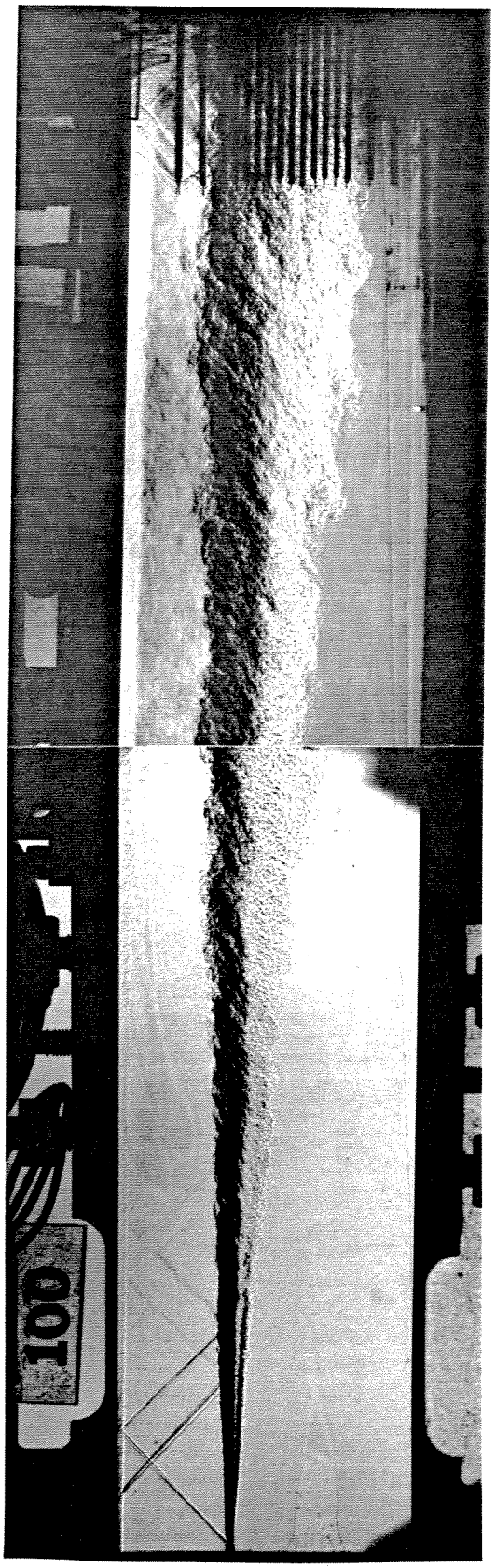

Fig. 5.2 Composite Schlieren Photograph Of Case 3c (N_2/N_2 diluents) Reacting Flow.

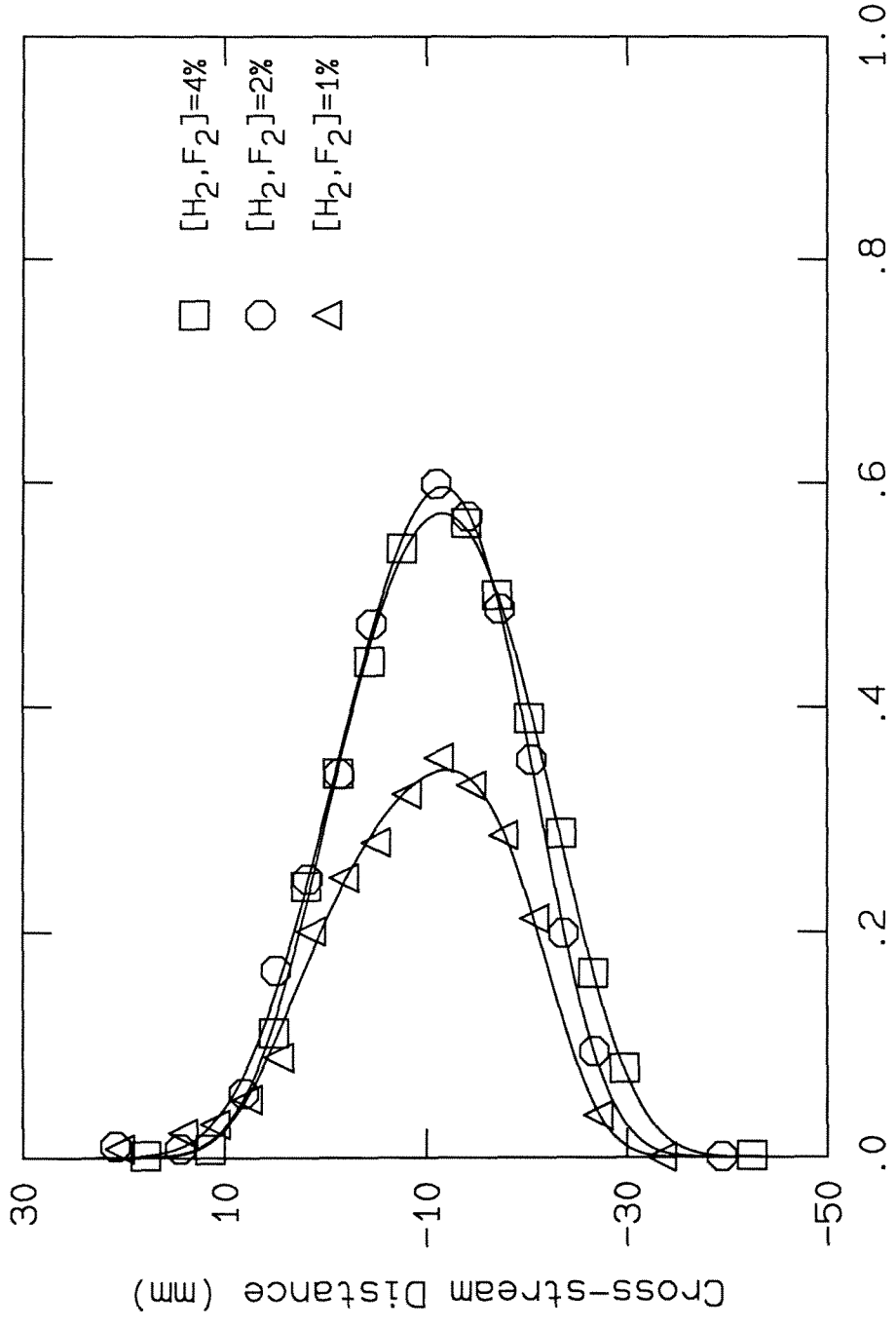

Fig. 5.3: Normalized Temperature Profiles For The Case 3 Kinetics Experiment.

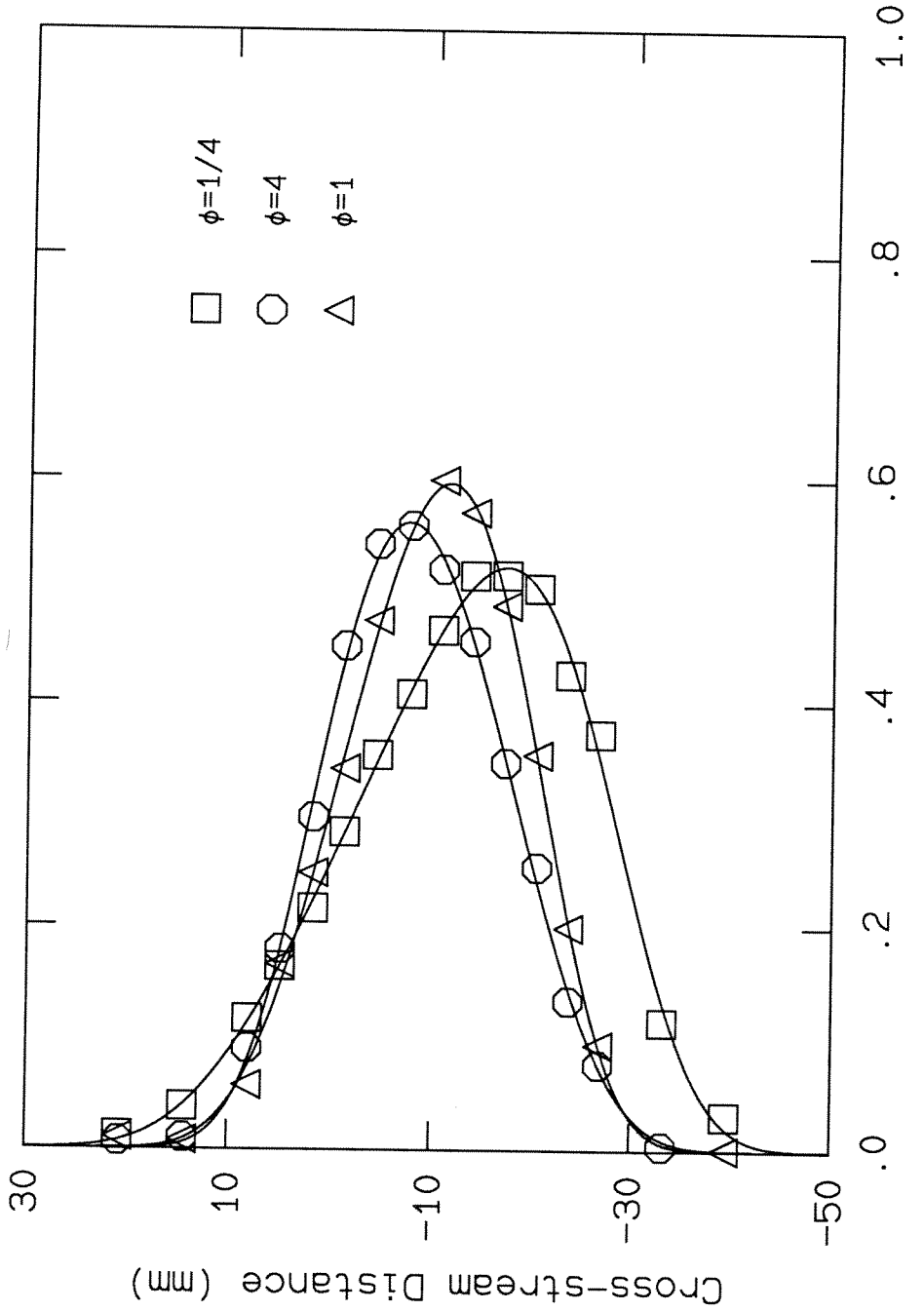

Fig. 5.4: Normalized Temperature Profiles For The Case 3 Flip Experiment.

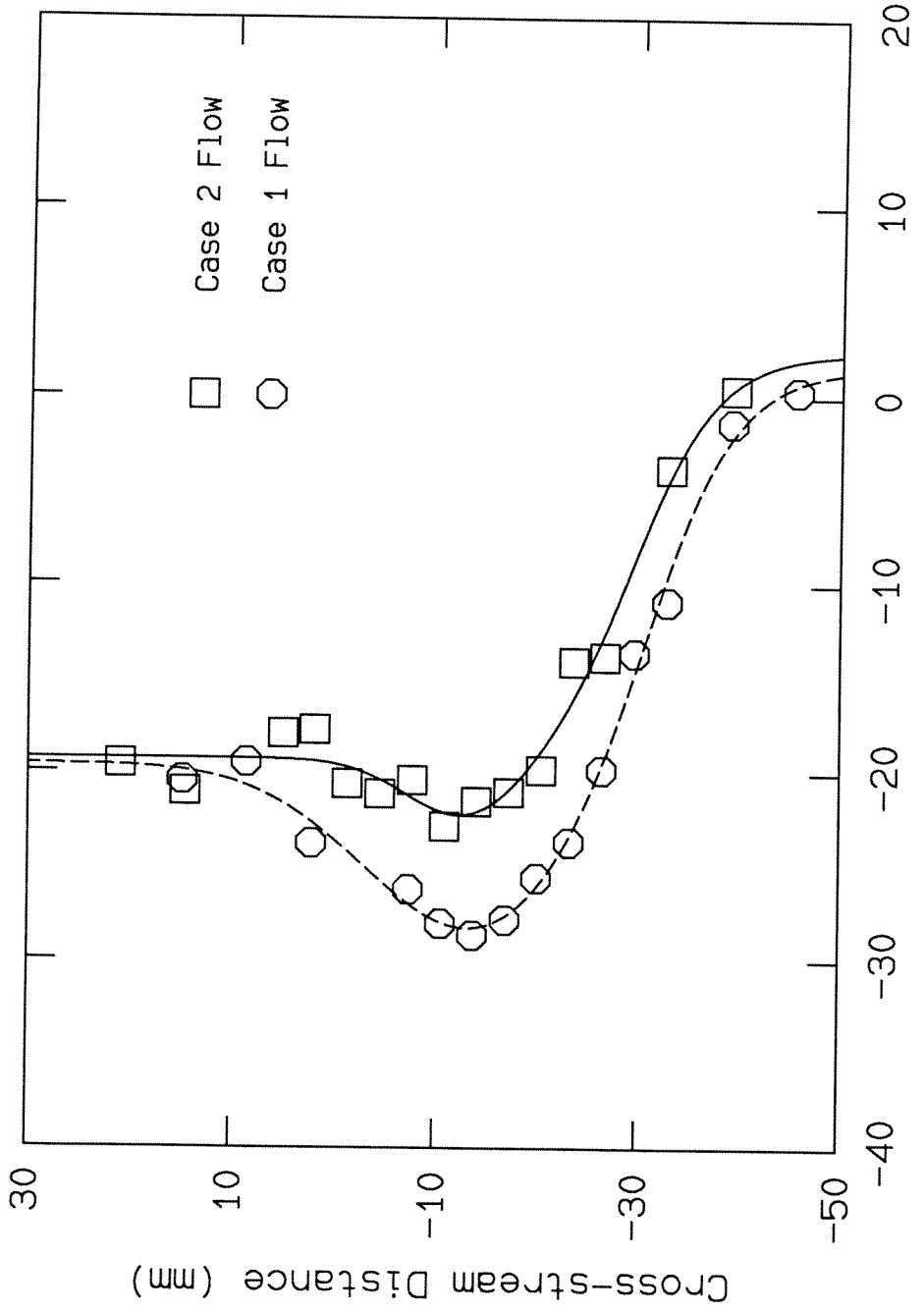

Fig. 5.5: Measured Non-Reacting Temperature Profile For Case 1 and Case 2 Flows.

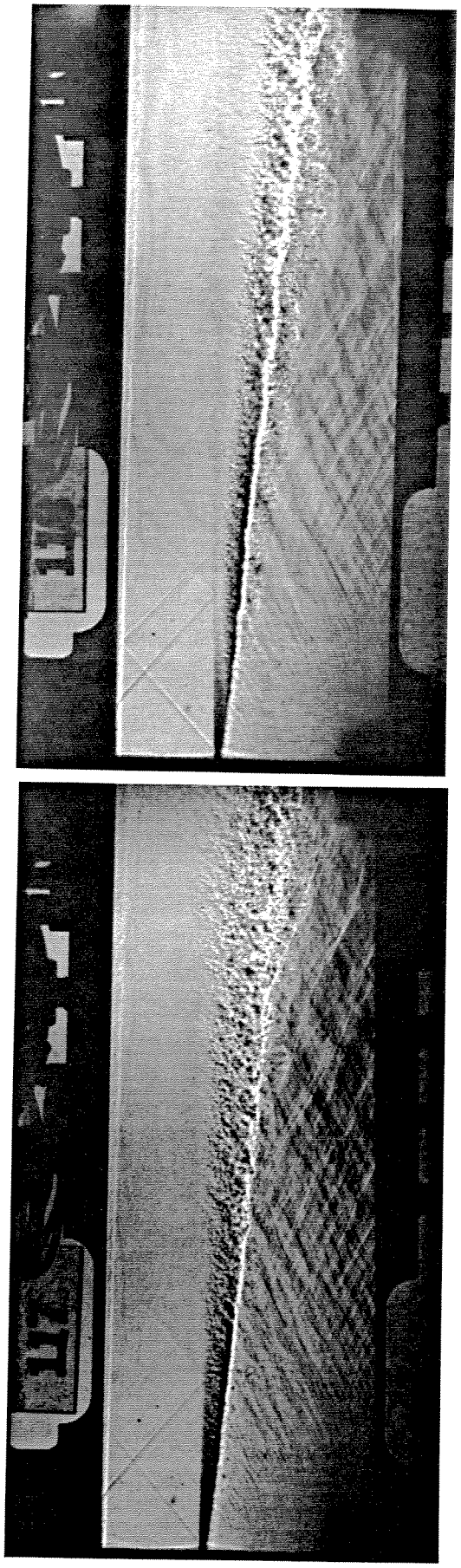

(a) Non-Reacting (b) Reacting

Fig. 5.6: Shadowgraph Comparison Of Reacting and Non-Reacting Case 2 Flows (He/N_2 Diluents).

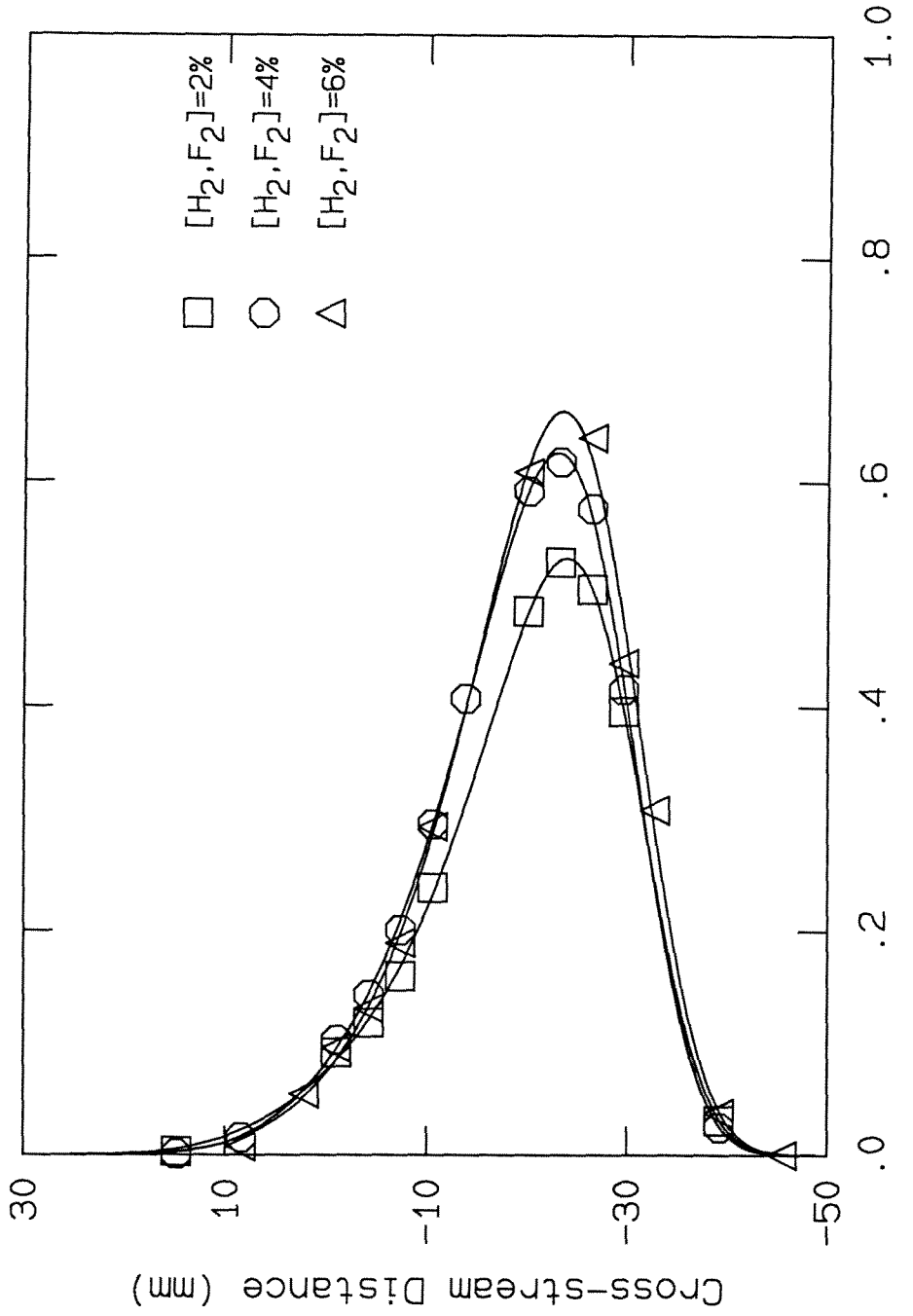

Fig. 5.7: Normalized Temperature Profiles For The Case 2 Kinetics Experiment.

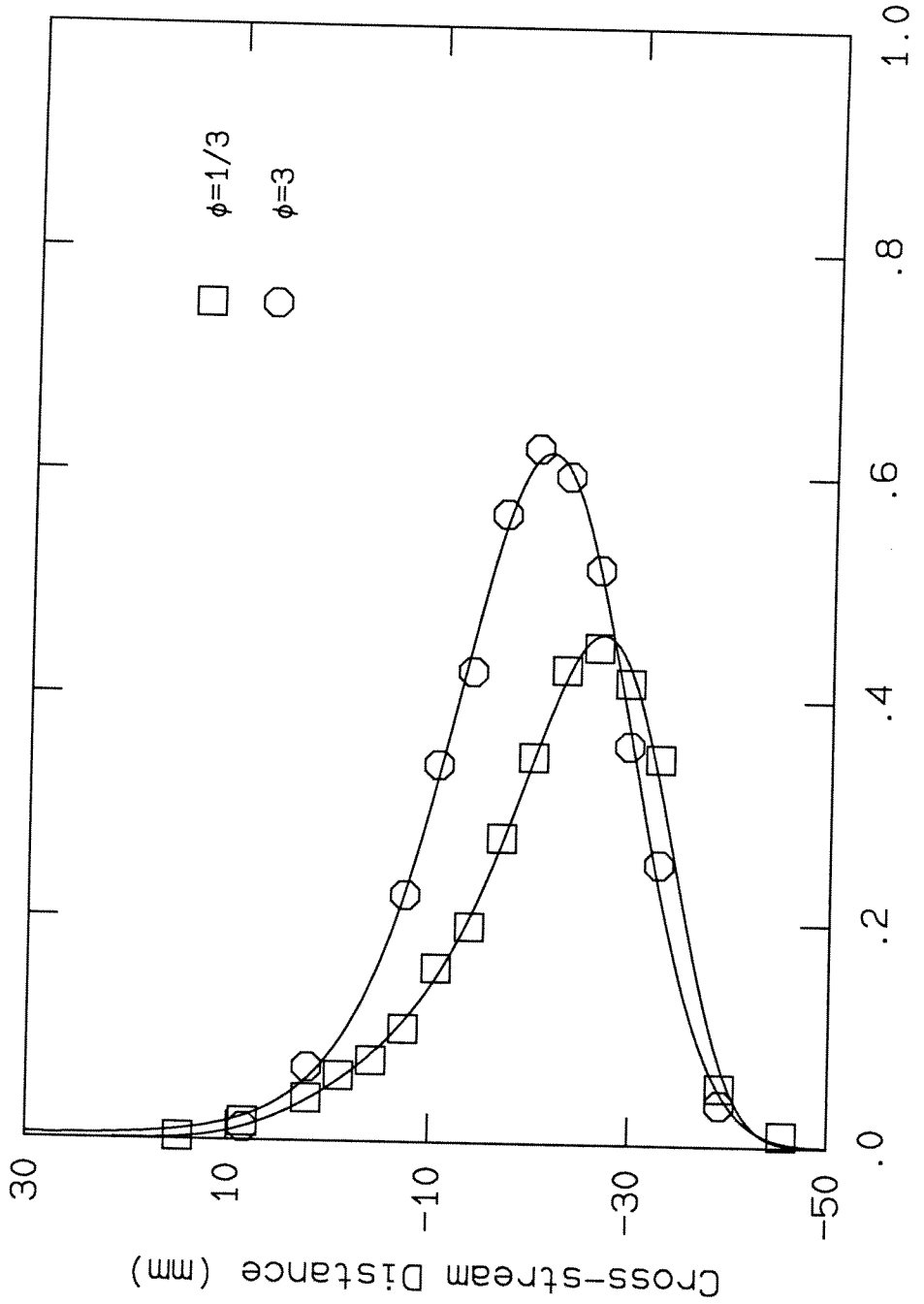

Fig. 5.8: Normalized Temperature Profiles For The Case 1 Flip Experiment.

Appendix A

Further Details On The Design Of The Supersonic Hydrogen-Fluorine Facility

This appendix has been included to provide the reader with additional information concerning the design of the new facility. It consists of several engineering drawings and schematics, as well as some brief descriptions.

Fig. A.1 is a comprehensive flow schematic for the entire facility. It shows the gas flow on both sides, as well as the waste gas treatment system. Although not every detail can be discussed here, the following list contains the key points not covered in Chapter 3:

1. Safety burst diaphrams have been installed on the H_2/NO Reactant Tank and the F_2 Mixing Vessel. Pressure relief valves have been installed on the Surge Tank, the N_2 Receiver, the LN_2 Dewar and the 6000 psi inert manifolds.
2. Filters are used on all inert gas manifolds to remove particulates, oil and water vapour.
3. The NaOH shower system operates in a closed-loop fashion, that is, with the pumped liquid draining back into the reservoirs to be used again. There are two pumps in parallel for redundancy. A particulate filter is installed on the pump feed line (not shown).
4. The vented gas on the F_2 side is passed through a bed of activated charcoal and then bubbled through a barrel full of high pH $NaOH$ in water (not shown). This neutralizes the unused F_2 gas. The exhaust from the F_2 Mixing Vessel burst diaphram also vents in this fashion.

Approximately 165 electrical strip heaters are bolted onto the H_2/NO Reactant Tank (Figure A.2) in order to preheat the high speed gas. These Mica strip heaters are divided into five zones on the tank, each of which can be controlled separately. A total of twenty thermocouples bolted onto the tank provide the required temperature feedback. The heaters, the thermocouples and the microprocessor-based control system were all manufactured by the WATLOW company. Thermal insulation of

the tank is provided by a four and a half inch thick ceramic fibre insulating material which completely surrounds the tank. This insulation, in turn, is protected by a shell of sheet aluminum. It is this aluminum exterior that is seen in the facility photographs, Figs. 3.1 and 3.2.

The specifications for the Compumotor KH-740 servomotor are listed in Table A.1. This is the motor used to drive the main pressure regulator on the high speed side.

Figure A.3 shows the test section plenum chamber and flow management devices. The arrangement is standard: A perforated cone is used to diffuse the incoming flow, followed by a pair of coarse mesh screens to break down the large turbulent structures, honeycomb to remove the swirl and finally a pair of fine mesh screens to complete the cascade to small-scale turbulence. Note that all of the screens are quite porous, with open areas exceeding 60% . This criterion was taken from Loehrke & Nagib (1972). Finally, note that all of the screens and the honeycomb in the drawing are mounted inside aluminum frames, a modular arrangement that facilitates their removal for adjustment and repair purposes.

Figure A.4 is an engineering drawing of the test section guidewalls. Note particularly the locations of the PCB and Druck pressure transducers.

Figure A.5 is a drawing of a thermocouple probe. Recall that sixteen such probes are clamped into the instrument rake to provide mean total temperature profile measurements across the flow. The thermocouple wire and junctions were manufactured by the OMEGA company. Final assembly of the probes was performed by Earl Dahl.

A cutaway drawing of the shower tunnel is presented as Figure A.6. It consists of a thirty-inch diameter 304 stainless steel pipe with numerous outside connections and internal components. The exhaust gas from the test section enters from the left, flows down the pipe and is turned upwards into the catch bag by a pair of turning vanes. Along the axis of this pipe are twenty showerheads that spray the gas on the fly with the neutralizing solution of sodium hydroxide in water. The showerheads are a mixture of Spraying Systems Inc. model 7N and 7G devices, which produce mean drop sizes in the range of 150 to 300 μm. The main shower pump that provides this sodium hydroxide flow is a CAT Pump model 6020 positive displacement pump, which is typically set for 350 psi output pressure.

Figure A.7 is a drawing of the catch bag that collects the exhaust gas from an experiment. This bag has approximately 4000 cubic feet of internal volume when fully inflated. It is constructed from a three-ply laminated material 0.030 inch thick, consisting of a layer of polyester sandwiched between layers of a poly-vinyl and polyurethane alloy (Keptex APR3018B). This bag was constructed by Kepner Plastics Fabricators Inc. This material is extremely corrosion resistant and mechanically tough, and it has a chemical additive to make it resistant to ultraviolet radiation from the sun. Across the top of this bag are fourteen more showerheads of the types already described for the shower tunnel. These catch bag showers are fed by a flex hose that runs from the shower tunnel feedthrough to the top of the catch bag. These showers typically operate for a total of three minutes after an experiment in order to fully neutralize the exhaust gas.

Table A.1: KH-740 Servomotor Specifications

Manufacturer	Compumotor
Static Torque (continuous)	29 Nm
Static Torque (peak)	58 Nm
Rated Power	3400 watts
Motor Weight	26.4 kg
Top Speed	1300 rpm
Rotor Inertia	$3.85 \times 10^{-3} Kgm^2$
Acceleration at Peak Torque	15061 rad/sec/sec
Resolution	32768 steps/rev
Repeatability	$\pm 0.088°$
Accuracy	$\pm 0.23°$
Operating Temperature	0° C to 50° C
Motor Input Power	240 VAC, 3 phase, 30 amps max.
Control Input Power	120 VAC, 1 Phase, 1 Amp max.
Control Inputs	step, direction, shutdown and limits
Control Outputs	drive fault, in position, prog. outputs
Control Interface	RS-232, 9600 Baud, 8 data bits, no parity

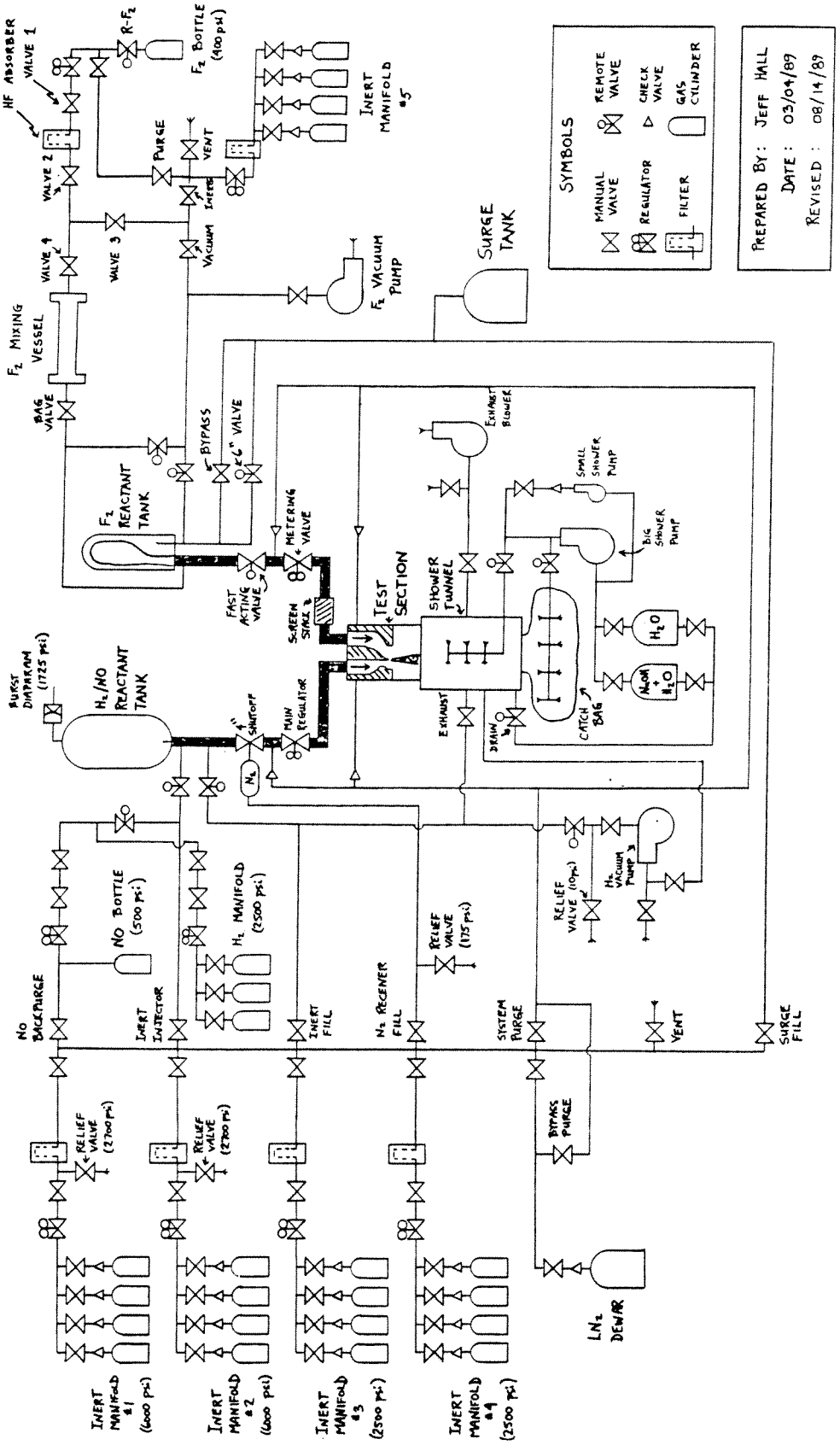

Fig. A.1: Comprehensive Flow Schematic Of The Supersonic Hydrogen-Fluorine Facility.

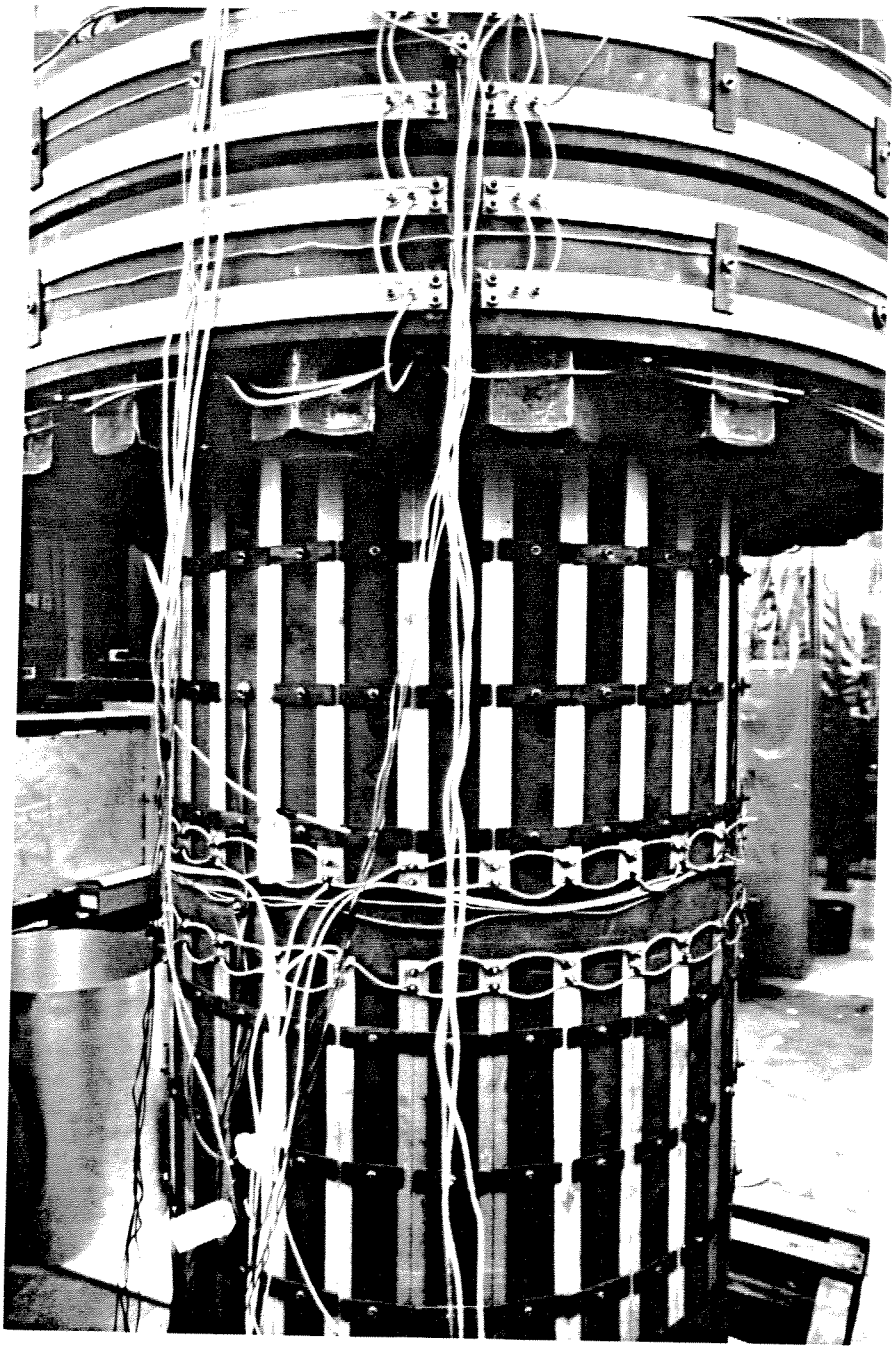

Fig. A.2: Photograph Showing Strip Heaters On H_2/NO Reactant Tank.

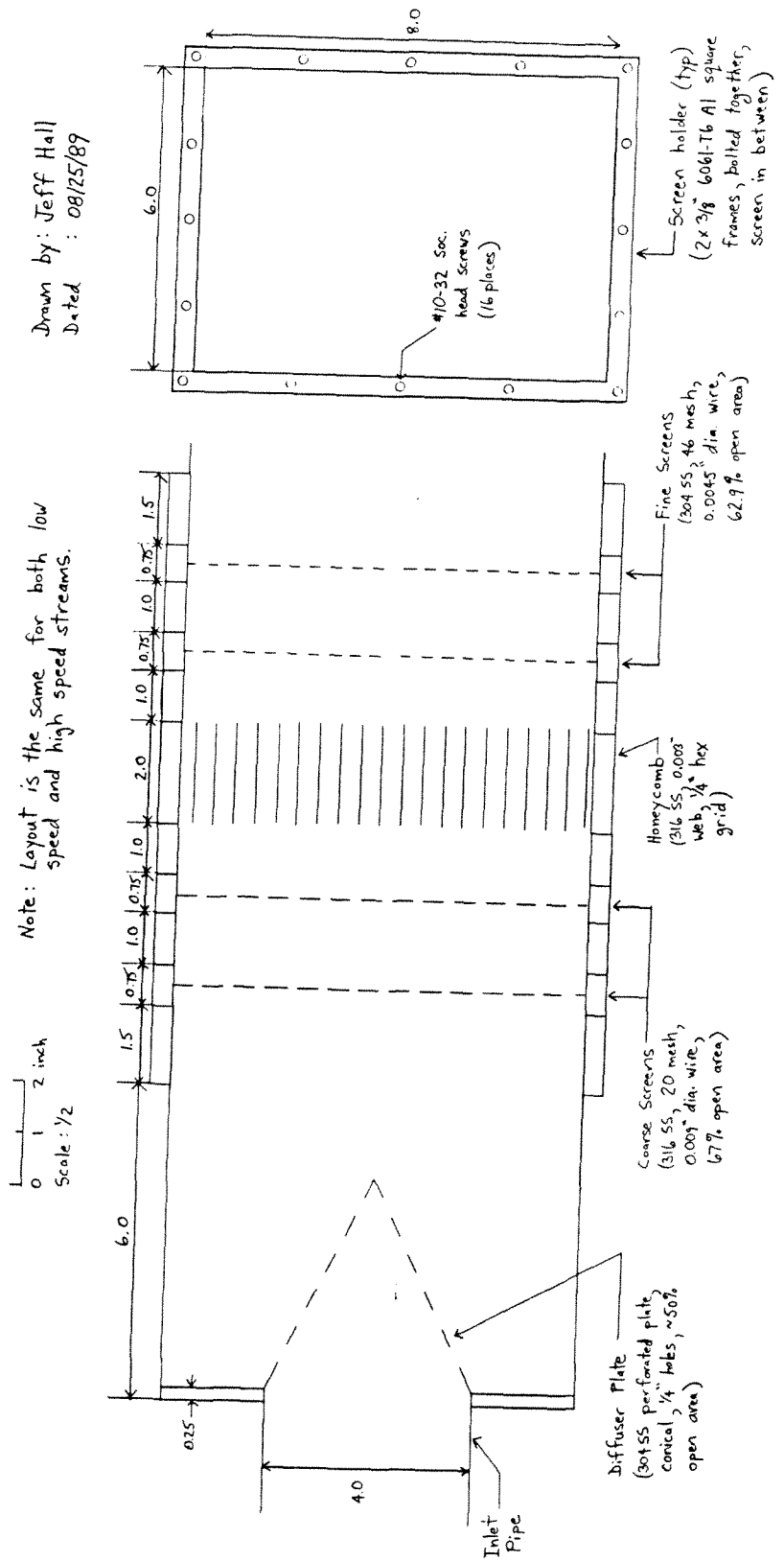

Fig. A.3: Test Section Plenum Chamber And Flow Management System.

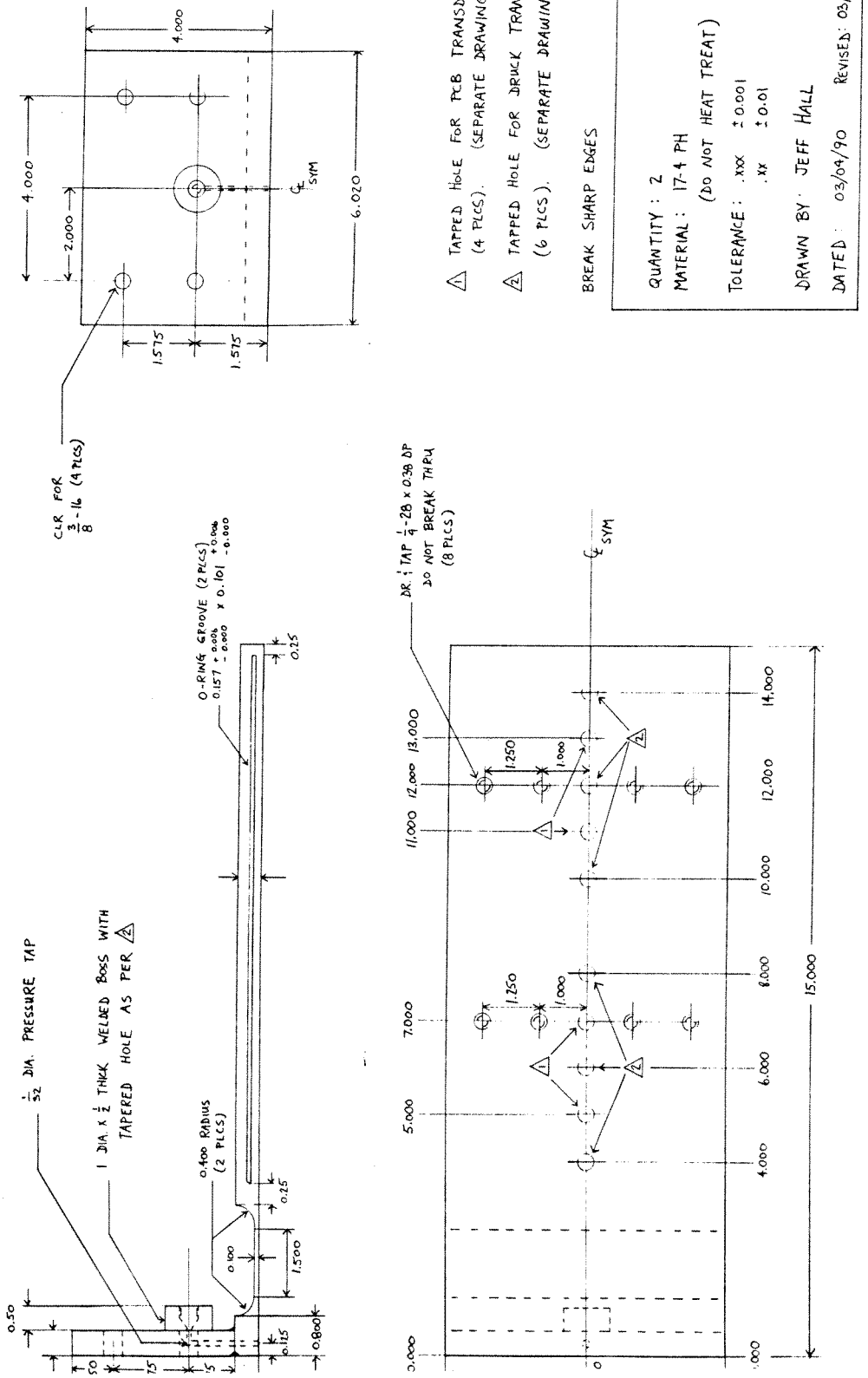

Fig. A.4: Test Section Guidewall.

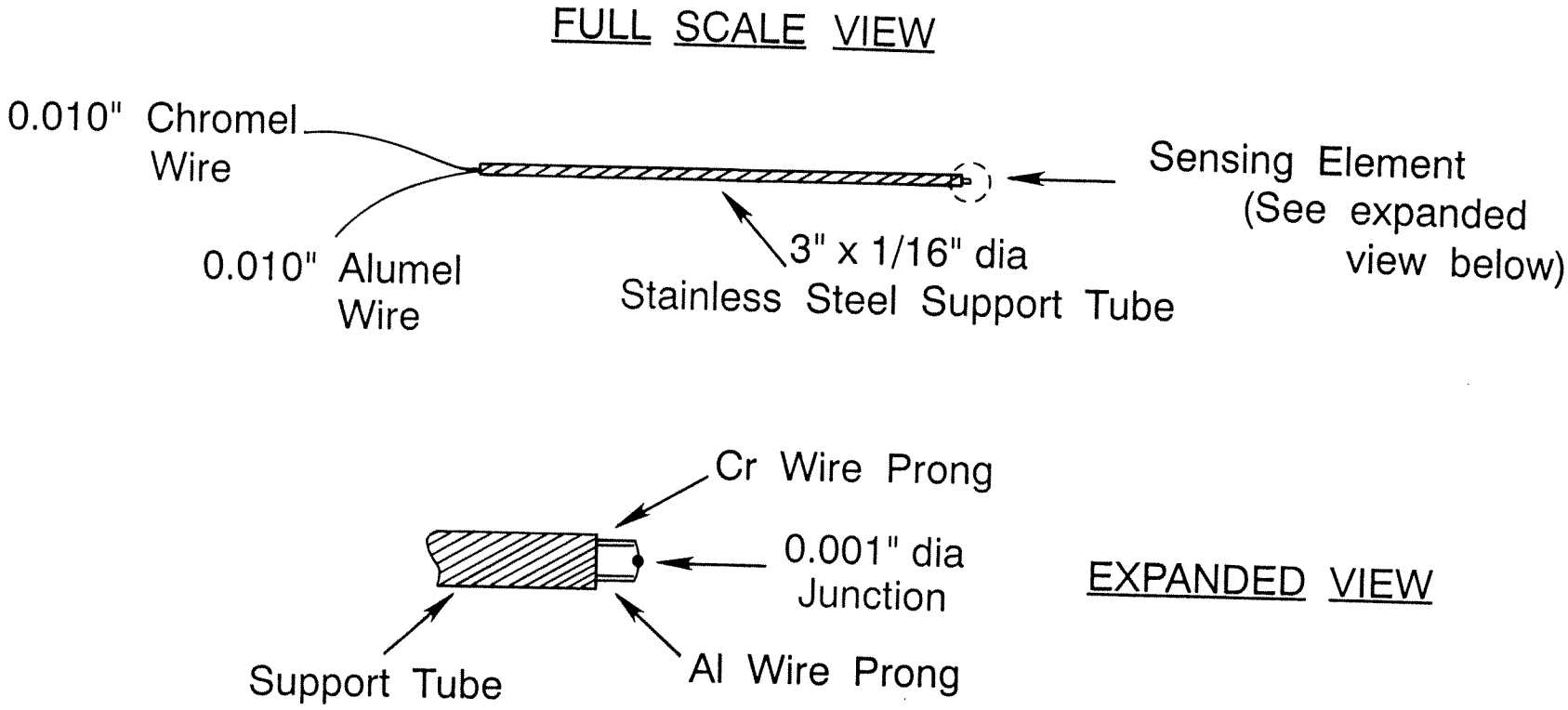

Fig. A.5: Sketch Of Thermocouple Probe.

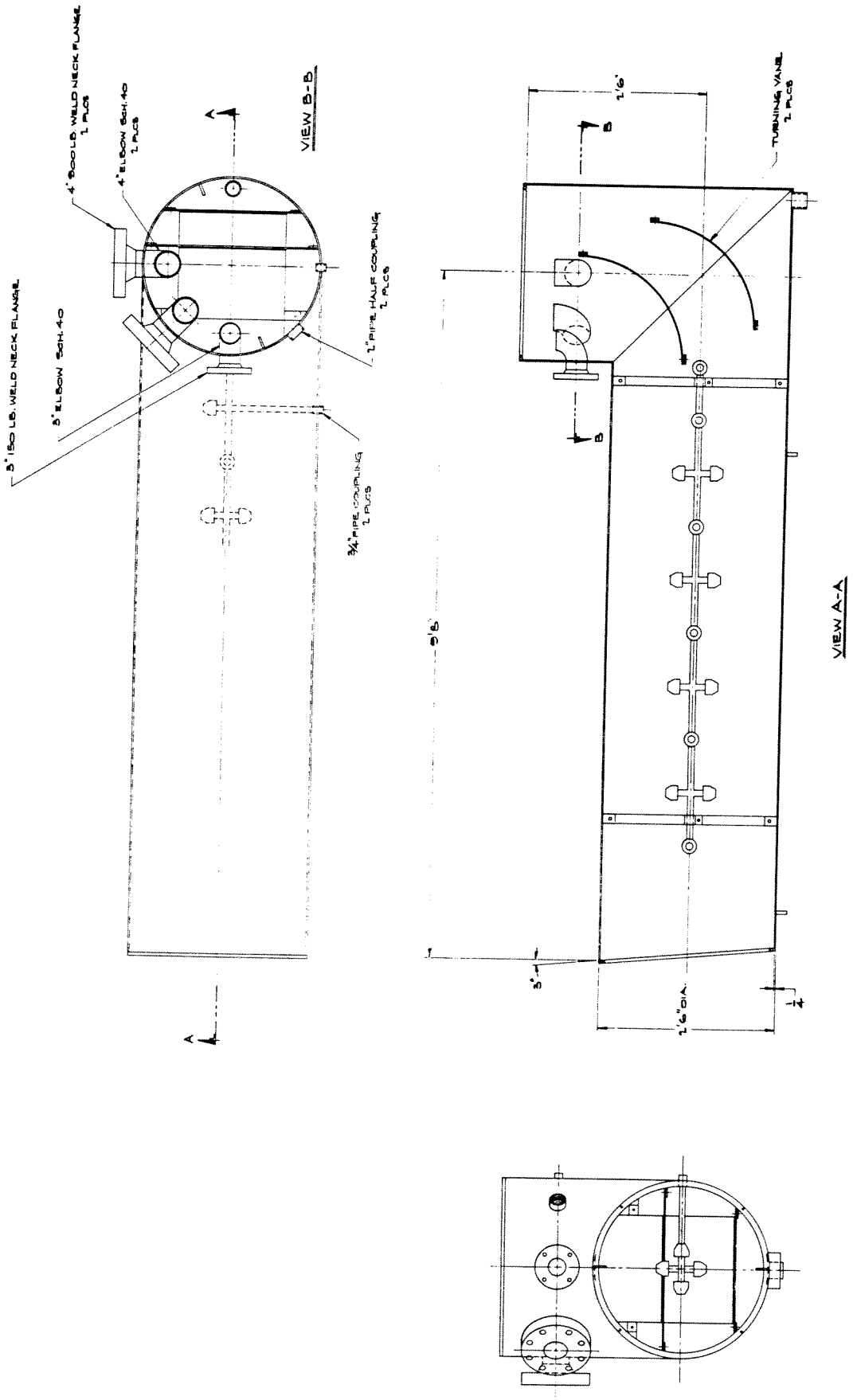

Fig. A.6: Cut-away Drawing Of The Shower Tunnel.

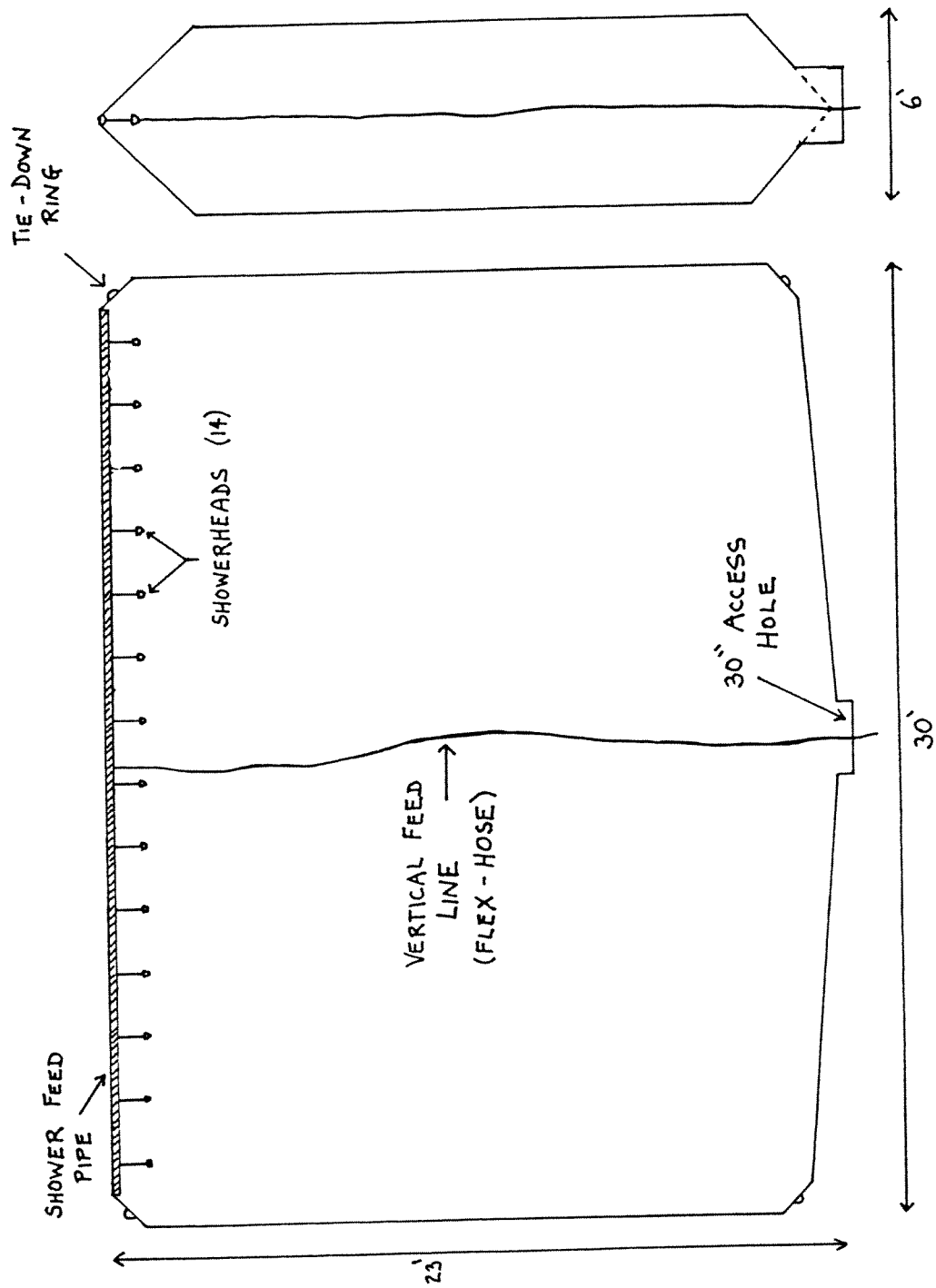

Fig. A.7: Sketch Of The Catch Bag.